

# Stochastic characterization of discrete fractures in rocks by hydraulic tomography

Dissertation

zur Erlangung des  
Doktorgrades der Naturwissenschaften (Dr. rer. nat)

der  
Naturwissenschaftlichen Fakultät III  
Agrar- und Ernährungswissenschaften,  
Geowissenschaften und Informatik  
der Martin-Luther-Universität Halle-Wittenberg

vorgelegt von  
Frau Ringel, Lisa Maria  
Geb. am 10.04.1995 in Ingolstadt

Gutachter:  
Prof. Dr. rer. nat. Peter Bayer  
Prof. Dr. rer. nat. Florian Amann

Tag der Verteidigung: 09. Mai 2023



# Abstract

Fracture networks are the main pathways for groundwater flow and transport especially in rocks with a low-permeability matrix. For this reason, the presence, connectivity, and hydraulic properties of fracture networks concern groundwater resources, geothermal systems, and the environmental safety of waste repositories. Hydraulic tomography experiments provide one approach for characterizing fractured sites. For this method, several intervals of adjacent boreholes are isolated by packer systems at different depths. A given pumping rate in one of the intervals induces a perturbation of the steady-state pressure, and the resulting transient pressure curves are recorded in the surrounding intervals. This procedure is repeated for all intervals; thus, multiple combinations of pressure signals are measured, which serve as the basis for the inversion of the hydraulic and structural properties of fractured rocks.

For this purpose, a discrete fracture network (DFN) model is applied. A DFN model implies planar fractures and a permeability determined by the fracture aperture. The derivation of a DFN realization from the pressure response curves is a challenging topic due to the high number of unknown parameters and the significant contrast between highly permeable fractures and a nearly impervious rock matrix. Therefore, a new approach for the evaluation of hydraulic tomography experiments that is specifically suited for fractured sites is developed and tested in this thesis. In comparison to previous studies that mainly utilize continuous inversion methods, the properties of the fractured rock are addressed more directly by the DFN model. Thereby, a DFN model is implemented to perform the forward simulations, the structural and hydraulic properties of a DFN are inferred, and the results are evaluated as the fracture probability. The inversion is accomplished by a stochastic method based on the Bayesian equation that defines a posterior distribution of the DFN parameters given the measured data. The posterior distribution is characterized by sampling from it according to Markov chain Monte Carlo (MCMC) methods. An initial DFN configuration is updated iteratively by adding or deleting fractures or by changing the position, length, and hydraulic aperture of a fracture. This results in several posterior DFN realizations of approximately equal probability. The structural properties of the DFN realizations are processed to a fracture probability map over the investigated region and a mean hydraulic aperture indicating transmissivity and storativity of the fractures.

The developed inversion approach is tested and evaluated with two- (2D) and three-dimensional (3D) synthetic test cases. The synthetic test cases demonstrate the applicability of the method in general and the sensitivity of the inversion results to a different tomographic setup. Moreover, the method is applied to the inversion

---

of hydraulic tomography experiments conducted as part of the In situ Stimulation and Circulation experiments at the Grimsel Test Site in Switzerland. Flow, seismic, and ground penetrating radar tests identified a highly fractured and most permeable area of 4 m to 6 m width between two shear zones which is the target of the inversion. The fracture probability map of the investigated zone highlights two preferential flow paths with different levels of permeability.

This work delineates a practical procedure for the setup of a DFN inversion problem as derived from the work with synthetic test cases and the field application. This includes a list of studies that have to be conducted before the DFN inversion, a description of common assumptions and simplifications for the derivation of constraints and prior distributions, and a recommendation for the specification of site-dependent parameters. Thereby, this project facilitates the direct inversion of hydraulic and structural parameters of DFNs and promotes the application to other fractured sites and on a larger scale.

# Zusammenfassung

Kluftnetzwerke sind bedeutende Wegsamkeiten für Grundwasserströmung und Transport. Das gilt insbesondere für Gesteine, die eine Gesteinsmatrix mit geringer Permeabilität aufweisen. Aus diesem Grund sind das Auftreten, die Konnektivität und die hydraulischen Eigenschaften von Kluftnetzwerken für Grundwasserressourcen, geothermische Systeme und die Umweltverträglichkeit von Deponien von Bedeutung. Einen Ansatz zur Charakterisierung von geklüfteten Standorten bietet die hydraulische Tomographie. Für dieses Verfahren werden mehrere Intervalle benachbarter Bohrlöcher durch Packersysteme in unterschiedlichen Tiefen isoliert. Durch eine vorgegebene Pumprate in einem der Intervalle wird eine Störung des stationären Drucks hervorgerufen und die daraus resultierenden instationären Druckkurven werden in den umliegenden Intervallen aufgezeichnet. Dieses Vorgehen wird für alle Intervalle wiederholt, sodass mehrere Kombinationen von Drucksignalen gemessen werden können. Diese dienen als Grundlage für die Inversion der hydraulischen und strukturellen Eigenschaften des geklüfteten Gesteins.

Für die Inversion wird in dieser Arbeit ein diskretes Kluftnetzwerkmodell angewendet. Ein diskretes Kluftnetzwerkmodell setzt ebene Klüfte und eine durch die Kluftöffnung bestimmte Permeabilität voraus. Die Berechnung eines Kluftnetzwerks aus den Druckkurven stellt aufgrund der großen Anzahl unbekannter Parameter und des starken Kontrasts zwischen durchlässigen Klüften und einer nahezu undurchlässigen Gesteinsmatrix eine Herausforderung dar. Deswegen wird hier ein neuer Ansatz zur Auswertung von hydraulischer Tomographie entwickelt und erprobt, der sich speziell für geklüftete Standorte eignet. Im Vergleich zu früheren Studien, die hauptsächlich kontinuierliche Inversionsverfahren anwenden, werden die Eigenschaften des geklüfteten Gesteins durch das diskrete Kluftnetzwerkmodell unmittelbarer berücksichtigt. Dazu wird ein diskretes Kluftnetzwerkmodell für die Durchführung der Simulationen implementiert, die strukturellen und hydraulischen Eigenschaften des diskreten Kluftnetzwerkmodells werden bestimmt und die Ergebnisse als Kluftwahrscheinlichkeit ausgewertet. Die Inversion erfolgt durch ein stochastisches Verfahren, das auf der Bayes'schen Gleichung basiert, die eine Posterior-Verteilung der Parameter des Kluftnetzwerks in Abhängigkeit von den gemessenen Daten definiert. Die Posterior-Verteilung wird durch mehrere Stichproben, die mit dem Markov-Ketten-Monte-Carlo-Verfahren erzeugt werden, charakterisiert. Eine erste Konfiguration eines Kluftnetzwerks wird iterativ durch Hinzufügen oder Löschen von Klüften oder durch das Anpassen von deren Position, Länge und Kluftöffnung variiert. Dies führt zu mehreren Realisierungen von diskreten Kluftnetzwerken mit ungefähr gleicher Wahrscheinlichkeit. Die strukturellen Eigenschaften der Kluftnetzwerke werden für den untersuchten Bereich

---

durch die Visualisierung der Kluftwahrscheinlichkeiten und der mittleren Kluftöffnung, die Transmissivität und Speicherfähigkeit der Klüfte bestimmt, ausgewertet.

Der erarbeitete Inversionsansatz wird durch zwei- (2D) und dreidimensionale (3D) synthetische Beispiele getestet und bewertet. Die synthetischen Testfälle demonstrieren die grundsätzliche Anwendbarkeit der Methode und die Sensitivität der Inversionsergebnisse gegenüber unterschiedlichen tomographischen Einstellungen. Darüber hinaus wird die Methode auf die Inversion von hydraulischen Tomographieexperimenten angewendet, die als Teil der In-situ-Stimulations- und Zirkulationsexperimente am Grimsel-Testgelände in der Schweiz durchgeführt wurden. Strömungsmessungen, Seismik und Bodenradaruntersuchungen ergaben einen hochgradig geklüfteten und höchst durchlässigen Bereich von 4 m bis 6 m Breite zwischen zwei Scherzonen. Die Charakterisierung dieses Bereichs ist das Ziel der Inversion. Die Auswertung der Kluftwahrscheinlichkeiten in dem untersuchten Bereich zeigt zwei bevorzugte Fließwege mit unterschiedlichen Permeabilitäten.

In dieser Arbeit wird ein praktisches Verfahren für den Ablauf eines Inversionsproblems zur Charakterisierung von geklüfteten Standorten vorgestellt, das sich aus der Arbeit mit synthetischen Testfällen und der Feldanwendung ergibt. Dies beinhaltet eine Empfehlung von Untersuchungen, die vor der Inversion durchgeführt werden müssen, eine Beschreibung gängiger Annahmen und Vereinfachungen für die Ableitung von Randbedingungen und Prior-Verteilungen, sowie eine Empfehlung für die Spezifikation von standortabhängigen Parametern. Dadurch ermöglicht diese Studie die direkte Inversion der hydraulischen und strukturellen Parameter von diskreten Kluftnetzwerken und fördert die Anwendung auf andere geklüftete Standorte und in einem größeren Maßstab.

# Publications

The following three publications are part of this thesis (cumulative thesis):

Chapter 2 has been published as Ringel, L. M., Somogyvári, M., Jalali, M., & Bayer, P. (2019). Comparison of Hydraulic and Tracer Tomography for Discrete Fracture Network Inversion. *Geosciences*, 9(6), 274. <https://doi.org/10.3390/geosciences9060274>.

Chapter 3 has been published as Ringel, L. M., Jalali, M., & Bayer, P. (2021). Stochastic Inversion of Three-Dimensional Discrete Fracture Network Structure With Hydraulic Tomography. *Water Resources Research*, 57(12), e2021WR030401. <https://doi.org/10.1029/2021WR030401>.

Chapter 4 has been published as Ringel, L. M., Jalali, M., Bayer, P. (2022). Characterization of the highly fractured zone at the Grimsel Test Site based on hydraulic tomography. *Hydrology and Earth System Sciences*, 26(24), 6443–6455. <https://doi.org/10.5194/hess-26-6443-2022>.

Summary of author contributions:

Ringel, et al. (2019), Chapter 2: Formal analysis, L.M.R., M.S., M.J. and P.B.; Investigation, L.M.R., M.S., M.J. and P.B.; Methodology, L.M.R., M.S., M.J. and P.B.; Writing–original draft, L.M.R., M.S. and P.B.; Writing–review & editing, M.J. and P.B.

Ringel, et al. (2021), Chapter 3: Conceptualization: L.M.R., M.J., P.B; Funding acquisition: P.B.; Methodology: L.M.R; Project Administration: P.B.; Supervision: P.B.; Visualization: L.M.R, M.J., P.B.; Writing – original draft: L.M.R; Writing – review & editing: M.J, P.B

Ringel, et al. (2022), Chapter 4: Funding acquisition: P.B.; Measurements: M.J.; Methodology: L.M.R., P.B.; Inversion: L.M.R; Writing – original draft: L.M.R.; Writing – review & editing: M.J., P.B





# Acknowledgments

This work would not have been possible without my supervisor Peter Bayer, and the support from Márk Somogyvári and Mohammadreza Jalali. I am extremely grateful to Peter Bayer for offering me the opportunity to take on and conclude this PhD project, for his valuable support, constructive feedback, and encouragement. This project would have been much more difficult without Márk Somogyvári and his help getting me started by sharing his work with me. I very much appreciate the discussions with Mohammadreza Jalali who introduced me to the field work conducted during the In situ Stimulation and Circulation experiments at the Grimsel Test Site. The exchange with him was essential for the setup of the inversion and the forward simulations.

I would like to highlight that I am fortunate to be a part of the working group *Applied Geology* of MLU Halle-Wittenberg. I could always count on my colleagues for answering my questions about geological processes I was not familiar with and for providing a motivating and supporting environment.

Preparing the publications and the thesis required not only academic support, but also encouragement from my family and friends. I thank my life partner Raphael Miehling for his unconditional love and patience. I owe special thanks to my parents, Gabi and Christian Ringel, for their support throughout my whole life. Many thanks to my sisters, Vera and Anna Ringel for keeping me motivated and confident during the entire process of this thesis. This work would not have been possible without them.



# Contents

<b>1</b>	<b>Introduction</b>	<b>1</b>
1.1	Fracture networks . . . . .	1
1.2	Tomography experiments for fractured sites . . . . .	4
1.3	Inverse problems . . . . .	10
1.4	Objective and outline of this study . . . . .	13
<b>2</b>	<b>Comparison of hydraulic and tracer tomography for DFN inversion</b>	<b>15</b>
2.1	Introduction . . . . .	15
2.2	Methodology . . . . .	17
2.2.1	DFN case study . . . . .	17
2.2.2	Transdimensional inversion . . . . .	19
2.2.3	Estimation of the noise variance . . . . .	23
2.3	Results . . . . .	25
2.3.1	Results of the DFN inversion . . . . .	26
2.3.2	Results estimating the noise variance . . . . .	28
2.4	Discussion and conclusions . . . . .	29
<b>3</b>	<b>Stochastic inversion of 3D DFN structure with hydraulic tomography</b>	<b>33</b>
3.1	Introduction . . . . .	33
3.2	Methodology . . . . .	35
3.2.1	Forward modeling of hydraulic tomography experiment . . . . .	36
3.2.2	Inversion methodology . . . . .	37
3.2.3	Setup of test cases . . . . .	40
3.2.4	Implementation of the inversion . . . . .	43
3.2.5	Evaluation of the results . . . . .	45
3.3	Results . . . . .	46
3.3.1	Test case 1 . . . . .	46
3.3.2	Test case 2 . . . . .	47
3.3.3	Test case 3 . . . . .	49
3.3.4	Test case 4 . . . . .	50
3.3.5	Comparison of the results for all four test cases . . . . .	51
3.4	Conclusions and outlook . . . . .	51
<b>4</b>	<b>Characterization of the highly fractured zone at the Grimsel Test Site</b>	<b>53</b>
4.1	Introduction . . . . .	53
4.2	Experimental setting . . . . .	56
4.2.1	Test site . . . . .	56

4.2.2	Hydraulic tomography data . . . . .	57
4.3	Implementation of the inversion . . . . .	58
4.3.1	Forward modeling . . . . .	58
4.3.2	Inversion algorithm . . . . .	60
4.3.3	Inversion constraints . . . . .	61
4.3.4	Prior distributions . . . . .	63
4.4	Results . . . . .	64
4.4.1	Processing of the results . . . . .	64
4.4.2	Evaluation of the data . . . . .	65
4.4.3	Evaluation of the DFN realizations . . . . .	66
4.4.4	Comparison with other studies . . . . .	68
4.5	Conclusions . . . . .	68
<b>5</b>	<b>Synopsis</b>	<b>71</b>
5.1	Summary and conclusions . . . . .	71
5.2	Outlook . . . . .	73
	<b>Appendix</b>	<b>77</b>
A.1	Supporting information for Chapter 3 . . . . .	77
	<b>References</b>	<b>81</b>
	<b>Curriculum vitae</b>	<b>99</b>
	<b>Declaration</b>	<b>101</b>

# List of Figures

1.1	Illustration of evaluation methods of tomography experiments from different artificial examples, (a) continuous tomogram, (b) simplification of the fracture structure according to predefined orientations or connectivity, (c) simplification of the fractured rock based on a DFN model. . . . .	5
1.2	Classification of the field studies (Table 1.1) concerning the characterization of fractured sites according to the scale of the investigated region and the resolution of the fracture properties by the inversion results. . . . .	11
2.1	Synthetic DFN with three injection points and three receiver points based on an outcrop in Switzerland. . . . .	18
2.2	Flowchart showing the inversion algorithm with its main phases. . .	20
2.3	Scheme to explain the procedure of drawing samples from a variance probability function (pdf) . . . . .	26
2.4	(a) Synthetic discrete fracture networks (DFN) and (b) the results using the pressure signals for the inversion illustrated as fracture probability map. . . . .	27
2.5	(a) Synthetic DFN and (b) the results using the tracer BTCs for the inversion illustrated as fracture probability map. . . . .	28
2.6	Noisy tracer BTCs ( $\sigma_{\text{noise}} = 3$ ) for different combinations of source and receiver points. . . . .	29
2.7	Histogram of variance samples during the inversion and posterior pdf of $\sigma_{\text{noise}}^2 p\left(\sigma_{\text{noise}}^2   \mathbf{d}, \theta_{-\sigma_{\text{noise}}^2}\right)$ in the last iteration of the rjMCMC loop (a) inversion of $\sigma_{\text{noise}}^2$ using the inverse gamma prior; and, (b) inversion of $\sigma_{\text{noise}}^2$ using the uniform prior. . . . .	30
2.8	Noisy pressure signals ( $\sigma_{\text{noise}} = 3000$ ) for different combinations of source and receiver points. . . . .	30
2.9	Histogram of variance samples and posterior pdf of $\sigma_{\text{noise}}^2$ in the last step of the inversion. . . . .	31
3.1	Overview of the implemented rjMCMC sampling strategy for the discrete fracture network (DFN) inversion with the between-model moves (insertion or deletion of fractures) and the within-model move, that is, the update of the DFN parameters. . . . .	39

3.2	(a) Synthetic test case 1 (base case), boreholes, and source/receiver points denoted as S/R 1 to S/R 5. (b) Pressure signals recorded at the different receiver points (R 1 to 5) provoked by an overpressure created at the source points (S 1 to 5). . . . .	41
3.3	(a) Test case 3 oriented at the base case with an extra injection point fracture and an additional source/receiver point (S/R 6). (c) Test case 4 including a third fracture set and an additional source/receiver point (S/R 6). The noisy pressure signals and the mean of the simulated pressure curves of the posterior DFN realizations are displayed for both test cases in (b) and (d). . . . .	42
3.4	(a) Rasterized test case 1. (b) Inversion results illustrated as FPM presented for constant positions $y$ . . . . .	46
3.5	Inversion results of test case 2 evaluated as (a) fracture probability map and (b) mean aperture of each element. . . . .	48
3.6	(a) Rasterized test case 3. (b) Inversion results illustrated as FPM for different cross sections for constant values $y$ . . . . .	49
3.7	(a) Rasterized test case 4. (b) Inversion results illustrated as FPM presented for different cross sections for constant values $y$ . . . . .	50
4.1	(a) General overview of the ISC experimental site showing the AU (Auflockerungszone, i.e., excavation effects) tunnel, the VE (ventilation test) tunnel, all boreholes, and the two types of shear zones (Krietsch et al., 2018). (b) The volume that is investigated in this study, i.e., the zone between the two brittle–ductile (S3) faults. . . .	56
4.2	Pressure response in the different intervals provoked by a constant rate injection applied sequentially to the intervals Inj1–Int3 (a), Inj1–Int4 (b), Inj2–Int3 (c), and Inj2–Int4 (d), according to Table 4.1. . . .	58
4.3	Overview of the volume considered in the forward model and the boundary conditions (BCs). The geometry of the S3 faults is simplified to planes, and the fractures intercepted by the injection intervals are illustrated as plane ellipses. . . . .	59
4.4	Orientations of the structures between the fault cores of the S3 shear zones in the injection boreholes observed from optical televiewer logs (Krietsch et al., 2018) as well as the calculated orientations for the fracture sets applied for the conceptual model. . . . .	62
4.5	Comparison of the observed pressure response with the simulation of the hydraulic tomography experiment for the posterior DFN realizations for injection in the intervals Inj1–Int3 (a), Inj1–Int4 (b), Inj2–Int3 (c), and Inj2–Int4 (d), according to Table 4.1. . . . .	65
4.6	Evaluation of the results from the fracture probability map (a) and the mean hydraulic aperture (b) for different cross sections ( $z$ ). . . .	67

A.1	Range and quantiles of the fracture parameters $x$ (a), $y$ (b), $z$ (c), and fracture length (d) as results from the inversion with a fixed number of fractures for the base test case compared to the value used to set up the test case. . . . .	79
A.2	Histogram of the inversion results of the $z$ -coordinate (a) and the length (c) of fracture 4 and correlation between both parameters (b).	80





# List of Tables

1.1	Overview of studies concerning the characterization of fractured media, the input data, i.e., hydraulic (HT), pneumatic (PT), or tracer (TT) tomography, the inversion approach, and the evaluation of the results. . . . .	6
2.1	List of geometric constraints, experimental and inversion parameter settings. . . . .	19
3.1	Overview of the characteristics of each test case. . . . .	40
3.2	Steps required for the setup of the inversion problem, and parameters estimated by the inversion. . . . .	44
3.3	Parameter setting of the inversion model. . . . .	45
4.1	Parameters of the packer intervals and the hydraulic tomography experiments. . . . .	57
4.2	Uniform prior distributions defined by a minimum and maximum possible value. . . . .	63



# 1 Introduction

## 1.1 Fracture networks

Fractures represent the preferential pathways for flow and transport in an otherwise intact rock matrix. They often form a network that provokes a complex flow field depending on the size, geometry and connectivity of fractures, and the permeability of the matrix. Despite the challenge to resolve these networks and to reliably describe their hydraulic properties, fractured sites are the target for various applications in hydrogeology and engineering, such as water resources, geothermal energy, or nuclear waste repositories. For instance, fractured aquifers host important freshwater reservoirs worldwide (Chandra et al., 2019; Spencer et al., 2021; Wilske et al., 2020). At the same time, open fractures are also the main conduits for contaminant transport affecting groundwater resources (Hadgu et al., 2017; Neuman, 2005). As another example, the construction and operation of enhanced geothermal systems relies on well-connected fracture networks by generating new fractures or by opening already existing fractures through hydraulic, thermal, or chemical stimulation (Kittilä et al., 2020; Vogler et al., 2017; Watanabe et al., 2017). Moreover, the appearance and properties of fracture networks are crucial for the evaluation of potential sites for a nuclear waste repository (Follin et al., 2014; Li et al., 2022), and for the description of an excavation-induced damaged zone around tunnels and openings (Armand et al., 2014; de La Vaissière et al., 2015). In all these different application areas, models and in particular specialized high-fidelity simulation tools are elementary for understanding subsurface processes. Especially for case-specific evaluation and engineering, the applicability of these models depends on the reliability of fractured site characterization.

Fractures are mechanical discontinuities with a predominant direction, i.e., a void space confined on two sides by the surface of the intact rock. The length of a fracture can extend to several orders of magnitude while the opening of a fracture, which is the so-called fracture aperture, is small compared to the length. Therefore, the geometry of individual fractures is approximated as planar two-dimensional (2D) objects in a three-dimensional (3D) rock matrix (Adler et al., 2013; Berre et al., 2019). The aperture of a fracture depends on the properties of the rock surfaces. Their fluctuations determine the local aperture distribution and are commonly described by statistical methods, that is a Gaussian probability density function of the surface fluctuations with the surface roughness as standard deviation, an autocorrelation function describing the nature of each surface, and an intercorrelation function to relate the fluctuations of the upper and lower surface (Adler et al., 2013; Vogler et al., 2017).

The geometric properties of fracture networks are characterized by the fracture intensity, the network connectivity, and the spatial correlation of the properties of individual fractures, mainly the aperture, length, and orientation of fractures (Berkowitz, 2002). The parameters of the fracture network can be described by statistical distributions, such as the power law distribution (Bour and Davy, 1997; de Dreuzy et al., 2012; Hyman et al., 2019). Thereby, the term fracture network implies an impervious or low-permeable rock matrix, such as crystalline rock or bedrock formations. In contrast to that, a fractured porous media has a non-negligible matrix permeability (Adler et al., 2013; Berre et al., 2019).

Two general approaches can be distinguished for the implementation of fracture networks in numerical models to simulate flow and transport which are reviewed by Berre et al. (2019) and compared by Hadgu et al. (2017) for two test cases. For the application of the so-called equivalent continuum method, a regular grid of the investigated domain is generated, and the hydraulic properties of the fractures are translated into a permeability tensor and an effective porosity for each element of the grid. Thereby, the fracture network is translated into an equivalent porous media (EPM). In contrast, the hydraulic and structural properties of the fractures are represented directly by applying a discrete fracture network (DFN) method. The fractures are incorporated as lower-dimensional objects in the simulation models. Only the midplane of the fracture is discretized assuming plane fractures and no changes of the fluid pressure and the averaged velocity normal to the plane. In general, the EPM method is better suited especially in terms of computational costs for fracture networks with a high fracture density and for problems where the matrix conductivity cannot be neglected, such as heat transfer. Representing fractures explicitly in flow models allows for a detailed insight into preferential flow paths (Neuman, 2005) and it provides a direct link between the properties of the fracture network and their influence on flow and transport (Hyman et al., 2019; Roubinet et al., 2010). It also enables the resolution of small-scale characteristics such as local variations of fracture lengths, density, and aperture (de Dreuzy et al., 2012). However, the advantages of applying DFNs are only admissible in practice insofar as the DFN parameters are well mapped (Hadgu et al., 2017). Different gradations and combinations of the DFN and EPM approaches are also possible. For example, the discrete fracture matrix approach explicitly discretizes those fractures that are more relevant for flow and transport, while others are replaced by an equivalent permeability (Berre et al., 2019).

In general, flow is governed by mass and momentum conservation, i.e., by the continuity equation and the Navier-Stokes equations. The Navier-Stokes equations are simplified for flow in DFN models by assuming the flow to be confined between two parallel plates with a large ratio between the extensions of the fracture and the fracture aperture. No surface roughness is considered, and the flow is dominated by a small Reynolds number, i.e.,  $Re < 1$ , which refers to a so-called viscous flow behavior. This assumption implies only small changes of the fluid velocity in a fracture plane and a constant pressure normal to the fracture plane (Zimmerman and Bodvarsson, 1996). Errors occur at the inlet and outlet and at the intersections

of fractures. Thereby, a linear relation between the flow rate and the pressure or hydraulic head gradient, which is effective in the fracture plane, is derived analogous to Darcy's law applied for flow in porous media. The flow rate and the pressure gradient are linked by the aperture to the power of three, hence the name cubic law (Berkowitz, 2002; Zimmerman and Bodvarsson, 1996). Inserting the flow rate in the continuity equation and integrating over the fracture aperture leads to a partial differential equation for the pressure diffusion valid in a fracture midplane

$$a\rho S \frac{\partial p}{\partial t} - \nabla_T \cdot \left( a\rho \frac{k_f}{\mu} \nabla_T p \right) = a q. \quad (1.1)$$

$a$  [m] refers to the aperture of a fracture,  $S$  [ $\text{Pa}^{-1}$ ] to the specific storage,  $k_f$  [ $\text{m}^2$ ] to the fracture permeability, and  $q$  [ $\text{kg m}^{-3} \text{s}^{-1}$ ] to a source/sink term depending on the sign of  $q$ . The fluid parameters are the density  $\rho$  [ $\text{kg m}^{-3}$ ] and the dynamic viscosity  $\mu$  [Pa.s]. The pressure  $p$  [Pa] includes the static pressure and the piezometric pressure due to gravitational forces. The fracture permeability  $k_f$  is related to the fracture aperture (Zimmerman and Bodvarsson, 1996). The gradient  $\nabla_T$  is to be applied in the local coordinate system tangential to the fracture plane due to the assumption that no changes of the flow occur normal to the fracture plane. The intersections of different fractures in a fracture network are also governed by the continuity equation. The continuity of the primary variable, in this case, the pressure, and the balance of the secondary variable, in this case, the flow rate, are valid at the intersection of fractures (Reddy and Gartling, 2010). Equation 1.1 does not consider coupling of the flow with geomechanical or heat effects, such as fracture opening or a temperature dependent density or viscosity.

In order to consider realistic fracture properties and deviations from the flow model, the concept of the so-called hydraulic apertures needs to be applied (Berre et al., 2019). The average aperture of a fracture is easy to determine, while the hydraulic aperture is estimated by experiments such as pumping tests or with air permeameters. The hydraulic aperture of a fracture accounts for a more reasonable flow rate due to filling materials inside a fracture or the surface roughness. In most cases, the hydraulic aperture is smaller than the average aperture and in case a good estimate of the hydraulic aperture is available, this value should be applied for the calculation of the fracture permeability.

A review of the validity of the assumptions, i.e., cubic law and viscous flow, and an extension of the method are examined by Oron and Berkowitz (1998), Brush and Thomson (2003), and Fang and Zhu (2018). Oron and Berkowitz (1998) derived an estimation of the Reynolds number that depends on the geometry as limiting condition for the applicability of the cubic law. Brush and Thomson (2003) compared the solution of Navier-Stokes, Stokes, and local cubic law equations for fractures with different wall geometries, and Fang and Zhu (2018) developed a model based on a local Reynolds number using either Darcy's law (viscous flow) or the Forchheimer equation (inertial and viscous flow).

## 1.2 Tomography experiments for fractured sites

The characterization of the structural and hydraulic properties of fractured rocks is a challenging topic due to the difficulty of identifying single fractures, the complexity of fracture connectivities, and the high costs of specialized measurement techniques. A general understanding of fractured sites, such as fracture intensities or prevalent fracture orientations, is derived by analyzing outcrops or evaluating the parameters of fractures intercepted by boreholes with borehole samples or optical or acoustic viewers (Armand et al., 2014; Barthélémy et al., 2009; Chandra et al., 2019; Follin et al., 2014; Ishibashi et al., 2016; Krietsch et al., 2018; Ma et al., 2022; Massiot et al., 2017; Pavičić et al., 2021; Ren et al., 2018; Shakiba and Doulati Ardejani, 2022; Tan et al., 2020; Yin and Chen, 2020). Single- and cross-borehole pumping or tracer tests characterize the permeability surrounding a borehole interval (Brixel et al., 2020a; Ren et al., 2018), the permeability of the connection between several intervals (Brixel et al., 2020b; Chuang et al., 2017; de La Vaissière et al., 2015; Le Borgne et al., 2006; Jalali et al., 2018), the velocity distribution (Hyman et al., 2019; Kang et al., 2015), transport properties (Cvetkovic et al., 2010; Cvetkovic and Cheng, 2011; de La Bernardie et al., 2018; Kittilä et al., 2019), or the effects from hydraulic stimulation (Amann et al., 2018; Kittilä et al., 2020). Moreover, they are applied for constraining the hydraulic properties of simulation models (Cvetkovic et al., 2007; Follin et al., 2014; Frampton and Cvetkovic, 2010; Li et al., 2022; Tiedeman et al., 2010).

The results from these studies can serve as prior information and constraints for the application of tomography experiments that provide an estimate of the properties between boreholes. The common principle of all tomographic methods is the perturbation of the investigated system by injecting, e.g., a flow rate, tracer, or an electric current. The provoked responses are recorded by several nearby receivers. The aim of the tomography experiments is to determine a relation between the measured signals and the quantity of interest which is, in most cases, the permeability of the fractures or the porous media.

Geophysical methods, such as stress-based tomography, seismic reflection, or ground penetrating radar (Afshari Moein et al., 2018; Chandra et al., 2019; Deparis et al., 2008; Doetsch et al., 2020; Dorn et al., 2011, 2012; Robinson et al., 2016; Voorn et al., 2015), provide only an implicit link between the permeability and the measured signal (Day-Lewis et al., 2017). A summary of various geophysical technologies suitable for the characterization of fractured media, the measured properties, and their potential target application is given by Day-Lewis et al. (2017). In contrast to this, so-called invasive tomographic methods apply a hydraulic or pneumatic overpressure or tracer injections, such as salt, dye, or heat. Thereby, the interpretation of the signals is both clearer and the relation between the pressure responses or the tracer breakthrough curves, and the permeability is easier to determine. A combination of invasive and geophysical measurements can also be realized (Chen et al., 2006; Dorn et al., 2013; Giertzuch et al., 2021a,b).

Especially fractured sites pose a challenge for the application and interpretation

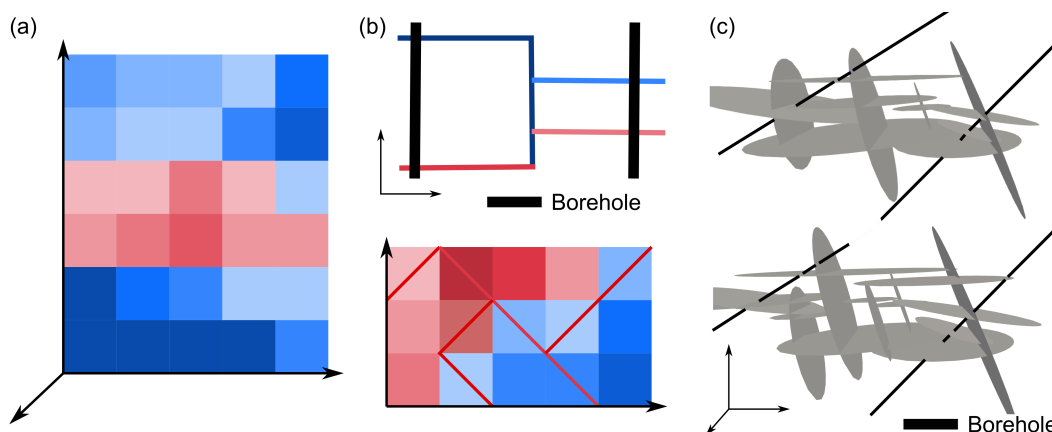


Figure 1.1: Illustration of evaluation methods of tomography experiments from different artificial examples, (a) continuous tomogram, (b) simplification of the fracture structure according to predefined orientations or connectivity, (c) simplification of the fractured rock based on a DFN model. The colors indicate the evaluated hydraulic parameter. Lines mark 2D fracture structures, ellipses 3D fracture structures.

of tomography experiments due to the sharp contrast between permeable fractures and the surrounding rock matrix. In general, the data from the tomography experiments can be evaluated as EPM over the investigated volume, by a simplification of the fracture structure, or as DFN which is summarized schematically in Fig. 1.1. An EPM approach results in a 2D or 3D tomogram of the hydraulic conductivity (**C**) or diffusivity (**D**) distribution and, for some studies, also a specific storage (**S**) distribution as illustrated in Fig. 1.1a. The evaluation of the element-wise fracture density is also possible with the EPM representation. The properties of the fractured rock can be inferred more directly by simplifying the structural properties of the fractures (Fig. 1.1b) as connectivity structure between borehole intervals (Klepikova et al., 2014, 2020) or by the cell-wise adaption of the parameters of linear structures (Fischer et al., 2017b, 2018a,b). The hydraulic parameters of the simplified DFN structure are calibrated with the measured data. Only 2D properties are inferred by these studies, thereby, neglecting the propagation of flow in the third dimension. The application of a DFN model and the inversion of the hydraulic and structural properties of the DFN resolves the fractured rock more detailed as shown in Fig. 1.1c (Ringel et al., 2019, 2021; Somogyvári et al., 2017, 2019). However, this approach also requires assumptions and simplifications, e.g., about the fracture shape or the fracture orientations. Due to the large number of unknown parameters, an unequivocal relation between the measured signals and the fracture properties is usually not possible.

Table 1.1 gives an overview of studies concerning the characterization of fractured media applying hydraulic, pneumatic, or tracer tomography with an emphasis on the representation of the fracture properties in the evaluation of the results.

Table 1.1: Overview of studies concerning the characterization of fractured media, the input data, i.e., hydraulic (HT), pneumatic (PT), or tracer (TT) tomography, the inversion approach, and the evaluation of the results.

Site/ Application	Study	Input data	Inversion method	Inversion results
Blair Wallis (USA)	Ren et al. (2021)	Transient HT	Simultaneous SLE	<b>C</b> , <b>S</b> , and <b>D</b> tomogram
Göttingen (Germany)	Liu et al. (2022) Yang et al. (2020)	Thermal TT Transient HT	Travel time Travel time	<b>C</b> tomogram <b>D</b> tomogram
Grimmel (Switzerland)	Kittilä et al. (2020) Klepikova et al. (2020) Ringel et al. (2022)	Dye TT Transient HT Transient HT	Travel time Nelder-Mead optimization MCMC	<b>C</b> tomogram before and after stimulation Transmissivity/ storativity of interval connectivity structure Structural and hydraulic properties of 3D DFN
Manitoba (Canada)	Park et al. (2004)	Steady-state HT/ TT	Transition probability geostatistics	Stochastic EPM with five facies representing different fracture densities (sparsely to highly fractured), calibrated hydraulic conductivity and effective porosity
Mizunami (Japan)	Illman et al. (2009) Zha et al. (2015) Zha et al. (2016) Zha et al. (2017)	Transient HT Transient HT Transient HT Transient HT	Sequential SLE Simultaneous SLE Simultaneous SLE SLE	<b>C</b> and <b>S</b> tomogram <b>C</b> and <b>S</b> tomogram <b>C</b> and <b>S</b> tomogram <b>C</b> and <b>S</b> tomogram



Site/ Application	Study	Input data	Inversion method	Inversion results
Olkiluoto Island (Finland)	Blessent et al. (2011)	Steady-state HT	Transition probability geostatistics	Stochastic EPM with four facies representing different fracture densities (sparsely to highly fractured), calibrated hydraulic conductivity
	Dorn et al. (2013)	Steady-state HT/ TT	Hierarchical rejection sampling	Connectivity and effective transmissivity of DFN
Ploemeur (France)	Klepikova et al. (2014)	Thermal TT/ steady-state HT	Optimization	Transmissivity of interval connectivity structure
	Fischer et al. (2017b)	Steady-state HT	Optimization	Hydraulic conductivity of a discrete conduit and the background matrix
Terrieu (France)	Fischer et al. (2018a)	Oscillatory HT	Interpretation of amplitude/ phase offset	Interpretation of the connection between boreholes as conduit, matrix, or dual
	Fischer et al. (2018b)	Oscillatory HT	CADI	Transmissivity/ storativity of conduits and the background matrix
Fischer et al. (2020)	Fischer et al. (2020)	Steady-state HT	Optimization	Transmissivity of a simplified DFN structure and the background matrix
	Wang et al. (2016)	Steady-state HT	Optimization	Transmissivity tomogram
Wang et al. (2017)	Wang et al. (2017)	Steady-state HT	Transition probability geostatistics	Stochastic EPM with three facies (karst, fracture, bedding), calibrated transmissivity

Site/ Application	Study	Input data	Inversion method	Inversion results
Waiwera aquifer (New Zealand)	Somogyvári et al. (2019)	Borehole temperature	MCMC	Structural properties of 2D DFN
West Trenton (USA)	Tiedeman and Barrash (2020)	Transient HT	Geostatistical inversion	<b>C</b> tomogram and fracture connectivity
Laboratory studies	Brauchler et al. (2003)	Transient PT	Travel time	<b>D</b> tomogram
	Brauchler et al. (2013a)	Gas TT	Travel time	Interstitial velocity distribution
	Poduri et al. (2021)	Transient HT	Kriging based pilot-point inversion	<b>C</b> and <b>S</b> tomogram
	Sharmeen et al. (2012)	Transient HT	Sequential SLE	<b>C</b> and <b>S</b> tomogram
	Zhao et al. (2021)	Transient HT	Sequential SLE	<b>C</b> and <b>S</b> tomogram

Site/ Application	Study	Input data	Inversion method	Inversion results
2D synthetic test case	Dong et al. (2019)	Transient HT	Simultaneous SLE	<b>C</b> and <b>S</b> tomogram
	Fischer et al. (2017a)	Steady-state HT	CADI	Hydraulic conductivity of a discrete conduit and the background matrix
	Fischer et al. (2018c)	Steady-state HT	Optimization	Transmissivity of a simplified DFN structure and the background matrix
	Hao et al. (2008)	Transient HT	SLE	<b>C</b> and <b>S</b> tomogram
	Le Goc et al. (2010)	Steady-state HT	Hierarchical optimization	Transmissivity of flow channels and background matrix
	Ma et al. (2020)	Transient HT	Stochastic multi-scale inversion	Structural properties of major fractures and stochastic parameters of minor fractures
	Ringel et al. (2019)	Transient HT/ TT	MCMC	Structural properties of DFN
	Somogyvári et al. (2017)	TT	MCMC	Structural properties of DFN
	Vu and Jardani (2022)	Steady-state HT	Convolutional neural network	Structural properties of DFN
	3D synthetic test case	Cliffe et al. (2011)	Steady-state HT	Basis vector/ Bayesian conditioning
Ringel et al. (2021)		Transient HT	MCMC	Structural and hydraulic properties of DFN

Table 1.1 shows that most studies rely on continuous tomograms instead of an explicit representation of the fractured media. Figure 1.2 groups the fractured sites (Table 1.1) based on the scale of the investigated region and the resolution of the properties of the fractured rock by the evaluation of the tomography experiment. The resolution is categorized generally based on the different evaluation methods that are illustrated in Fig. 1.1. Further, the studies are arranged according to the dimension of the results and the evaluated parameters. On a meter-scale, the conductivity tomograms are not able to delineate the strong heterogeneity of the permeability distribution provoked by the appearance of a fracture network. This problem can be overcome by particle transport simulations to investigate the fracture connectivity (Tiedeman and Barrash, 2020), the comparison with forward simulations of synthetic test cases with similar properties as the site (Sharmeen et al., 2012; Zha et al., 2015; Zhao et al., 2021), or the incorporation of specific prior knowledge (Poduri et al., 2021; Zha et al., 2017; Zhao et al., 2021). Inversion approaches resulting in continuous tomograms have an advantage characterizing kilometer-scale sites where the influence of single fractures is smaller (Blessent et al., 2011; Illman et al., 2009; Zha et al., 2015, 2016, 2017) or porous aquifers such as in sedimentary rock (Berg and Illman, 2011; Brauchler et al., 2013b; Cardiff and Barrash, 2011; Cardiff et al., 2012, 2013, 2019; Jardani et al., 2013; Jiménez et al., 2013; Sánchez-León et al., 2020b; Somogyvári and Bayer, 2017; Zha et al., 2018; Zhao and Illman, 2017; Zhao et al., 2019).

### 1.3 Inverse problems

In general, forward or inverse problems provide a relation between experimental data and the parameters that are the quantity of interest to be estimated by the experiments. Therefore, such problems comprise the following elements: the input data  $\mathbf{d}$  is obtained from observations or measurement campaigns, the model  $f$  describes the present system that depends on a vector of model parameters  $\theta$  (Aster et al., 2018). The elements of the system are linked by

$$f(\theta) = \mathbf{d}, \quad (1.2)$$

whereby  $f(\theta)$  refers to the evaluation of the mathematical model or forward operator based on the parameter vector  $\theta$  (Aster et al., 2018). Depending on the problem, the forward operator can be an ordinary or partial differential equation, or a system of equations. For most applications, the input data contains observation errors or measurement noise, such that the signals consist of the perfect outcome of an experiment  $\tilde{\mathbf{d}}$  and noise  $\epsilon$

$$\mathbf{d} = \tilde{\mathbf{d}} + \epsilon. \quad (1.3)$$

Equation 1.2 is a so-called forward problem, that is, the results of an experiment are calculated based on the model parameters. Thereby, errors are introduced by assumptions applied to reduce the number of model parameters, simplifications of

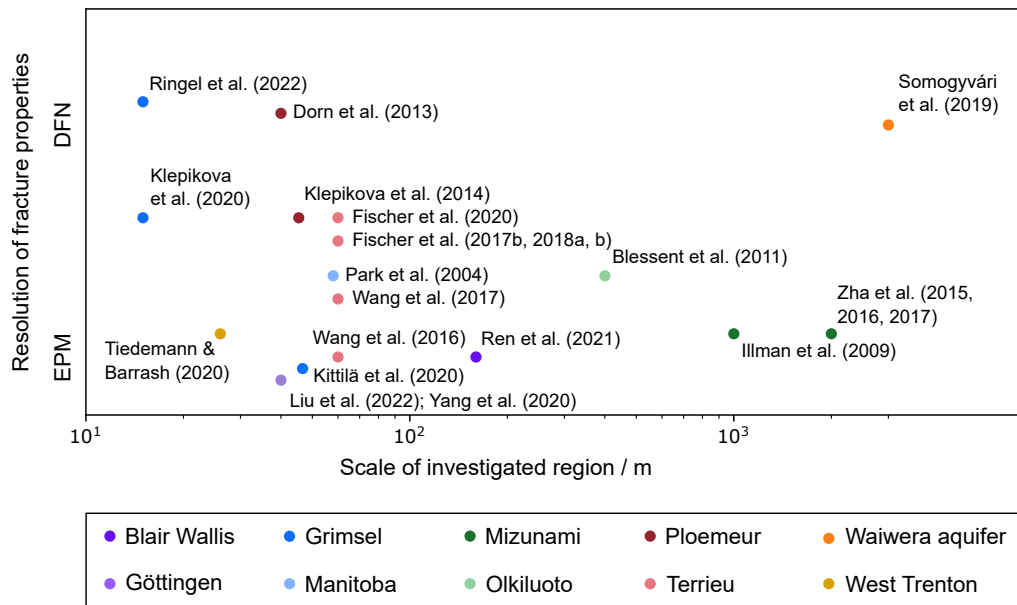


Figure 1.2: Classification of the field studies (Table 1.1) concerning the characterization of fractured sites according to the scale of the investigated region and the resolution of the fracture properties by the inversion results.

the underlying physics, or by the discretization of the differential equation in a numerical model.

Vice versa to the forward problem, an inverse problem deals with finding the model parameters given the input data (Aster et al., 2018). Several difficulties arise for the computation of inverse problems in practice. The number of parameters describing a model is often large, making the solution computationally expensive. Moreover, the forward operator is not invertible for most applications, therefore, an inverse problem cannot be solved by inverting Eq. 1.2. In addition, there may be no parameter set that fits the input data exactly. This is the case for data containing measurement errors (Eq. 1.3) or for simplified models. On the contrary, a large number of model parameters  $\theta$  can fit the perfect data without noise  $\tilde{\mathbf{d}}$  (Aster et al., 2018).

Depending on the input data, the forward model, and the scale of the investigated domain, different methods for the solution of inverse problems, which is the evaluation of tomography experiments, are feasible. The most common methods in hydrogeology are different deterministic approaches, geostatistical methods, and stochastic sampling methods. The input data, i.e., the type of tomography experiment, and the inversion approach are summarized for each study and site in Table 1.1.

A deterministic solution is derived by minimizing the misfit between the measured

data and the results from the forward simulation according to Eq. 1.2 and, therefore, one parameter vector can be evaluated. The optimization is implemented generally as an iterative process of updating the parameter vector such that the experiment data matches the results of the forward simulation. Depending on the system and the parameter set for the inversion, different approaches are possible, such as the cellular automata deterministic inversion (CADI) method that is adapted for the work with linear structures (Fischer et al., 2017a,b), or the Nelder-Mead optimization method (Klepikova et al., 2020).

Travel time inversion is a specific type of deterministic inversion. The concept was adapted from seismic tomography to invasive tomography. The basis is a relation between the travel time of the measured signal and the line integral of the reciprocal of the diffusivity (Brauchler et al., 2003). For advection-driven problems, such as heat transfer or tracer transport, the diffusivity can be replaced by the application of Darcy’s law, i.e., porosity, permeability, and pressure gradient (Vasco and Datta-Gupta, 1999). For the inversion of hydraulic tomography data, the first derivative of the pressure or hydraulic head response is applied (Brauchler et al., 2013b). To distinguish preferential flow paths and reduce the effects of diffusion, early-time diagnostics can be applied for thermal and hydraulic tomography (Somogyvári et al., 2016). The travel time is recorded at each receiver which functions as the input data for the solution of the inverse problem. The investigated domain is discretized and the trajectory length of the signal through each element is calculated, which depends on the material properties of each element. Then, the material parameters are adapted iteratively to match the observed travel times.

A stochastic approach is capable of finding several solution parameter vectors, such that the statistical properties of the model parameters can be analyzed. This is based on the Bayesian equation that relates the conditional probability of the model parameters, given the input data, to the a priori known information and the likelihood of the data, given a parameter vector. In general, the mean quantity of interest and a variance or uncertainty of the results can be evaluated. The sequential or simultaneous successive linear estimator (SLE) and the pilot-point inversion applied in the studies in Table 1.1 are variogram-based geostatistical estimation methods (Poduri et al., 2021; Tiedeman and Barrash, 2020; Zha et al., 2015; Zhu and Yeh, 2005). The element-wise hydraulic conductivity and specific storage are formulated as mean value plus a stochastic perturbation. The estimate of the parameters is updated iteratively by comparing the simulated with the observed response from the tomography experiment. The error is weighted by a coefficient matrix that depends on the covariance and cross-covariance matrix (Zha et al., 2015; Zhu and Yeh, 2005). The residual covariance matrix is also updated during the inversion. Additional data sets can be included either sequentially or simultaneously.

A different stochastic approach is the transition probability geostatistical method. Thereby, the generation of realistic geological formations is in the focus of this approach. The basis are different rock types, so called rock facies, which vary from sparsely fractured to highly fractured, defined from ranges of fracture frequency or fracture density. The observed transition rates are calculated from borehole logs and

the properties of a Markov chain are fitted to match the observed transition rates. This is applied to simulate different rock facies distributions over the experimental volume. In a next step, the hydraulic conductivity of each facies is calibrated with the pressure, flow rate, or concentration data.

Sampling methods, such as Markov chain Monte Carlo (MCMC) (Ringel et al., 2019, 2021, 2022; Somogyvári et al., 2017, 2019) or Monte Carlo (MC) rejection sampling (Dorn et al., 2013), characterize the posterior distribution given by the Bayesian equation by generating samples from the distribution. The sampling operates according to a proposal function in case of MCMC or based on the prior distribution for MC. The proposal function can include a transdimensional update that changes the number of parameters (Green, 1995).

## 1.4 Objective and outline of this study

The overall objective of this research project is the development of an innovative method for the inversion of fractured sites. This approach should enable the characterization of fractured rocks with more detail than available continuous evaluation methods or simplified connectivity structures. For this purpose, the properties of the fractured rock are represented directly as DFN in the forward simulations and the parameter vector of the inverse problem. The observed pressure signals or tracer breakthrough curves are not sufficient, and the parameter set describing the system is too large to implement a deterministic solution method. Therefore, a stochastic sampling method is applied to consider the non-uniqueness of the inverse problem. The stochastic approach is reflected also in the results that are evaluated as fracture probability map and mean hydraulic aperture.

The previously conducted work regarding the inversion of 2D DFNs is summarized and extended in Chapter 2. The goal of this part of the thesis is the evaluation of suitable input data for the inversion. This is achieved by a synthetic DFN test case and by comparing the inversion results obtained from two different types of tomography experiments, in this case, hydraulic and tracer tomography.

Based on the insights from the work with 2D DFNs, a forward model and inversion algorithm for 3D DFNs are introduced in Chapter 3. The objective of Chapter 3 is testing the 3D DFN inversion procedure with several synthetic test cases. Therefore, the configuration of the tomography experiments and setup of the inversion problem are varied and the specifics of the inversion results are evaluated.

Chapter 4 demonstrates the applicability of the developed inversion method to a fractured field site. The approach is implemented to characterize the structural and hydraulic properties of the highly fractured zone at the Grimsel Test Site in Switzerland with hydraulic tomography experiments that were conducted as part of the In situ Stimulation and Circulation measurement campaign.





## 2 Comparison of hydraulic and tracer tomography for discrete fracture network inversion

### Abstract

Fractures serve as highly conductive preferential flow paths for fluids in rocks, which are difficult to exactly reconstruct in numerical models. Especially, in low-conductive rocks, fractures are often the only pathways for advection of solutes and heat. The presented study compares the results from hydraulic and tracer tomography applied to invert a theoretical discrete fracture network (DFN) that is based on data from synthetic cross-well testing. For hydraulic tomography, pressure pulses in various injection intervals are induced and the pressure responses in the monitoring intervals of a nearby observation well are recorded. For tracer tomography, a conservative tracer is injected in different well levels and the depth-dependent breakthrough of the tracer is monitored. A recently introduced transdimensional Bayesian inversion procedure is applied for both tomographical methods, which adjusts the fracture positions, orientations, and numbers based on given geometrical fracture statistics. The used Metropolis-Hastings-Green algorithm is refined by the simultaneous estimation of the measurement error's variance, that is, the measurement noise. Based on the presented application to invert the two-dimensional cross-section between source and the receiver well, the hydraulic tomography reveals itself to be more suitable for reconstructing the original DFN. This is based on a probabilistic representation of the inverted results by means of fracture probabilities.

### 2.1 Introduction

Tomographic methods are specifically suited for characterizing the spatial heterogeneity of aquifers. They are based on the inversion of signals recorded among multiple sources and receivers, which are employed to infer two-dimensional (2D) or three-dimensional (3D) images of spatial hydraulic parameter distribution. For identifying those structural characteristics relevant for groundwater flow, solute and heat transport, invasive concepts are available that apply hydraulic (Berg and Illman, 2011; Brauchler et al., 2013b; Cardiff et al., 2012; Illman, 2013; Jiménez et al., 2013; Zha et al., 2018) or pneumatic pressure (Hu et al., 2015, 2016; Ni and Yeh, 2008; Vesselinov et al., 2001), or that use tracers such as dye (Datta-Gupta et al., 2002; Jiménez et al., 2016; Ma et al., 2012), salt (Doetsch et al., 2012; Jardani et al.,

2013; Jougnot et al., 2018; Singha and Gorelick, 2005) or heat tracers (Hermans et al., 2015; Klepikova et al., 2014; Schwede et al., 2014; Somogyvári et al., 2016). In comparison to many alternative near-surface geophysical applications, these signals are rarely introduced from the ground surface. Instead, pressure and tracer tomograms are typically recorded between boreholes by cross-well testing. For example, Bohling et al. (2007), Brauchler et al. (2013b), Cardiff et al. (2013), and Paradis et al. (2016) applied short-term pumping or slug tests in different well intervals or levels, which are isolated by packers. Tomographic data sets for two- or three-dimensional inversion of aquifer heterogeneity were obtained by recordings from pressure sensors in adjacent observation wells. In contrast, tracer tomography as presented by Jiménez et al. (2016) for solutes and by Somogyvári and Bayer (2017) for heat, is based on multi-level injection of tracers. Here, the tracer breakthrough curves (BTCs) recorded in adjacent observation wells serve as input for spatial inversion procedures.

Most available tomographic inversion methods are especially suitable for reconstruction of smoothly changing hydraulic properties such as those often found in sedimentary deposits (Berg and Illman, 2011; Hu et al., 2011; Jiménez et al., 2013; Tso et al., 2016; Zha et al., 2018; Zhao et al., 2015). In comparison, fractured aquifers commonly exhibit sharp contrasts between highly conductive fractures and a low-permeable matrix. Tomograms generated with classical smoothing algorithms such as the successive linear estimator thus provide a blurred visualization of hydraulic properties, and they roughly estimate fracture locations or connectivity (Dong et al., 2019; Hao et al., 2008; Illman et al., 2009; Illman, 2013, 2015; Wen et al., 2019; Zha et al., 2015). As alternatives, a hybrid procedure was presented by Wang et al. (2017), and a travel-time based approach by Brauchler et al. (2013a) for exploring trend and location of highly conductive channels. All these inversion techniques, however, similarly pixelate the spatial hydraulic properties and thus offer limited insight into the geometric properties of fractures.

Due to that, we chose to rely on a discrete fracture network (DFN) approach since this method is more realistic when emphasizing the features of a DFN and the connectivity of the fracture network. In contrast, equivalent continuum models can be appropriated to characterize rocks with a high fracture intensity. In this case, the approximation of the rock as highly heterogeneous porous medium holds. However, the DFN case study presented in this paper deals with a small number of fractures. Another significant advantage of the DFN approach is that this method allows for an easier observance of a priori known statistical information such as fracture inclination and fracture intensity.

Recently, concepts have been introduced that focus on a discrete representation of inverted fractures. For example, Fischer et al. (2017b) introduced a method based on the use of the Cellular Automata concept for deterministic inversion of linear structures and applied it to systems with fractured and karstic conduits (Fischer et al., 2018b,c). Klepikova et al. (2014) calibrated DFNs with given horizontal and vertical fracture orientations mainly for investigating fracture connectivity, but not for adjustment of fracture network geometry. The method by Somogyvári et al. (2017)

iteratively tunes geometric fracture properties in order to match tomographic tracer measurements. Based on synthetic DFN examples, fracture probability maps were generated, which reveal a good reliability of inverted results for simple networks, but a minor capability for locating single fractures in complex networks. This demonstrates not only the highly demanding inversion problem when adjusting individual fractures in a network, but it also highlights the growing data demand of accurate tomographic inversion, with increasing network complexity.

Improved tomograms can be achieved by increasing source-receiver density, by optimal and full usage of information of measured data instead of, for example, utilizing trends and characteristics of response data only, and by combining different measurements that deliver complementary data. For better delineation of fracture flow paths, the combined use of salt tracer and electrical resistivity tomography (Singha and Gorelick, 2005), of salt tracer and ground penetrating radar (Dorn et al., 2011), as well as of nanoscale zero-valent iron tracer and flowmeter testing (Chuang et al., 2017) have been proposed. Combining different methods, however, also raises efforts and cost of field investigation campaigns. Moreover, comparison or coupling of different data inversions escalate the requirements for the tomographic inversion procedure.

The presented work builds upon the DFN inversion procedure by Somogyvári et al. (2017). The objective is to further develop the tomographic reconstruction of discrete fractures by comparing the results from tracer-based inversion to that based on hydraulic pressure signals. Our inversion procedure is assigned to the stochastic methods. Therefore, the probabilistic characteristics of the results will be the same for different inversion runs. Nevertheless, individual results will change, although we use the same input data. In contrast, deterministic approaches (e.g. Klepikova et al., 2014) will produce the same results for every inversion run using the same input parameters. In the following, the underlying Bayesian inversion procedure is first described and improved. Then a synthetic case study is introduced for testing the different tomographic concepts.

## 2.2 Methodology

The following section starts by introducing our case study, its geometrical parameters, and the settings of the experiment. The reconstruction of the DFN is done by transdimensional inversion, which is explained in the following part. We present a method that deals with noisy observation data at the end of this section.

### 2.2.1 DFN case study

A synthetic 2D DFN model is used for testing the inversion procedure. It is set up based on the fracture geometry of the Tschingelmad outcrop in the central Alps (Ziegler et al., 2013). The simplified cross-section shown in Fig. 2.1 provides different preferential flow paths between the given three source and three receiver points, and hence represents an ideal example to test the specific capabilities of different

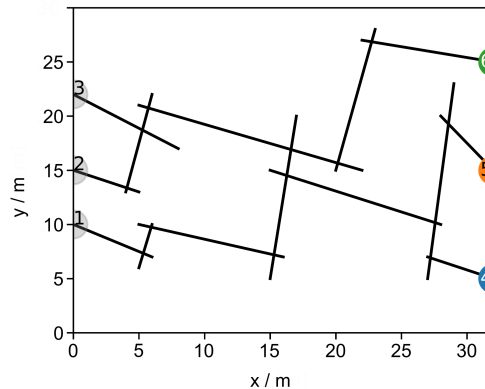


Figure 2.1: Synthetic discrete fracture network with three injection points (number one to three) and three receiver points (number four to six) based on an outcrop in Switzerland. It contains two fracture sets with two different fracture angles and fracture apertures.

tomographic methods. The sources on the left side may be interpreted as packed vertical intervals of a well, where tracer or pressure signals are introduced. The receiver points on the right represent measurement points in an imaginary observation well. By systematic characterization of the fractures adjacent to the source and receiver wells and with the aid of packer tests, one could isolate only conductive and connective fractures and realize such tests also in practice. For the subsequent tomographic inversion, it is assumed that the profile in Fig. 2.1 can be reproduced by the definition of two fracture sets. These sets differ with respect to the fracture orientation and aperture as given in Table 2.1. These properties of the fracture sets and the fracture length distribution (FLD) are geometric constraints of the inversion. Within these constraints, the inversion procedure will explore suitable fracture combinations.

Theoretical experiments are simulated with different source signals to obtain receiver data that is used for the inversion to calibrate the DFN. The details of these experiments are summed up in Table 2.1. Hydraulic tomography is simulated with a series of independent pumping tests, using a Heaviside injection pressure signal (transient flow condition). Tracer tomography is simulated in a similar hydraulic regime as in the hydraulic tomography case. Water is injected in the source wells using the same pressure gradient between the source and receiver wells as for the hydraulic tomography. We wait until the flow stabilizes after the injection of water., i.e. until the velocity field is stable (steady-state flow condition), before any tracer injection is applied. The tracer is injected continuously, with a constant concentration, until the termination of the experiment.

To simulate the pressure signals and tracer breakthroughs, a fast and robust forward model is implemented. Darcy flow, which relates the pressure gradient to the

Table 2.1: List of geometric constraints, experimental and inversion parameter settings.

Category	Parameter	Fracture set 1	Fracture set 2
Geometric constraints	Fracture inclination ( $^{\circ}$ )	-19.48	74.48
	Fracture aperture (mm)	1.5	1
	FLD-mean (m)		9.9
	FLD-variance ( $\text{m}^2$ )		8.5
Experimental parameter settings	Injection pressure (Pa)		$3 \cdot 10^5$
	Injection concentration ( $\text{mg l}^{-1}$ )		40
Inversion parameter settings	Discretization (m)		1
	$p_{\text{add}}/p_{\text{del}}/p_{\text{shift}}$		0.4/0.4/0.2
	Number of iterations		100,000

velocity, and the continuity equation are used to calculate the pressure diffusion in the fracture network. The fracture aperture indicates the hydraulic conductivity due to Cubic law. The intersection between two or more fractures is considered by mass conservation. These equations are solved numerically by a finite difference approach with first-order accuracy in time and second-order accuracy in space (Afshari Moein et al., 2018; Jalali, 2013). We use an implicit time integration method which is unconditionally stable. The advection-dispersion equation is solved numerically considering the steady state velocity field. The numerical solution of the equation produces the concentration field of the experiment in the DFN. By monitoring the concentration at specific points we obtain the tracer breakthroughs at the monitoring intervals in the receiver well. The tracer transport is assumed to be conservative, and no loss towards the rock matrix is simulated. The focus of the present study is set on a conservative tracer, but the experiment could also be simulated and inverted with a heat tracer. In the model, heat conduction and heat convection are described by a partial differential equation that has the same form as the advection-diffusion equation. Additionally, however, heat conduction from the water to the rock matrix needs to be taken into account.

### 2.2.2 Transdimensional inversion

The DFN reconstruction is accomplished by using a transdimensional Markov Chain Monte Carlo methodology: the Metropolis-Hastings-Green algorithm (MHG) introduced by Green (1995). The method is also known as reversible-jump Markov chain Monte Carlo (rjMCMC) as it operates with reversible model updates (jumps) that change the problem dimensions. This algorithm was implemented for DFN inversion by Somogyvári et al. (2017).

RjMCMC uses an iterative structure with two main phases per iteration; an update and an evaluation phase. The inversion procedure and the workflow of our

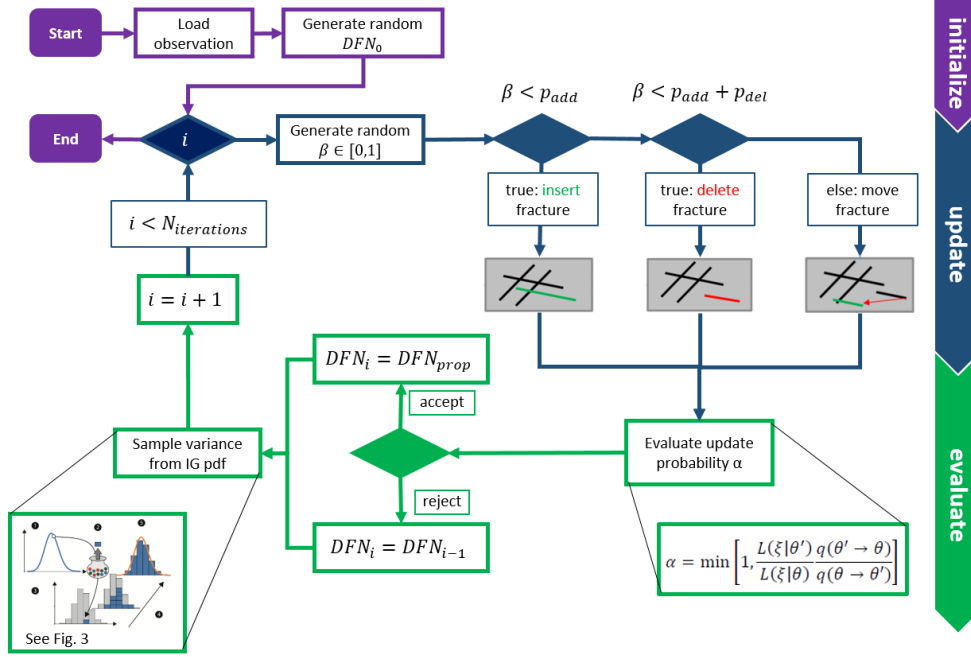


Figure 2.2: Flowchart showing the inversion algorithm with its main phases.

inversion algorithm are described by the flowchart in Fig. 2.2. In the update phase, the parameters of the DFN model are modified by one of the following updates: fracture movement, fracture insertion, and fracture deletion. The DFN model parameter set includes the number of fractures and for each fracture its position, the fracture inclination, and the fracture length. The parameter set of a DFN realization is denoted by  $\theta$ . Since the number of fractures varies through adding or deleting a fracture, the dimension of the parameter space changes, too. This motivates the description of transdimensional inversion. To consider the computational costs of the inversion problem, we estimate the number of fractures during the iterations of the inversion. The number of fractures is in the range of 10 to  $10^2$  and the dimension of the parameter space is three times the number of fractures. These parameters have to be adjusted by the inversion algorithm to reproduce the measured pressure signals or tracer breakthroughs.

The kind of update is selected randomly, with predefined probabilities  $p_{add}$ ,  $p_{del}$ , and  $p_{shift}$ , which may change during the inversion process, e.g. if the fracture intensity is too high. Fracture addition is the so-called birth move of the rjMCMC algorithm. For this update, first the DFN model gets discretized, adhering to a pre-defined spacing distance. This characteristic property of the fractured rock represents the shortest possible distance between two parallel fractures. A set of insertion points is identified based on this distance, where new fractures could be added. The insertion of fractures is only possible starting or intersecting with a given fracture since isolated fractures do not affect the transport. Counting the

number of possible insertion points, we receive the insertion probability  $P_{\text{ins}}$ . The orientation, length, and physical properties of a new fracture are probabilistically chosen, based on the given characteristics of one or more fracture sets. In this study, a fracture set represents fractures with similar physical properties and inclinations (Table 2.1). The choice between different fracture sets is taken into account by the fracture set probability,  $P_{\text{set}}$ . However, further constraints and properties may be defined, depending on the information that is available for a specific case. The fracture length is drawn from the fracture length distribution (FLD) that is assumed for the corresponding fracture set, which gives us the probability of the length of a new fracture,  $P_{\text{length}}$ .

The point of intersection along the fracture (fracture position) is randomly selected after the geometric properties of the fracture are determined. The new fracture is inserted in the field by assigning the fracture position to a random insertion point. We obtain the probability of the position  $P_{\text{pos}}$  where the new fracture intersects the existing DFN according to the number of possible points along the new fracture. The different probabilities, which have a part in the addition probability, are explained in detail in Somogyvári et al. (2017). The resulting probability of fracture addition can be expressed as the product of the individual probabilities of the above-mentioned steps

$$q_{\text{add}} = P_{\text{set}} P_{\text{length}} P_{\text{ins}} P_{\text{pos}}. \quad (2.1)$$

Fracture deletion is the so-called death move of the rjMCMC algorithm. A randomly selected fracture gets deleted from the DFN model when it is applied. This update is constrained, only allowing the deletion of a fracture if the source and receiver points remain connected. This is required to properly run the forward model. The probability of this update reads as the reciprocal of the number of deletable fractures,  $n_{\text{deletable fractures}}$

$$q_{\text{del}} = \frac{1}{n_{\text{deletable fractures}}}. \quad (2.2)$$

$q_{\text{add}}$  and  $q_{\text{del}}$  are the transition probabilities. We receive the probability of the transition from the current DFN realization to a proposed realization by computing them. Therefore,  $q_{\text{add}}$  and  $q_{\text{del}}$  are the conditional probabilities of updating the DFN given the current realization.

Fracture movement is a straightforward update, representing a random perturbation of fracture coordinates. It does not change the dimension of the model parameter space. A fracture is randomly selected in our implementation, and is then shifted to another randomly drawn insertion point while using the same discretization as the fracture addition. Fracture movement updates symmetrically, that is, the probability of the forward and the reverse update is equal. The proposal ratio does not need to be calculated, because the fracture length and the fracture set will not change, i.e., only the likelihood ratio matters. In contrast, the parameters of a new fracture are drawn from the FLD and  $P_{\text{set}}$  if we first delete a random fracture and add a new one in the next iteration. This requires the calculation of the proposal ratio for adding and deleting. Therefore, fracture moving necessitates less compu-

tational costs than adding or deleting. Hence, it is the most efficient update. This type of update is also known as the Metropolis update, as defined by Metropolis et al. (1953).

The DFN model is iteratively adjusted in a loop that is based on the recorded pressure signals or tracer breakthroughs by one of the described updates, as it is shown in the flowchart (Fig. 2.2). A proposed DFN model (denoted by the model parameters  $\theta'$ ) is evaluated while using the MHG acceptance criterion, i.e., the update probability  $\alpha$ , comparing the current DFN realization (denoted by  $\theta$ ) with the proposed DFN realization

$$\alpha = \min \left( 1, \frac{p(\theta')}{p(\theta)} \frac{L(\mathbf{d}|\theta')}{L(\mathbf{d}|\theta)} \frac{q(\theta_{i-1}|\theta')}{q(\theta'|\theta_{i-1})} |J| \right). \quad (2.3)$$

Equation 2.3 is calculated from the product of the prior ratio  $p(\theta')/p(\theta)$ , the likelihood ratio  $L(\mathbf{d}|\theta')/L(\mathbf{d}|\theta)$  the probability of the data given the model parameters, the proposal ratio  $q(\theta_{i-1}|\theta')/q(\theta'|\theta_{i-1})$  and the determinant of the so-called Jacobian matrix  $|J|$ . The prior probability, multiplied by the likelihood function, yields the posterior probability, according to Bayes' theorem. The Jacobian takes the change in the dimension of the parameter space into account, as provoked by fracture addition or fracture deletion. In the presented DFN inversion, the prior ratio is always equal to one, because, aside from the non-informative priors, all prior information is included in the proposal ratio. The likelihood ratio is calculated by dividing the likelihood function of the updated model by the non-updated model. The likelihood of a model can be expressed with the following Gaussian distribution if we assume that the observations are independent and follow a normal distribution

$$L(\mathbf{d}|\theta) = \frac{1}{\sqrt{4\pi\sigma^2}} \exp \left( -\frac{(\mathbf{d} - f(\theta))^2}{2\sigma^2} \right). \quad (2.4)$$

The transdimensional updates of the presented DFN inversion only deal with the discretized model parameter space. New fractures can only be inserted to discrete insertion points, with discretized fracture length distribution. Deleting a fracture from a DFN is also a discrete operation. The Jacobian matrix of these discrete updates is always equal to one (Denison et al., 2002). This makes this inversion approach very efficient, as the transdimensional updates can be evaluated at the same computational cost as updates that do not change the dimension of the parameter space. For the same reason, the fracture spacing discretizes the originally continuous fracture length distribution, since discretized values ensure an easy computation of the Jacobian in the acceptance probability  $\alpha$ , see Eq. 2.3.

The MHG criteria ensure that the Markov chain is stationary, and it samples from the posterior probability distribution of the inverse problem. In our case, the MHG criteria simplify to

$$\alpha = \min \left( 1, \frac{L(\mathbf{d}|\theta')}{L(\mathbf{d}|\theta)} \frac{q(\theta_{i-1}|\theta')}{q(\theta'|\theta_{i-1})} \right), \quad (2.5)$$

which is the same as the acceptance ratio of the Metropolis–Hastings algorithm.



The accepted realization is stored and the Markov chain continues in step. In the case of rejection, the previous model gets restored and it is used for the start of the next iteration. The final result of the inversion is the ensemble of model realizations along the whole Markov chain. However, in practice, the first part of the chain (burn-in phase) is discarded, as these realizations are influenced by the chosen initial model until the chain converges (Brooks et al., 2011).

The likelihood governs the convergence rate of the inversion. In this case, the control parameter of the inversion is a fixed variance  $\sigma^2$  of the normal distribution in Eq. 2.4. Choosing a smaller variance value could enhance the convergence rate, with the risk of trapping the algorithm early in the local minimum. We inspect the acceptance probability  $\alpha$  to study the effect of the variance,  $\sigma^2$ , on the convergence rate in more detail (Eq. 2.5). For this, we test the different settings of the variance. Note that, by changing the variance, only the likelihood ratio  $L_{\text{ratio}}$  is affected, while the proposal and the prior ratio remain constant. First, we consider the case that the error between the observed and the current DFN simulated data decreases through a proposed realization. This yields a likelihood ratio that is greater than one, irrespective of whether a high or a low variance is chosen, and it induces a high acceptance probability.

Second, we suppose the choice of a high variance. The limit of  $(\text{RMS}_{\text{current}}^2 - \text{RMS}_{\text{proposed}}^2) / 2\sigma^2$ , is zero, as  $\sigma^2$  approaches infinite,

$$\lim_{\sigma^2 \rightarrow \infty} \frac{\text{RMS}_{\text{current}}^2 - \text{RMS}_{\text{proposed}}^2}{2\sigma^2} = 0 \quad (2.6)$$

and therefore, the limit of  $L_{\text{ratio}}$  is one ( $\lim_{\sigma^2 \rightarrow \infty} L_{\text{ratio}} = 1$ ). Hence, the use of a high variance causes a high acceptance rate

$$\text{acc} = \frac{N_{\text{accepted}}}{N_{\text{iterations}}} \quad (2.7)$$

independent of whether RMS becomes smaller or larger through the proposed DFN. In contrast, the lower the variance is, the lower the mean RMS after the burn-in phase. However, a variance that is too low increases the possibility of the algorithm getting stuck in a local minimum as  $L_{\text{ratio}}$  approaches infinity for a decreasing error and zero for an increasing RMS while using small variance. If a higher variance is chosen, the mean RMS increases as well, but more proposed realizations will be accepted and the mixing of different accepted realizations is better.

### 2.2.3 Estimation of the noise variance

In addition to the reconstruction of the DFN, we can estimate the variance of the measurement error, i.e., the measurement noise. While this value is the main control parameter of the convergence of the rjMCMC algorithm, in most implementations its value is empirically chosen. For pressure measurements, this value is relatively easy to properly choose, but for solute and especially for temperature measurements, it becomes difficult due to numerous environmental factors and the strong

influence of imperfect experimental conditions (e.g., nonuniform physical properties of the borehole, sampling inconsistency, tracer degradation). Hence, we apply the following methodology for variance sampling: The measured data  $\mathbf{d}$  (obtained by  $N_{\text{data}}$  measurement points) is composed of the tracer BTCs or the pressure signals that would be observed without noise  $\tilde{\mathbf{d}}$  and a measurement error  $\epsilon$ . Therefore, the recorded data can be expressed as  $\mathbf{d} = \tilde{\mathbf{d}} + \epsilon$ .  $\epsilon_i$  ( $i = 1, \dots, N_{\text{data}}$ ) is independent and normally distributed,  $\epsilon_i \sim \mathcal{N}(0, \sigma_{\text{noise}}^2)$ . The observation data is also normally distributed  $d_{\text{obs},i} \sim \mathcal{N}(\tilde{d}_i, \sigma_{\text{noise}}^2)$  with data mean  $\tilde{\mathbf{d}}$  and noise variance  $\sigma_{\text{noise}}^2$ .

Our aim is to determine  $\tilde{\mathbf{d}}$  and estimate the variance of the noise. Therefore, we need a probability density function (pdf) for  $\sigma_{\text{noise}}^2$  that depends on the observed data and the model parameters to draw the variance from. The posterior pdf of  $\sigma_{\text{noise}}^2$  can be calculated while using Bayes' theorem with the model parameters  $\theta$  (DFN and inversion parameters) and the observation data  $\mathbf{d}$

$$p(\theta|\mathbf{d}) = \frac{L(\mathbf{d}|\theta)p(\theta)}{p(\mathbf{d})}. \quad (2.8)$$

The denominator is assumed as constant and therefore can be neglected. For reasons of clarity,  $\theta_{-\sigma_{\text{noise}}^2}$  denotes the model parameters without  $\sigma_{\text{noise}}^2$ . Due to Bayes' theorem and a constant  $p(\mathbf{d})$ , the posterior pdf of  $\sigma_{\text{noise}}^2$  can be expressed as

$$p(\sigma_{\text{noise}}^2|\mathbf{d}, \theta_{-\sigma_{\text{noise}}^2}) \propto L(\mathbf{d}|\theta)p(\sigma_{\text{noise}}^2) \quad (2.9)$$

from which  $\sigma_{\text{noise}}^2$  can be sampled (Demirhan and Kalaylioglu, 2015; Gelman et al., 2013).

To determine the likelihood function  $L(\mathbf{d}|\theta)$ , we assume that the tracer BTCs or the pressure signals of the current DFN realization (denoted by  $f(\theta)$ ) calculated with the forward model are the data mean  $\tilde{\mathbf{d}}$ . This assumption is valid after the burn-in phase, because the error between the data mean and the simulated data from the proposed DFN realization is small enough  $\tilde{d}_i - f(\theta)_i \approx 0$ . Therefore, the probability density function of the observation data given the model parameters, i.e., the likelihood function, can be calculated with Eq. 2.4. The estimated variance is higher than the variance of the noise at the beginning of the inversion due to the higher error occurring during the first iterations, i.e., the burn-in phase. The estimated noise variance is inserted into the likelihood function to replace the fixed variance. This is valid because of the assumption  $d_i \sim \mathcal{N}(\tilde{d}_i, \sigma_{\text{noise}}^2)$ , which is expressed by the likelihood function. Thus, the variance in the likelihood function is updated by estimating the noise variance in every iteration of the rjMCMC loop.

The use of a noninformative prior as pdf of  $\sigma_{\text{noise}}^2$  ensures that the data mainly affect the posterior distribution. In this study, an inverse gamma (IG) and a uniform (U) prior are applied

$$p(\sigma_{\text{noise}}^2) \sim \mathcal{IG}(a, b), \quad (2.10)$$

$$p(\sigma_{\text{noise}}^2) \sim \mathcal{U}(0, c), \quad (2.11)$$

with the so-called hyperparameters  $a$ ,  $b$ , and  $c$  ( $a, b, c > 0$ ). A noninformative prior is obtained by using small values for  $a$  and high values for  $b$  and  $c$ . Bayes' theorem leads to the following posterior pdfs that are dependent on the prior

$$p\left(\sigma_{\text{noise}}^2 | \mathbf{d}, \theta_{-\sigma_{\text{noise}}^2}\right) \sim \mathcal{IG}\left(a + \frac{n}{2}, b + \frac{\sum_{i=1}^{N_{\text{data}}} (d_i - f(\theta)_i)^2}{2}\right), \quad (2.12)$$

$$p\left(\sigma_{\text{noise}}^2 | \mathbf{d}, \theta_{-\sigma_{\text{noise}}^2}\right) \sim \mathcal{IG}\left(\frac{n}{2} - 1, \frac{\sum_{i=1}^{N_{\text{data}}} (d_i - f(\theta)_i)^2}{2}\right). \quad (2.13)$$

The calculation of the posterior pdf is illustrated in Eq. 2.12 while using the IG prior and in Eq. 2.13 using the uniform prior. The IG prior has to be carefully handled, since the pdf is improper as  $a$  and  $1/b$  approach zero. A pdf is improper if the integral of the distribution is infinity, which violates the assumption that the cumulative probability distribution approaches one or any positive value for non-normalized distributions. In this case, the improper IG prior leads to improper posterior distribution. The results of the two different priors will be compared in the following because of this potential shortcoming (Demirhan and Kalaylioglu, 2015; Gelman et al., 2013).

After a new DFN realization is accepted or rejected (as explained in Section 2.2.2), the variance is estimated from the posterior pdf while using the Gibbs sampling method illustrated in Fig. 2.3. The acceptance probability  $\alpha$  of a Gibbs sampler is always one. Therefore, every proposed variance will be accepted (Brooks et al., 2011). The variance sampling is implemented in every iteration of the inversion loop after the evaluation of a proposed update of the DFN model parameters (see Fig. 2.2). This is illustrated by adding the sampled variances to a histogram, as shown in step 4 of Fig. 2.3. The described procedure is presented for an increasing number of iterations.

A similar procedure is employed by Fearnhead (2005) and Punskeya et al. (2002) to analyze a speech signal in order to obtain the real speech data without noise. Gallagher et al. (2011) used the rjMCMC method to identify the abrupt changes in geochemical data series due to environmental or climatic variations and to fit a constant regression function to the recorded data curves. The regression function is defined piecewise between two changepoints, which model the abrupt changes in the data series. Adding, deleting, or moving a changepoint estimates the number and position of the changepoints. They estimate the variance of the noise while using an acceptance criterion to accept or reject a new variance proposal. In Sambridge (2016), an rjMCMC algorithm is applied to reconstruct sea level variations assuming that the time series and the measured data contain stochastic noise.

## 2.3 Results

In the following, we first rely on a fixed variance in the likelihood function to compare the results of hydraulic and tracer tomography. In the second part, the results of the estimation of the noise variance are presented.

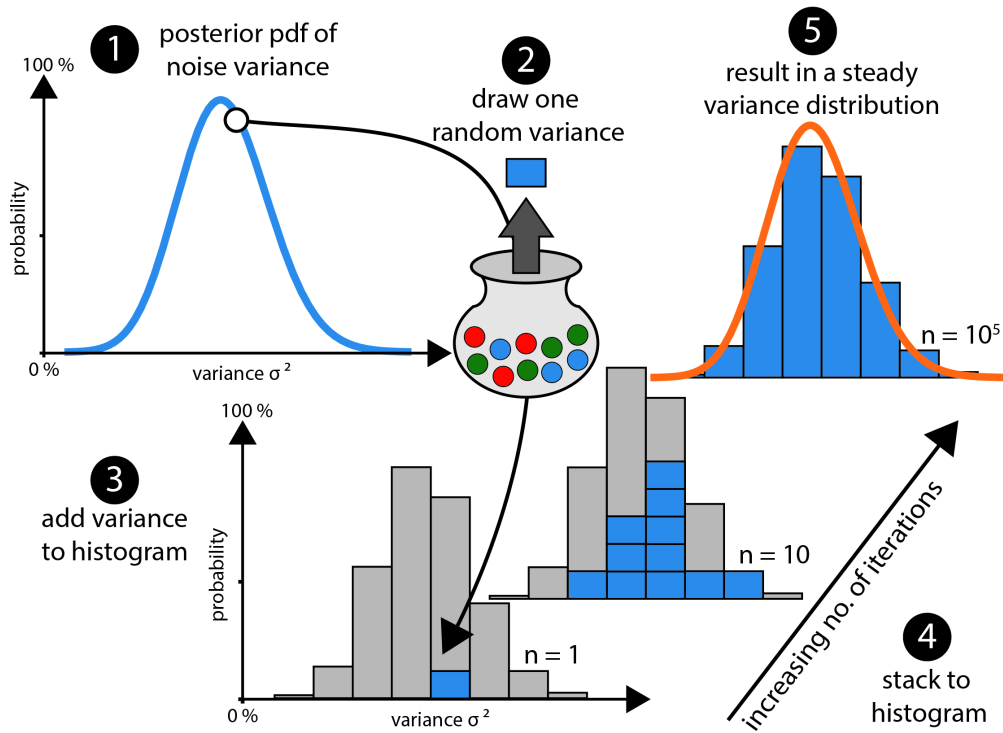


Figure 2.3: Scheme to explain the procedure of drawing samples from a variance probability function (pdf)

### 2.3.1 Results of the DFN inversion

The result of the DFN inversion is not a single calibrated DFN model. In every iteration of the MCMC loop, a DFN realization is calculated and stored. The set of DFN realizations is called the ensemble. This result contains information regarding the probabilistic properties of the inverse problem, such as uncertainty and bi- or multimodality. The probabilistic characteristics stay the same for different inversion runs, as our inversion method is a stochastic method. To visualize the ensemble, we convert it to a fracture probability map (Somogyvári et al., 2017). This is done via the rasterization of the DFN realizations and by taking the mean of these raster models over the ensemble. The fracture probability of one point, i.e., the probability of this position to contain a fracture, is the number of DFN realizations that identify a fracture at this point divided by the whole number of realizations. This representation is equivalent to taking the mean of the ensemble, which is a common method of visualization (see Bodin and Sambridge, 2009; Jiménez et al., 2016).

Figure 2.4 shows the tomographic reconstruction of the hydraulic tomography experiment. The fracture locations are well resolved, and the locations of the fracture intersections with the higher fracture probability roughly match those of the

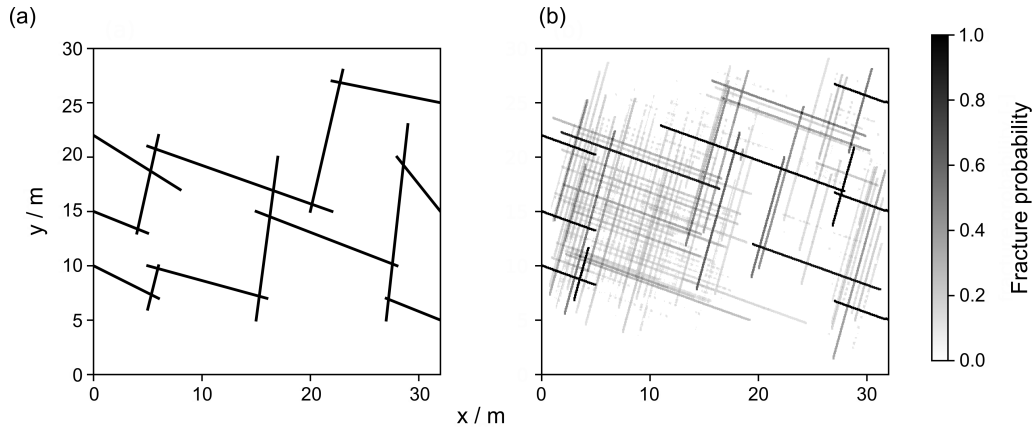


Figure 2.4: (a) Synthetic discrete fracture networks (DFN) and (b) the results using the pressure signals for the inversion illustrated as fracture probability map.

synthetic model. Fractures at the sides of the model (connecting the sources and receivers with the DFN) are fixed, thus they appear with 100% probability. This assumption is acceptable since it is possible to detect the fracture location and orientation in boreholes based on core and image logs (e.g., optical or acoustical televiewer) (see Afshari Moein et al., 2018; Jalali et al., 2018).

The fracture probability map only shows the fractures with a probability higher than 10% to present the results clearly. In Fig. 2.4, the general characteristics of the original DFN can be identified. We can locate the area where the main horizontal connection between the source and receiver takes place. In addition, the non-fractured positions can be detected. Still, some errors are visible in the reconstruction. The quality of the recognition is better there so that the fractures on the right half of the model appear with higher probability because observation points are only placed on the right side of the model. The position of the fractures, which connect the fractures of the left side of the model horizontally with the middle of the investigated area, is uniformly distributed between  $y \approx 8$  m and  $y \approx 22$  m. Therefore, we can conclude that this area contains fractures, but we cannot determine the exact position of a single fracture. In contrast, the position of the fractures, which horizontally connect the middle of the area with the right side of the model, has a higher probability and it is better resolved. The variance of a fracture position is much smaller on the right half of the investigated area. The position of the fracture with its center point at  $x \approx 30$  m and  $y \approx 12$  m can be fit to a normal distribution, since the fractures at the left and right side of it appear symmetrically with a decreasing probability. This corresponds to a Gaussian pdf of the position of this fracture. The aligned dots occur due to the rasterization in the fracture probability, and their size depends on the accuracy of converting a continuous DFN realization to the grid points of the probability raster. They represent fractures with

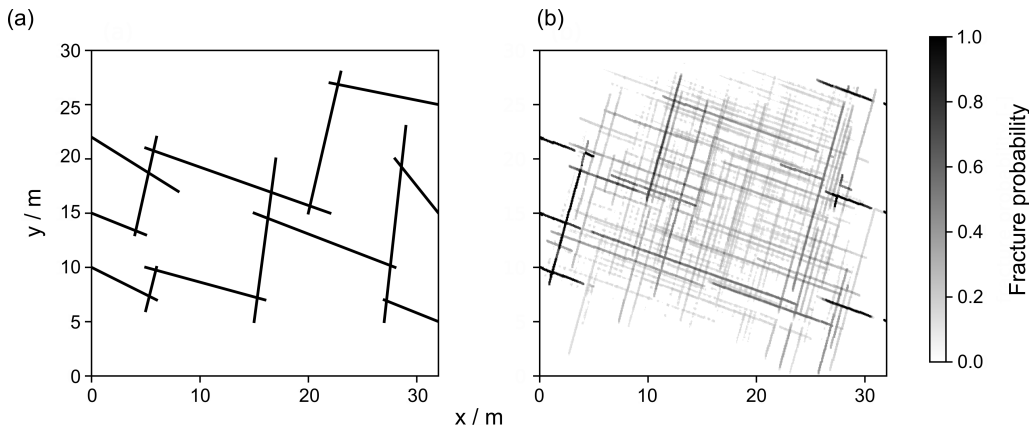


Figure 2.5: (a) Synthetic DFN and (b) the results using the tracer BTCs for the inversion illustrated as fracture probability map.

a very low probability.

Figure 2.5 shows the tomographic reconstruction of the tracer tomography experiment. We check the acceptance rate of the rjMCMC loop after the burn-in phase to ensure that both of the results are comparable, see Eq. 2.7. The acceptance rate in both cases is about  $acc \approx 4.2\%$ . From this, we can conclude that the different results of the different tomographic concepts do not depend on the parameter settings of the inversion, and especially not on the variance in the likelihood function. The most obvious difference to the hydraulic tomography example is the larger variability of the results. In contrast to the results of the hydraulic tomography (Fig. 2.4), single fractures, except for fractures from the injection and receiver points, are less visible, since no fractures occur with a high probability. Additionally, neither the left nor the right side is resolved well with a high probability. Still, from the result in Fig. 2.5, we get an idea regarding the fractured and non-fractured areas and the main characteristics of the DFN. The gaps appearing between some of the pixels are a matter of rasterization similar to the aligned dots and they do not occur in the individual DFN realizations. This results from a raster grid that does not accord well with the DFN geometry.

### 2.3.2 Results estimating the noise variance

In contrast to the previous section, we assume that the observed tracer breakthroughs and pressure signals contain stochastic noise. Therefore, we want not only to do the inversion of the DFN, but to also estimate the noise variance and the data mean, i.e., the theoretically measured data without noise. This is accomplished according to Section 2.2.3. A synthetic example for noisy tracer breakthroughs with  $\sigma_{\text{noise}} = 3 \text{ mg l}^{-1}$  is shown in Fig. 2.6. The data mean is iteratively estimated by the inversion of the DFN by applying the forward model to calculate the tracer breakthroughs of the current DFN realization. The variance is sampled from the IG

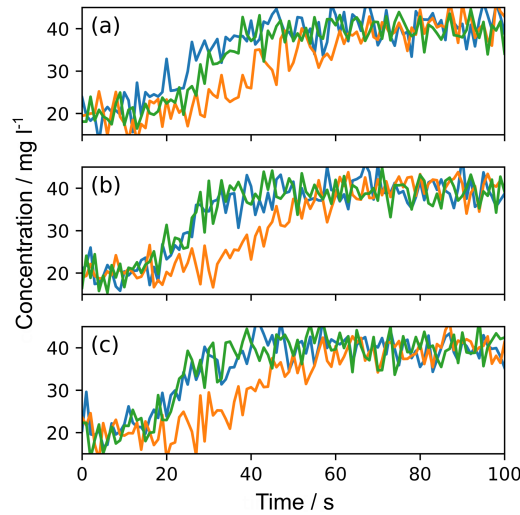


Figure 2.6: Noisy tracer BTCs ( $\sigma_{\text{noise}} = 3 \text{ mg l}^{-1}$ ) for different combinations of source and receiver points: (a) tracer injection at source 1; (b) tracer injection at source 2; (c) tracer injection at source 3. The colors of the graphs accord with the colors of the receiver points in Fig. 2.1.

posterior pdf in every iteration of the inversion loop. These samples are illustrated in a histogram that compares this with the posterior pdf of  $\sigma_{\text{noise}}^2 p(\sigma_{\text{noise}}^2 | \mathbf{d}, \theta_{-\sigma_{\text{noise}}^2})$  of the last iteration of the rjMCMC loop in Fig. 2.7. The pdf and the histogram in Fig. 2.7 are as well not normalized, i.e., a cumulative probability function would approach any positive value for an increasing variance due to the non-normalized posterior pdf (see Eq. 2.9) from which the variance is sampled. The samples converge to a stationary distribution, since the histogram of the variance samples fulfills the posterior pdf of the last step. Both variance histograms are similar, as we compare the two different priors. Hence, we can conclude that both priors are in fact noninformative, because the posterior pdf is mainly affected by the data and not by the choice of the prior pdf. In addition, the prior IG pdf does not lead to an improper subsequent pdf in this case.

The same procedure could be applied to the noisy pressure signals (Fig. 2.8). The histogram of the variance samples and the posterior pdf of  $\sigma_{\text{noise}}^2$  are shown in Fig. 2.9. Additionally, in this case, both of the priors provide similar histograms and posterior pdfs of  $\sigma_{\text{noise}}^2$ .

## 2.4 Discussion and conclusions

The presented study deals with an exemplary hypothetical case, which makes it difficult to generalize the results to other experimental setups or general conclusions. Still, the application of the two tomographic concepts allows for the comparison of

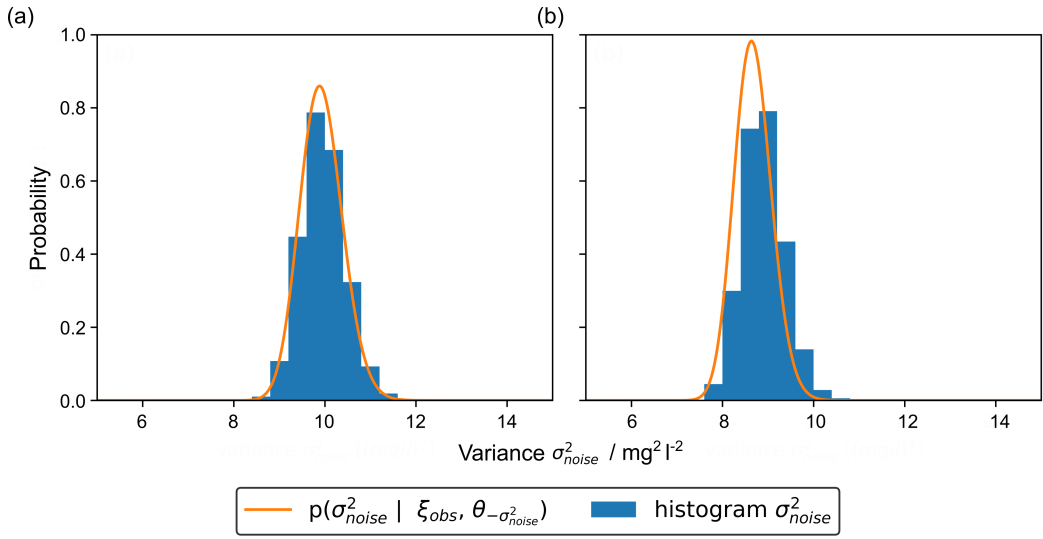


Figure 2.7: Histogram of variance samples during the inversion and posterior pdf of  $\sigma_{\text{noise}}^2 p(\sigma_{\text{noise}}^2 | \mathbf{d}, \theta_{-\sigma_{\text{noise}}^2})$  in the last iteration of the rjMCMC loop (a) inversion of  $\sigma_{\text{noise}}^2$  using the inverse gamma prior; and, (b) inversion of  $\sigma_{\text{noise}}^2$  using the uniform prior.

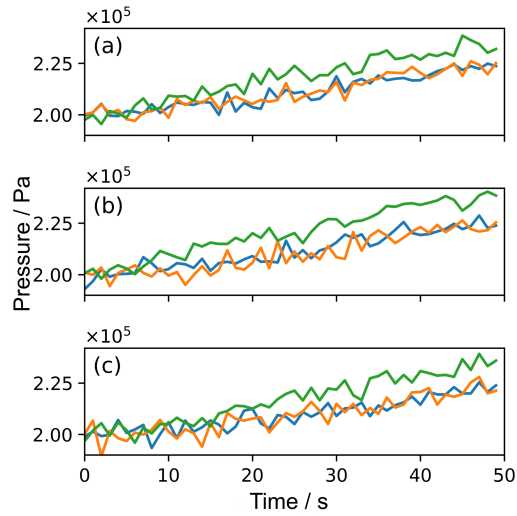


Figure 2.8: Noisy pressure signals ( $\sigma_{\text{noise}} = 3000$  Pa) for different combinations of source and receiver points: (a) water injection at source 1; (b) water injection at source 2; (c) tracer injection at source 3. The colors of the graphs accord with the colors of the receiver points in Fig. 2.1.



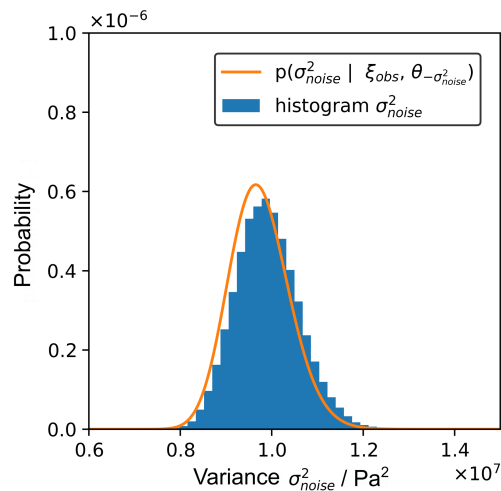


Figure 2.9: Histogram of variance samples and posterior pdf of  $\sigma_{\text{noise}}^2$  in the last step of the inversion.

characteristic differences. Hydraulic tomography provides better results than tracer tomography, since the variability of the result is smaller and some fractures occur with a higher probability, i.e., the obtained fracture probability map of the hydraulic tomography is better resolved. In this case, the pressure signals are better for the inversion, because the complexity of the simulation is smaller. For practical use, many extra factors would probably make the tracer tomography better, e.g., the measurement noise is smaller, and tracer BTCs can be more easily detected. Both tomographic concepts are able to perfectly identify no fractured areas and the main characteristics. The experiment should be repeated in the other direction, since the part of the cross-sectional area where the receiver points are located provides better results to further improve our inversion algorithm. This uneven sensitivity is a known attribute of tomographic methods, as it was shown for continuous reconstruction in Somogyvári et al. (2016).

The presented procedure for the estimation of variance includes noise variance and model errors. The estimated variance is usually higher than the variance of the noise, since the estimated variance includes not only the variance of the noise, but also the error of the conceptual model, e.g., the geometrical constraints (only two different fracture inclinations, fracture length distribution), the limited number of iterations, and errors of the forward model. Therefore, this method could also be applied to determine the errors of the conceptual model, if observation data without noise or with very low noise variances are used for the inversion.

Variance estimation becomes even more significant when considering, for instance, heat as a tracer. In-situ temperature observations are more prone to systematic errors and to being affected by diffusion than solutes. The simulation of thermal

transport in both fracture and matrix introduces an extra level of complexity into the forward model, and requires the specification of additional physical parameters. Variance estimation could be employed to reveal initial improper settings if these parameters are set incorrectly.

The aim of this study is to extend the inversion procedure from synthetic DFN cases to practical applications with field data. To prepare this, we conclude from the synthetic DFN case study to the parameters and information we need to use this inversion algorithm in practice. In addition, we checked the limitations and the conceptual errors of this approach. However, we introduce a method to deal with that issue. One conclusion is that we need a 3D forward model to expand from the two-dimensional cases to three-dimensional DFN reconstruction. Moreover, we require information regarding the fracture sets, e.g., from outcrops. We also have to use an optical or acoustical televiewer to get the inclination and the position of the fractures adjacent to the boreholes to introduce them as source and receivers for the inversion and as boundary conditions in the forward model.

# 3 Stochastic inversion of three-dimensional discrete fracture network structure with hydraulic tomography

## Abstract

We introduce an approach for the stochastic characterization of the geometric and hydraulic parameters of a three-dimensional (3D) discrete fracture network (DFN) and for estimating their uncertainty based on data from hydraulic tomography experiments. The inversion approach relies on a Bayesian framework and the resulting posterior distribution is characterized by generating samples by Markov chain Monte Carlo (MCMC) methods. The inversion method is evaluated for four synthetic test cases related to the Grimsel Test Site (GTS) in Switzerland. Comparison of original and reconstructed DFN models shows that the presented approach is suitable for identifying variable fracture locations and orientations. This is especially the case for those fractures that represent the preferential flow paths in the simulated experiments. It is also revealed that the Bayesian framework is useful to discriminate fractures based on the reliability of the inversion, which is illustrated by fracture probability maps taken as sections through the studied rock mass. Moreover, it is demonstrated that the hydraulic apertures can be calibrated together with the fracture geometries. A premise for applicability in practice, however, is that the hydraulic measurements are complemented by additional information to sufficiently constrain the value ranges of the geometric and hydraulic parameters to be inverted together. The presented work expands the applicability of a previously presented promising two-dimensional procedure based on transdimensional inversion to field-based 3D problems. The theoretical findings here open the door for highly flexible structural characterization in practice based on hydraulic tomography, as well as alternative or complementary tomographic methods.

## 3.1 Introduction

Groundwater flow through rocks with a low-permeability matrix is usually dominated by the presence of fractures, associated with pronounced local permeability contrasts. Multiple connected fractures yield preferential flow paths along a fracture network permeating the rock mass. Implemented in a model, the network is mostly

represented either by a single or multiple continuum method that translates the hydraulic properties of the fractures into an upscaled effective permeability tensor or explicitly as a discrete fracture network (DFN). Combinations of both methods are also possible, such as realized by the discrete fracture matrix model (Berre et al., 2019). Dense fracture networks with many interconnections are more appropriate for the representation in a continuum model. In contrast, if a few fractures dominate the hydraulic conditions, resolving the fractures explicitly in flow models allows for a more detailed insight into preferential flow and transport paths, specific processes such as flow focusing, spatial fracture connectivity, and quantification of the individual influence of single fracture parameters (Berkowitz, 2002; de Dreuzy et al., 2012; Hyman et al., 2019; Neuman, 2005; Roubinet et al., 2010; Yin and Chen, 2020). Both variants are compared, for example, by Hadgu et al. (2017), in terms of effective permeability and tracer breakthrough curves by simulating flow and tracer transport in benchmark test cases. The authors conclude that because of the explicit representation of the DFN, this approach is better suited to represent the structural heterogeneity of the DFN, insofar as the parameters of the network are well mapped. Proper mapping, however, is challenging due to the limited insight into the studied rock mass.

Spatial reconstruction of fracture systems requires field investigation techniques that deliver meaningful space-dependent information such as obtained by tomography. The underlying principle of tomographic methods is the application and combined interpretation of signals sent from different sources and/or recorded at different nearby receivers. Hydraulic tomography, for instance, is commonly based on multilevel pumping or slug tests with pressure signals recorded in cross-borehole test configurations (Berg and Illman, 2011; Brauchler et al., 2003, 2013b; Cardiff and Barrash, 2011; Cardiff et al., 2013, 2019; Hu et al., 2011; Illman et al., 2009; Illman, 2013; Klepikova et al., 2020; Laloy et al., 2018; Poduri et al., 2021; Sánchez-León et al., 2020a,b; Sharmeen et al., 2012; Tiedeman and Barrash, 2020; Wang et al., 2017; Yeh and Liu, 2000; Zha et al., 2015; Zhao and Illman, 2017; Zhao et al., 2019). This facilitates spatial resolution of aquifer heterogeneity by inversion procedures and further use of reconstructed permeability patterns in flow models. Fractured systems have been addressed by hydraulic tomography as well as by other tomographic techniques, such as tracer tomography (Brauchler et al., 2013a; Kittilä et al., 2020; Klepikova et al., 2014), stress-based tomography (Afshari Moein et al., 2018), or coupled inversion of geophysical signals (Chen et al., 2006; Day-Lewis et al., 2003; Dorn et al., 2013). The interpretation of the measured data is performed by a continuous representation of the porous or fractured media in most of these previous studies.

An explicit representation of the fractured media as DFN was demonstrated mainly for two-dimensional (2D) problems that neglect the role of structural variations in the third dimension (Fischer et al., 2020; Ma et al., 2020; Somogyvári et al., 2017; Tran and Tran, 2007). Three-dimensional (3D) inversion problems applying data from tomographic experiments are more challenging and have been handled primarily by continuous inversion methods. These provide tomograms of continu-

ous hydraulic conductivity distributions (Cardiff and Barrash, 2011; Cardiff et al., 2013, 2019; Tiedeman and Barrash, 2020) and hydraulic conductivity together with storativity distributions (Berg and Illman, 2011; Illman et al., 2009; Sánchez-León et al., 2020b; Zha et al., 2015; Zhao and Illman, 2017; Zhao et al., 2019). Promising alternatives rely on the simplification of the inversion problem by prescribing selected characteristics of the main flow paths between two boreholes (Klepikova et al., 2020); they focus on critical hydraulic aspects such as the role of a leakage interface (Wu et al., 2020) or the aperture distribution (Wu et al., 2021). In this context, multifidelity approaches can strike a balance between the accurate representation of 3D DFNs and simplifications of the inversion problem to improve the computational efficiency of modeling the tomography experiment (O'Malley et al., 2018).

In our study, we present a full 3D tomographic fracture network inversion. Based on promising previous work in 2D (Ringel et al., 2019; Somogyvári et al., 2017), the geometrical properties of fractured aquifers are represented by a flexible 3D DFN structure that is iteratively calibrated to the data from tomographic measurements. Related studies on the direct inversion of 3D fracture networks generate DFNs and condition them to geophysical and hydrogeological data (Dorn et al., 2013) or fit a random number of fractures intersecting the boreholes (Mardia et al., 2007). Our objective is to develop an inversion technique that adjusts the structure and organization of fractures as flexibly as possible. Moreover, a stochastic characterization of the structural properties is also chosen to account for the uncertainty in the results, as field data is often insufficient for unequivocal model inversion.

In the following, the forward and inverse modeling procedures used for simulation of DFNs will first be described. We refer to a synthetic hydraulic tomography experiment, which is treated as virtual reality to inspect and demonstrate the capabilities of the developed inversion method. This analysis is based on four different experimental variants to test inversion performance and limitations.

## 3.2 Methodology

The overall principle of the presented procedure is using tomographic information to infer as much 3D structural characteristics as possible of a fractured rock mass on the decimeter scale. In this study, a hydraulic tomography setup is chosen that is based on multilevel hydraulic pumping tests in boreholes with different orientations. The recorded pressure responses from multiple tests in these boreholes reveal the existence and degree of hydraulic connections within the fracture network of the rock mass. By simultaneous fitting of a DFN model to all recorded pressure responses, preferential flow paths and thus, hydraulically active fractures can be localized. While there exist different methods to calibrate the DFN to such hydraulic signals or tracer and geophysical information, they are commonly based on limiting assumptions (e.g., a priori fixed fracture locations). Our purpose is to minimize such assumptions except for a conceptual model of given fracture sets, which is formulated

based on the properties of fractures along boreholes or outcrops. This means, for a given fracture set, realistic ranges of fracture geometric and hydraulic parameters are predefined. Within this framework, fracture numbers, their locations, lengths, and hydraulic properties are treated as unknowns and are calibrated.

Flexible 3D adjustment of fracture geometries is ideally accomplished by an iterative learning procedure, which calibrates the model to independent measurements. Considering conditions in practice, we assume that there exists a basic geological insight in typical fracture orientations, density, and a range of possible hydraulic aperture values. Exact structures, however, are unknown, and the prior geological knowledge is exploited together with hydraulic test data to infer potentially valid DFN configurations. Typically, outcrops or properties of fractures along boreholes are investigated to define a conceptual model and for the setup of the inversion problem. A proper framework for probabilistic processing of such soft and hard data follows Bayesian principles, which is considered here. Bayesian inversion is accompanied by a high computational demand for iterative comparison of model predictions with measurements, which may require many thousands of model runs. To minimize the simulation time for the forward model, an unsophisticated DFN fluid flow model has been set up to simulate hydraulic tests in fractured aquifers with variable fracture orientations. This is described in the next chapter as the forward model concept of this study. After this, the inversion algorithm and its implementation with test cases are described. Different test cases are used to examine the applicability of the tomographic inversion. Here, specifics of the examined hydraulic problem, the parameters treated as unknowns, as well as the prior information will be explained.

### 3.2.1 Forward modeling of hydraulic tomography experiment

Fractures are modeled as lower-dimensional objects with a uniform aperture, assuming a constant pressure gradient normal to the fracture plane due to the small aperture. Fluid flow in a single fracture is described by the continuity equation and the cubic law derived by simplifying the Navier-Stokes equations (Berre et al., 2019; Zimmerman and Bodvarsson, 1996)

$$a\rho S \frac{\partial p}{\partial t} - \nabla_T \cdot \left( a\rho \frac{k_f}{\mu} \nabla_T p \right) = aq \quad (3.1)$$

with the hydraulic aperture  $a$  [m], the density of the fluid  $\rho$  [ $\text{kg m}^{-3}$ ], the specific storage  $S$  [ $\text{Pa}^{-1}$ ], the fracture permeability  $k_f$  [ $\text{m}^2$ ], the fluid dynamic viscosity  $\mu$  [ $\text{Pa s}$ ], and a source/sink term  $q$  [ $\text{kg m}^{-3} \text{s}^{-1}$ ]. The pressure  $p$  [Pa] refers to the static pressure and the piezometric pressure due to gravitational forces. The gradient  $\nabla_T$  is performed in the local coordinate system tangential to the fracture plane.

In this study, the equations are solved by the finite element method (FEM) with a conforming discretization at the intersections of different fractures. For further reading on the FEM fundamentals, we refer to related literature, for example, Langtangen and Mardal (2019), Reddy and Gartling (2010), and Zienkiewicz et al. (2014).

For conciseness, only the methodology that is specific to the present study and the evaluation of the results are explained in the remainder.

The geometry and mesh generation is implemented by the open-source mesh generator *Gmsh* (Geuzaine and Remacle, 2009). Each fracture can be created separately according to its properties, with the built-in geometry module as ellipse arbitrarily positioned in the investigated volume. The intersections of different fractures are considered by the so-called Boolean fragment operation implemented in *Gmsh*. This function provides a conforming discretization at the interfaces of fractures. The fractures are implemented as shell elements, as suggested by Reddy and Gartling (2010), for heat transfer problems with a constant temperature across the element thickness. This allows the reduction of a 3D fracture to a 2D plane without losing information about the properties normal to the fracture plane.

To verify our implementation, 2D and 3D scenarios have been defined in a preliminary analysis. For each scenario, there are analytical solutions or estimates of the expected results available. The 2D problems apply to the general behavior of the implementation of the FEM simulation concept. Therefore, the scenarios are specified by the method of manufactured solutions and the convergence of the numerical solution to the defined solution is evaluated for different basis functions and mesh resolutions (Langtangen and Mardal, 2019). This demonstrates the correct calculation of the pressure diffusion within a single fracture midplane and the accurate implementation of the boundary conditions. The 3D scenarios are designed to check those characteristics of flow in a DFN that are essential to providing physically meaningful results. That is, the reduction of the dimension by the shell elements, the quality of the results depending on the basis functions and the mesh resolution, and the balance of fluxes at the intersections of fractures for different apertures and fracture lengths. To consider more complex physics, the forward model may be replaced by any other DFN simulation tool that allows for automatic updating of the DFN structure (Hyman et al., 2015; Keilegavlen et al., 2020).

### 3.2.2 Inversion methodology

The method for the inversion of the DFN structure, that is, the estimation of the model parameters given the observed hydraulic data, is based on the Bayesian approach

$$p(\theta|\mathbf{d}) \propto L(\mathbf{d}|\theta)p(\theta) \quad (3.2)$$

that evaluates the posterior probability  $p(\theta|\mathbf{d})$  of the parameters of the DFN model given the results from the tomography experiment. In this study, the parameters  $\theta$  to be inferred are the properties of the DFN. The parameters are treated as random variables that are characterized by probability density functions. The data  $\mathbf{d}$  stems from the hydraulic tomography experiment, that is, the pressure perturbations provoked by an overpressure created at the injection points. The posterior distribution is based on prior information  $p(\theta)$  about the position and the properties of the fractures and the likelihood of the data  $L(\mathbf{d}|\theta)$  (Gelman et al., 2013).

The likelihood function evaluates the error between the measured data and the simulated results from the corresponding hydraulic tomography experiment. In the subsequent application to different test cases, we assume independent and identical normally distributed errors for the time steps of each pressure signal. Therefore, the log-likelihood function is proportional to the sum of the squared error over all data points  $N_{\text{data}}$

$$\log L(\mathbf{d}|\theta) \propto -\frac{1}{2\sigma^2} \sum_{i=1}^{N_{\text{data}}} (d_i - f(\theta)_i)^2 \quad (3.3)$$

whereby  $f(\theta)$  refers to the simulation of the forward model for a given DFN parameter set  $\theta$ .

Evaluating the posterior distribution is a challenge due to its complexity and its typically high dimensionality. A widely used method to handle this problem is to characterize the posterior by drawing samples from the posterior distribution according to the Markov chain Monte Carlo (MCMC) sampling strategy. Starting from an initial state, new samples  $\theta'$  are proposed in each iteration  $i$  according to a proposal distribution  $q$  and are accepted ( $\theta_i = \theta'$ ) with probability

$$\alpha = \min \left( 1, \frac{p(\theta'|\mathbf{d})}{p(\theta_{i-1}|\mathbf{d})} \frac{q(\theta_{i-1}|\theta')}{q(\theta'|\theta_{i-1})} |J| \right) \quad (3.4)$$

or rejected ( $\theta_i = \theta_{i-1}$ ). The determinant of the Jacobian matrix  $|J|$  holds for a generalization of the update probability. It equals one for updates that do not change the number of parameters. For transdimensional update types that include adding or deleting parameters, the Jacobian provides a relation between the already existing and to be added or deleted parameters. The tolerance for accepting a DFN realization depends on the update probability (Eq. 3.4). A high update probability implies, in most cases, that the proposed realization ( $\theta'$ ) has an equal or greater posterior compared to the current DFN realization ( $\theta_{i-1}$ ), that is, the error between the simulated and measured data is the same or smaller and that it meets the prior distribution. Proposed realizations outside of the prior limits are rejected outright.

The reversible jump MCMC (Fan and Sisson, 2011; Green, 1995; Hastie and Green, 2012) is applied due to the advantage that the number of parameters, in this case, the number of fractures, does not need to be known a priori. Instead, the number of fractures and the structure of the DFN are adjusted iteratively during the inversion. This is accomplished by switching between two update types (Fan and Sisson, 2011). The number of parameters is inferred by so-called between-model moves. In this case, the number of parameters is varied by inserting a fracture in a random position within the investigated volume or by deleting a randomly chosen fracture. Since the insertion of a fracture, in our implementation, is just an addition of parameters that are not linked to the parameters of the other fractures, the Jacobian is equal to 1 (Sambridge et al., 2006). The Jacobian of the reverse update type, that is, the deletion of a fracture, is the inverse of the reverse update, and therefore, it is also equal to 1. The parameters of the DFN for a given number of fractures are adjusted by updating the position, the fracture length, or the fracture aperture.



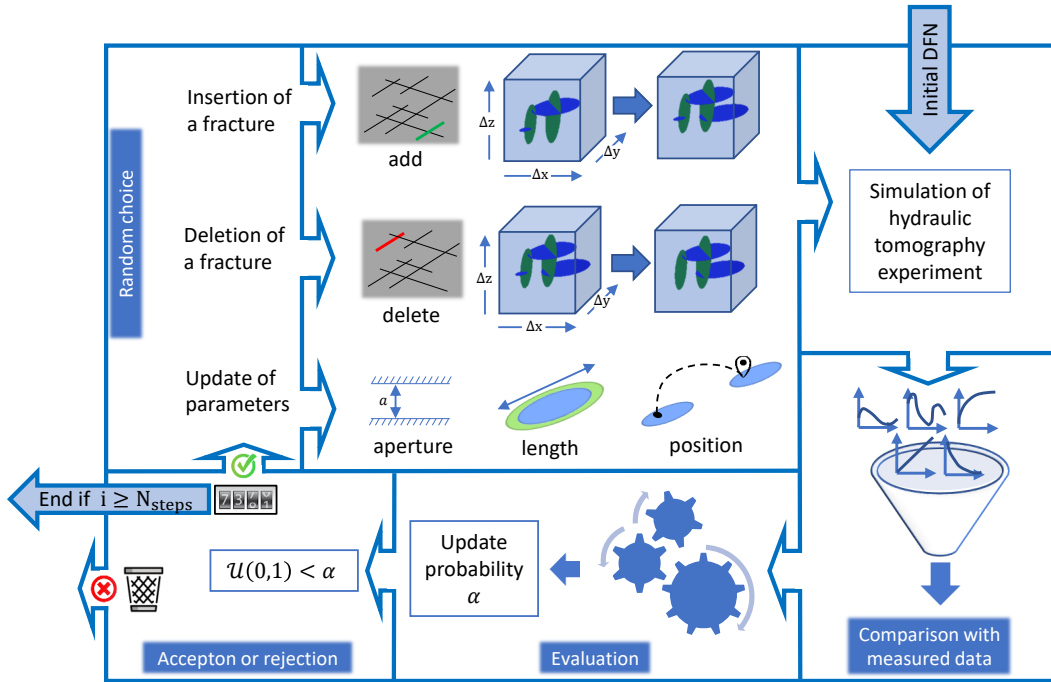


Figure 3.1: Overview of the implemented rjMCMC sampling strategy for the discrete fracture network (DFN) inversion with the between-model moves (insertion or deletion of fractures) and the within-model move, that is, the update of the DFN parameters.

Since the number of parameters does not change, this is described as a within-model move. The parameters are varied by perturbing the current value with a sample from a normal distribution with zero mean and a given variance, which is the most common proposal distribution. In practice, this procedure is implemented by alternating between both update types. The MCMC iterations are initialized by a random DFN realization based on the prior information and the DFNs are adapted iteratively to meet the posterior distribution. An overview of the rjMCMC algorithm and the workflow, as it is implemented for the DFN inversion, is illustrated in Fig. 3.1. The update type is chosen randomly and, in our implementation, for simplicity reasons, no update types are combined. During the burn-in iterations, we found that the efficiency of the algorithm can be improved by raising the probability for those update types that change the number of fractures, that is, insertion or deletion. When the number of fractures reaches the maximum possible number of fractures, the probability for insertion is set to zero.

As further advancement of our previous studies (Ringel et al., 2019; Somogyvári et al., 2017), the insertion of fractures is possible at any position in the investigated volume, that is, fractures do not necessarily have to be connected to the main DFN. In comparison, this provides two main computational advantages. The influence of

Table 3.1: Overview of the characteristics of each test case.

Test case	Settings	Objective
1	Based on measurements at the GTS	Applicability of the inversion method to realistic geological formations
2	Update of the hydraulic aperture by the inversion algorithm	Applicability of the inversion method to identify fracture geometries and hydraulic apertures
3	Insertion of an additional injection point	Sensitivity of the results to the number of constraints
4	Definition of a third fracture set	Applicability of the inversion method to an extra fracture set and handling of more possible flow paths

the initial DFN configuration is lower, and this ensures that more possible DFN realizations are included. Moreover, a fracture without a connection to the main DFN has no hydraulic effect and thus does not change the outcome of the hydraulic tomography simulation. Therefore, considering only the likelihood of this update, the insertion will most probably be accepted. Nevertheless, this realization is part of the posterior and has to be considered to ensure reversibility and stationarity of the Markov chain. Deletion of the same fracture will most likely be accepted for similar reasons, insofar as no new connection to the main DFN has yet been formed. In practice, fractures are inserted randomly within a given domain  $\Delta x$ ,  $\Delta y$ ,  $\Delta z$  (Fig. 3.1). Aside from that, the update of the fracture length and the hydraulic aperture has been included in the inversion framework to improve the sampling efficiency, since this also allows the consideration of more possible DFN realizations.

### 3.2.3 Setup of test cases

To check the applicability of the proposed methods, we employ four synthetic test cases (Table 3.1). The use of synthetic, perfectly known conditions, allows for evaluation of the performance of the inversion procedure, to detect difficulties that could cause errors in the inversion results, and to derive conclusions for measurement data requirements and field applications that are suitable for our inversion approach. In each test case, hydraulic tomography experiments are simulated by creating a constant overpressure sequentially at different cross-well injection positions. The induced transient pressure perturbations at the injection points are recorded at receiver points in adjacent observation boreholes and normally distributed noise is added to the data to account for measurement, modeling, and conceptual errors. The noise is applied to affect the pressure signals, nevertheless, without concealing the main trend of the signals (Klepikova et al., 2020). The standard deviation of the noise is approximately 3% of the mean pressure.

To refer to a realistic geological formation, a base case (test case 1) is devel-

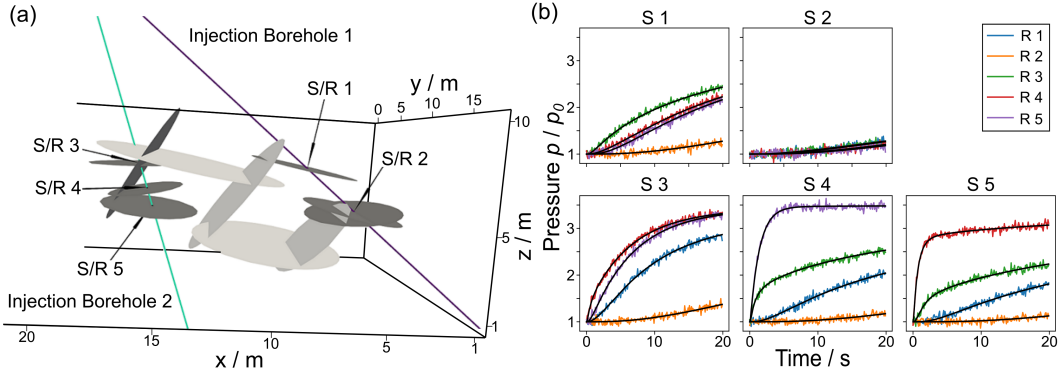


Figure 3.2: (a) Synthetic test case 1 (base case), boreholes, and source/receiver points denoted as S/R 1 to S/R 5. Fractures whose properties are assumed to be unknown are illustrated in lighter gray. (b) Pressure signals recorded at the different receiver points (R 1 to 5) provoked by an overpressure created at the source points (S 1 to 5). The pressure signals result from the forward simulation of the hydraulic tomography experiment with normally distributed noise added and function as basis for the inversion of the discrete fracture network (DFN) properties. The black curves indicate the mean of the simulated pressure signals of the posterior DFN realizations.

oped utilizing data from hydraulic characterization campaigns during the In situ Stimulation and Circulation (ISC) experiments at the Grimsel Test Site (GTS) in Switzerland (Amann et al., 2018; Doetsch et al., 2018; Krietsch et al., 2018). Nevertheless, the present analysis is only theoretical and the fractures of the base case are considered to be perfectly known. The insight from the GTS helps to define reasonable assumptions for the setup of the conceptual models and the prior parameter distributions. The fractures forming the DFN of the base case, as well as the boreholes for simulating a cross-hole hydraulic tomography experiment are presented in Fig. 3.2. The injection boreholes and the properties of the fractures with the center connected to the boreholes are oriented at observations from optical televiewer tests conducted during the ISC experiment (Doetsch et al., 2018; Krietsch et al., 2018). The position of the fractures connecting the boreholes and the length of all fractures are based on the connectivity matrix given in Jalali et al. (2018). The DFN is built up by two fracture sets. The inclination and dip assigned to the fractures are the mean of the fracture sets defined according to the fractures intersecting the boreholes. This tomographic setup yields 5 source/receiver (S/R) points, which means that the constant pressure injection tests are simulated sequentially at each position in the well and the arrival of the pressure signals are recorded at the other source/receiver points functioning as observation locations. The data assumed to be measured during the hydraulic tomography experiment is shown in Fig. 3.2b.

The potential of adjusting the hydraulic aperture within a given range is inves-

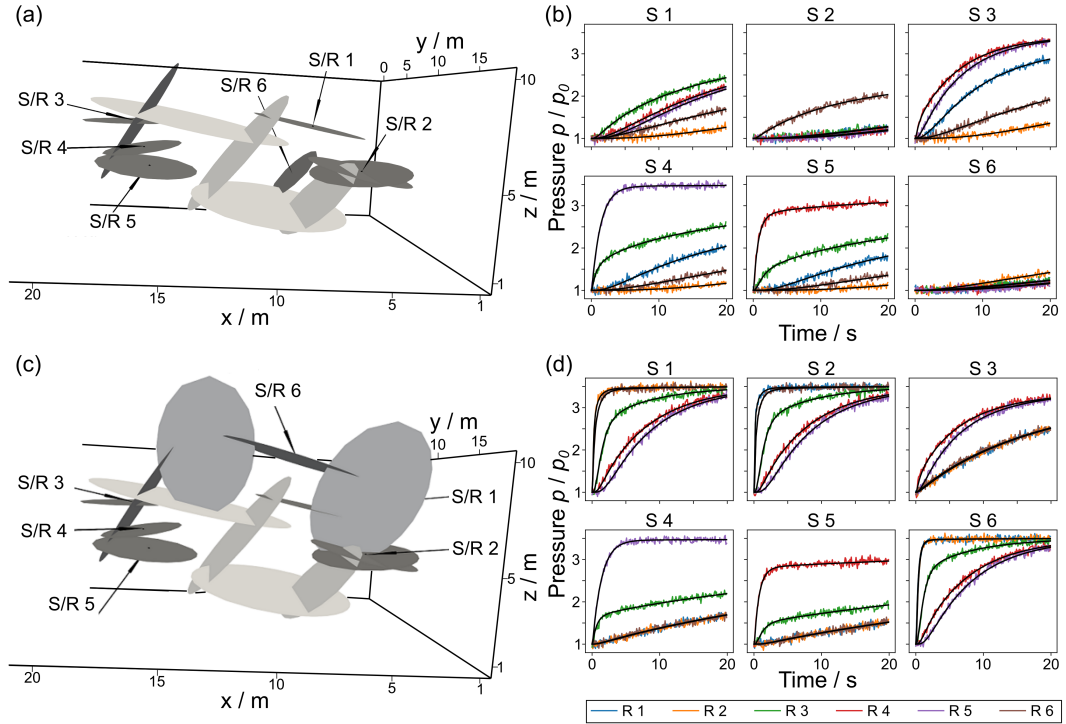


Figure 3.3: (a) Test case 3 oriented at the base case with an extra injection point fracture and an additional source/receiver point (S/R 6). (c) Test case 4 including a third fracture set and an additional source/receiver point (S/R 6). Fractures whose properties are assumed to be unknown are illustrated in lighter gray. The noisy pressure signals and the mean of the simulated pressure curves of the posterior DFN realizations are displayed for both test cases in (b) and (d).

tingated by test case 2. For comparison of the results with the base case, we apply the same DFN setup and the same tomographic test configuration (Fig. 3.2). In contrast to the previous test case, the aperture of the fractures is assumed unknown within given value ranges. Therefore, the aperture values are estimated as part of the parameter update of the inversion algorithm (Fig. 3.1). In this exemplary test case, the range of possible hydraulic aperture values is set to  $\pm 80\%$  of the given value in test case 1, which is implemented as prior bounds.

To examine the capabilities of the inversion methodology further, the base case (1) is extended. The third test case (3) is designed to check the sensitivity of the inversion algorithms to modifications of the DFN and to the number of available pressure signals. Therefore, a new fracture is added with a connection to a borehole to provide another source/receiver point (S/R 6). The additional fracture is placed in the lower part of the investigated volume and shifted backward. Since this fracture is presumably connected to a borehole, its position and the associated fracture set

are given. Hence, this variation of the test case contributes information about the lower part of the DFN in the studied rock mass and the parameters normal to the plane defined by the injection boreholes. This test case is illustrated in Fig. 3.3a. The tomographic setup is the same as before but with an additional source/receiver point (Fig. 3.3b).

Test case 4 (Fig. 3.3c) examines the ability of the inversion method to deal with a (theoretical) third fracture set. The third fracture set is defined by a rotation angle around the x-axis. To infer the properties of this DFN, an additional source/receiver point (S/R 6) is favorable to compensate for the uncertainty due to the additional possible rotation around the x-axis. Therefore, in this case, the tomographic setup is the same as for the previous test cases. By inserting the additional fractures, a unique feature of this third case is that more possible flow paths exist connecting the source/receiver points. Therefore, the rationale of the case is to reveal how the inversion procedure can deal with a potentially higher number of suitable solutions.

### 3.2.4 Implementation of the inversion

Constraints, assumptions, and prior distributions for the formulation and implementation of the inversion problem are mainly based on the information about the fractures connected to the boreholes. An overview of the underlying assumptions, the necessary information for the derivation of a conceptual model, the properties of the prior and likelihood distribution are summarized in Table 3.2.

Table 3.2 follows the steps for the setup of an inversion problem. The basic information, essentially, borehole data or outcrops, is applied for the derivation of a conceptual model and the definition of the prior distribution. The measured data from the hydraulic tests are included as likelihood function. Relying on these sources and assumptions, several parameters of the DFN can be estimated by the inversion algorithm.

The parameters selected for the test cases of this study are listed in Table 3.3. Hydraulic apertures are assigned as fixed values based on the fracture sets for test cases 1, 3, and 4, while the aperture is estimated within the exemplary prior bounds in test case 2. The shapes of the fractures are approximated as plane ellipses with a uniform aperture. Most of the flow occurs directly between intersections with other fractures. Therefore, no sharp edges have to be considered for the simulation of flow. This makes the ellipses a reasonable assumption, but does not account for the potential existence of nonuniform apertures or channelized flow along fractures. The length of the fracture refers to the major axis and the ratio to the minor axis is given by the conceptual model. In this setup of the inversion, the hydraulic conditions in the boreholes are not resolved. Instead, we assume that the injection points can be isolated perfectly by the packer systems.

Table 3.2: Steps required for the setup of the inversion problem, and parameters estimated by the inversion.

	<b>Properties</b>	<b>Information source/ assumptions</b>
1. Basic information	Coordinates of fractures intercepting boreholes	Cores, geophysical logs (e.g., optical or acoustic televiewer)
	Angles of fractures intercepting boreholes	Cores, geophysical logs (e.g., optical or acoustic televiewer)
2. Conceptual model	Fracture shape	Plane ellipse with a uniform aperture; length of minor axis is half of length of major axis
	Fracture sets	Properties of fractures along boreholes (cores, geophysical image logs) or based on outcrops
	Specific storage	Cross-hole in situ tests, laboratory tests
	Hydraulic aperture	In situ hydraulic tests or estimated by inversion
3. Prior distribution	Minimum and maximum possible values for the parameters of the fractures	Field investigation and/or outcrops
	Upper limit for the number of fractures	Fracture intensity map derived from outcrop, cores, and geophysical logs
4. Likelihood function	Transient pressure signals provoked by perturbations of the system	Cross-hole in situ hydraulic tests
5. Estimated parameters	Number of fractures, coordinates, and length of fractures between boreholes, length of fractures along boreholes, hydraulic apertures based on fracture sets	rjMCMC inversion algorithm

We apply a uniform prior as a lower and upper limit for the unknown parameters, that is, for the coordinates of the center of each fracture and the fracture length. The characterization of the error between simulated and measured data by estimating its standard deviation can be utilized to quantify uncertainties of the conceptual model, for example, deviations from the fracture sets or the assumed fracture shape, for resolving inconsistencies of conceptual model assumptions with respect to field conditions.

Table 3.3: Parameter setting of the inversion model.

Parameter	Fracture set 1	Fracture set 2	Fracture set 3
Hydraulic aperture	$6 \cdot 10^{-5}$ m	$8 \cdot 10^{-6}$ m	$6 \cdot 10^{-5}$ m
Inclination (Rotation around y-axis)	$167.9^\circ$	$56.7^\circ$	
Dip (Rotation around z-axis)		$65.9^\circ$	$90^\circ$
Rotation around x-axis			$75^\circ$
Specific storage		$2 \cdot 10^{-6} \text{ m}^{-1}$	

### 3.2.5 Evaluation of the results

During the MCMC search, initially tested DFN configurations and the following sample realizations proved unsuitable for the posterior distribution, since the misfit between the simulated and the measured pressure signals is relatively high due to inexact connections between the boreholes. Therefore, samples from the beginning of the MCMC procedure are discarded as burn-in realizations. Assuming that little is known about the posterior distribution, the evaluated results originate from different initial DFN configurations drawn from the prior distribution. This avoids getting stuck in local modes of the posterior distribution and respectively prevents the results from only partially covering the posterior. To reduce the autocorrelation, only every  $n$ th iteration is kept for the evaluation of the results, which is called thinning (Brooks et al., 2011).

The DFN realizations, that is, the samples from the posterior distribution, obtained by the rjMCMC algorithm, are evaluated as fracture probability maps (FPMs). Due to the changing number of parameters, single fractures and their influence are difficult to distinguish from each other and, therefore, FPMs are a more suitable evaluation method than, for example, histograms on individual fracture statistics. Since a fracture can be inserted at an arbitrary position in the investigated rock volume, a new fracture is not necessarily connected to the main DFN. Therefore, unconnected fractures, that is, fractures without influence on the flow, are discarded for the generation of the FPM. Similar to the mesh generation, the function Boolean intersection by the mesh generator *Gmsh* is implemented to detect unconnected fractures. The FPM is evaluated by generating a raster of each DFN realization and taking the mean of all DFN realizations. Thereby, the FPM presents the sample mean for each volume of the raster to be a part of a fracture, which is interpreted as fracture probability. The updates of the fracture aperture are evaluated on the same raster over the investigated volume. If an element of the raster is part of the DFN, the corresponding aperture is selected from the explicit representation of the DFN. This is used to calculate the mean fracture aperture of each element of the raster.

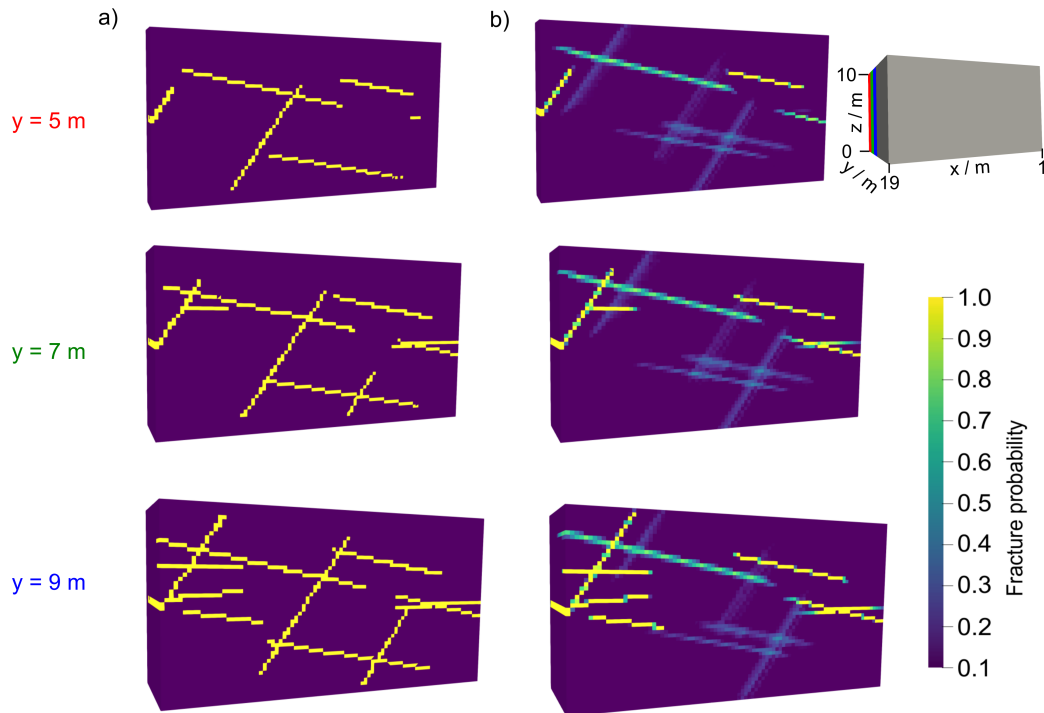


Figure 3.4: (a) Rasterized test case 1. (b) Inversion results illustrated as FPM presented for constant positions  $y$  (as illustrated at the upper right together with the size of the evaluated volume).

### 3.3 Results

#### 3.3.1 Test case 1

The rjMCMC samples are evaluated as FPM presenting the mean over the DFN realizations. In Fig. 3.4b, the FPM derived for the base case is illustrated in different cross sections for constant values  $y$ . For better comparability of the results with the test case, a raster of the synthetic DFN is generated with the same resolution as the FPM (Fig. 3.4a). Fracture probabilities below 10% are neglected for the sake of clarity of the visualization. Note that the bounds of the modeled domain are greater than what is presented in Fig. 3.4 and some fractures can partially extend over the bounds of the displayed volume.

In general, the shown cross sections reveal fractured and non-fractured areas. The main characteristics of the inverted DFN are precise and accord with the synthetic test case. This illustration of the results also indicates which parameters of the DFN can be inferred with certainty or uncertainty by the inversion algorithm. Parameters that are well constrained by the hydraulic tomography experiment can be estimated properly, while parameters that have only a small effect on the pressure signals occur



with a broader range of possible values. The fracture connecting the fractures from injection borehole 2 (Fig. 3.2a) with the right part of the investigated volume has a direct influence on the pressure signals, therefore, only small deviations from the mean position are possible. Otherwise, the error would be too large, that is, this realization would be less likely. The hydraulic effect of the other fractures on the flow is lower and thus larger fluctuations around an expected value are possible in the inverted results. In particular, the  $y$ -coordinates of all fractures are not well determined, instead, they can move quite freely on the  $x$ - $z$ -plane. The effects of varying the length of all fractures are visible by the lower fracture probabilities at the end of each fracture. More pressure signals are available for injection borehole 2 than for borehole 1. The combinations of source/receiver 3, 4, and 5 among each other allow the expected fracture length of the fractures connected to injection borehole 2 to be well determined, and fewer deviations are possible compared to the fracture lengths at injection borehole 1 (Fig. 3.2a).

Figure 3.2b shows the mean of the simulated pressure signals of the posterior DFN realizations compared to the pressure signals that function as basis for the inversion. Since the conceptual model coincides with the setup of the test cases, the mean signals accord well with the measured signals. For the inversion of field data, further parameters like the error variance or quantiles of the simulated data can be evaluated to consider uncertainties in the conceptual model. For the synthetic test cases of this study, the uncertainty of the data and the results correlate with the scale of the noise added to the pressure signals. If the approximate number of fractures can be evaluated based on the FPM, application of MCMC algorithms that require the number of fractures to be given can provide additional insight into the DFN parameters and their correlations. Results from such inversion setups with a constant number of fractures are available in the supplement. In general, the results from the inversion setup with a fixed number of fractures agree with the presented rjMCMC results, which serves as a confirmation of the results. However, due to the uncertainty about the number of fractures in a rock mass, in practice, a transdimensional implementation is favorable for the first step of inversion.

### 3.3.2 Test case 2

This test case expands the previous base case by coupled inversion of likewise hydraulic apertures. The latter are inverted within a range of possible values based on the fracture sets. The obtained fracture probability (Fig. 3.5a) and the sample mean of the hydraulic aperture of each element of the raster are evaluated in Fig. 3.3b. Fracture probabilities below 10% are not displayed in the FPM. Accordingly, no aperture value is given, since a reasonable estimate of the mean aperture is not possible for these elements.

In general, the overall uncertainty of the results is increased due to the estimation of an additional parameter of each fracture. In comparison to the previous results (Fig. 3.4), more raster elements with low fracture probabilities and probabilities below 10% exist and the resolution of the FPM is lower. As a whole, the fracture

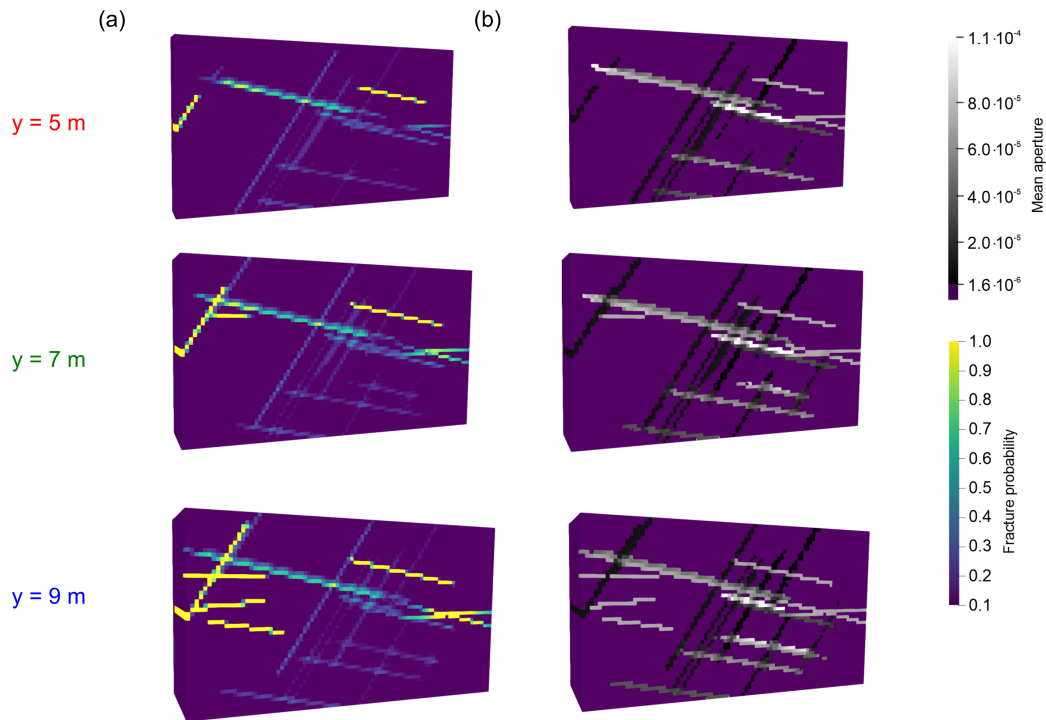


Figure 3.5: Inversion results of test case 2 evaluated as (a) fracture probability map and (b) mean aperture of each element. We refer to Fig. 3.4a for comparison with the rasterized test case and for the size of the displayed volume.

aperture correlates mainly with the number of fractures and the position of the other fractures. For example, more fractures in parallel with a small distance, can compensate for an underestimated aperture at the same position. However, the separate effect of the inverted parameters of the DFN even representing a similar position is difficult to quantify.

Despite the coarse resolution of the FPM, the results in Fig. 3.5 facilitate the following conclusions regarding the properties of the DFN: The horizontal connection in the upper part of the investigated volume is apparent and the mean aperture value accords approximately with the aperture from the setup of the test case. In contrast to the previous results with a fixed hydraulic aperture (Fig. 3.4), more DFN realizations appear in the lower part of the domain. And analogous to this, new intersections of the fractures of the different fracture sets are found suitable. This shows that the given tomographic data and prior information are not sufficient for reliable reconstruction of the given DFN of test case 2. While the inversion result comes close to the original DFN, the additional flexibility of calibrating the hydraulic aperture offers more freedom and allows more diverse candidate solutions. Obviously, such findings are still useful, especially when judging the suitability of

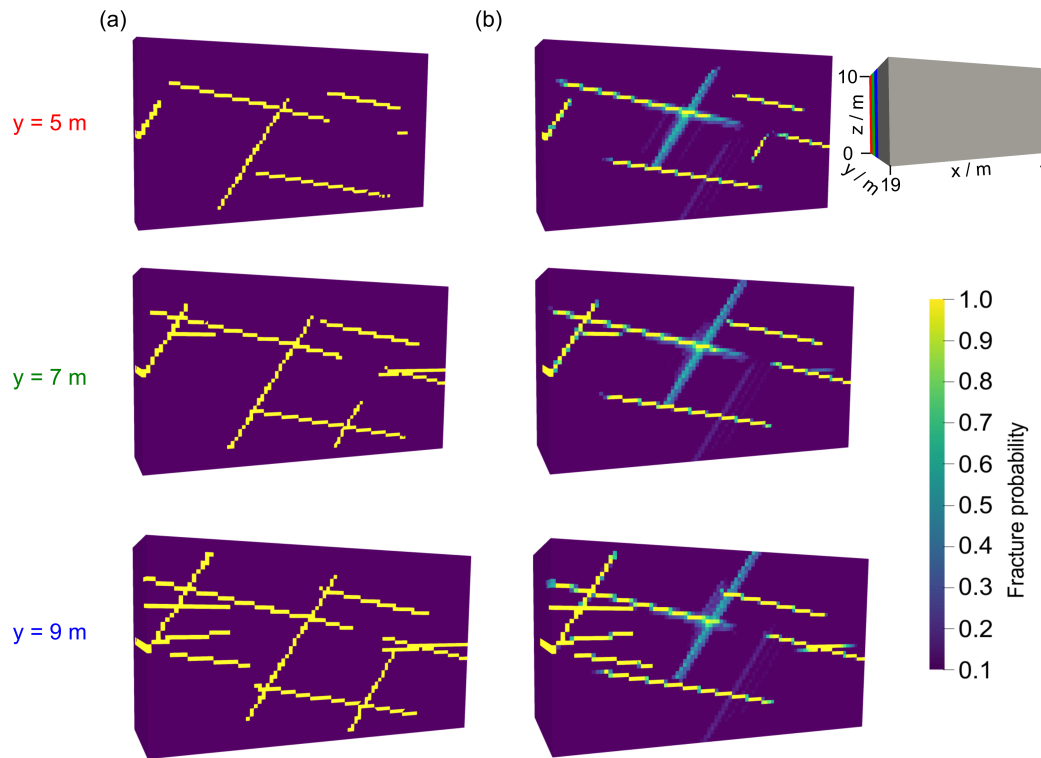


Figure 3.6: (a) Rasterized test case 3. (b) Inversion results illustrated as FPM for different cross sections for constant values  $y$ . Fracture probabilities below 10% are neglected.

different field data, and for deriving strategies of optimized additional field surveys or data requirements to better constrain the DFN inversion.

### 3.3.3 Test case 3

In test case 3, the role of a modified tomographic setup is examined with fixed apertures. Once again, using the base case as reference, an additional injection point provides more tomographic information. In general, the inversion results obtained by the rjMCMC algorithm demonstrate that it is possible to constrain the properties of the fractures by the extra injection point (Fig. 3.3a). Figure 3.6b indicates that the resolution of the inversion results is better in contrast to results from the base test case presented in Fig. 3.4. Due to the additional source/receiver point in the lower part of the investigated rock volume, the fractures in this part cause a more direct influence on the fluid flow in comparison to the previous base case. Therefore, the uncertainty of the inversion results is generally reduced. The fracture of fracture set 1 with the connection to S/R 6 exhibits less variance from the mean position compared to the initial setup given by the base case. The fracture of the second

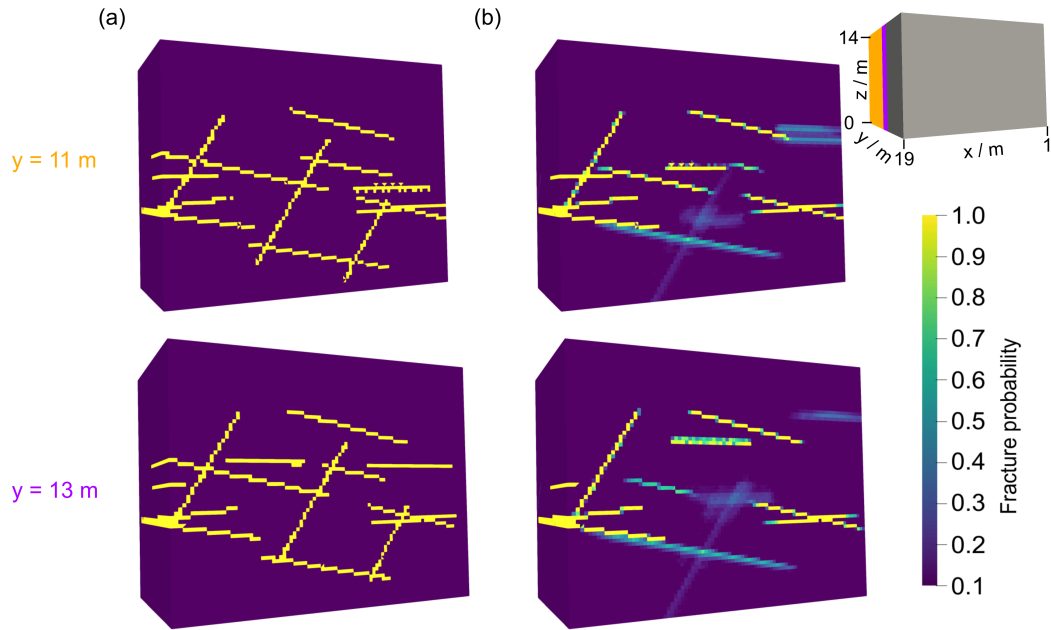


Figure 3.7: (a) Rasterized test case 4. (b) Inversion results illustrated as FPM presented for different cross sections for constant values  $y$ . Fracture probabilities below 10% are neglected.

fracture set, which connects the two fractures of the first set, respectively the upper and the lower part of the investigated rock volume, also deviates only slightly from the mean position. Since S/R 6 is shifted backward (Fig. 3.3a), this setup of the test case also enables better constraint of the  $y$ -coordinates of the center of the fractures. This also clarifies that it would not have been possible to reduce the inversion to a 2D problem without disregarding information on the 3D properties of the DFN. This example demonstrates that the results for test case 1 can be used to infer a suitable location for additional S/R points. Assuming no practical restrictions for the insertion of S/R points, the best effect could be achieved by placing it at positions where the resolution of the FPM is lowest.

### 3.3.4 Test case 4

In this case, the inversion result is obtained with a higher uncertainty compared to the previous examples. The accuracy of the inversion results is also lower. This originates mainly from the rotation around the  $x$ -axis according to the third fracture set and more possible flow paths due to more fractures, which leads to more uncertainty. However, a few useful conclusions about the structure of the DFN can still be drawn from the inversion results. The FPM is shown for different cross sections in Fig. 3.7b. The fractures of the third fracture set, readily identifiable by the straight line, are located in the upper part of the investigated rock volume, which coincides

with the setup of the test case (Fig. 3.3c). The FPM also reveals the appearance of fractures in the lower part, although the expected position is more difficult to determine. Especially the  $y$ -coordinate of the fractures is hard to specify more precisely. Obviously, there is not enough data available for reliable inversion. The resolution of the inversion results could, however, be improved by more prior information such as from other measurements or an additional source/receiver point in the lower part of the investigated volume similar to the one for the second test case.

### 3.3.5 Comparison of the results for all four test cases

We apply around 1,500 posterior samples for each test case to generate the FPM after discarding the burn-in iterations (approximately 40,000 depending on the initial guess and the proposed updates), and after thinning the posterior realizations (we keep every 100th iteration). Altogether, that is a rather conservative approach. However, that should ensure the representation of all possible DFN realizations to provide reasonable estimates about the uncertainties of the parameters. In general, it is a complex process to determine if the DFN samples capture the whole posterior distribution. We circumvent this issue by comparing and summarizing the results from different initial guesses as starting points of the inversion. If the results are similar or recurring, it is a good indication that the procedure can be terminated. This procedure will become even more important when dealing with real measured data.

Comparing the results from the base case and test case 3, an extra source/receiver point provides sufficient data to better resolve the inversion results, respectively reducing the uncertainty. However, this also has the effect that the algorithm is more prone to get stuck in a local minimum during the burn-in phase if only a part of the pressure signals is met. Therefore, test case 3 requires more burn-in iterations than the other examples. In contrast to this test case, test case 4 demonstrates that more available flow paths decrease the impact of a single fracture on the pressure signals and therefore, reduce the accuracy of the results. This is comparable to the findings with a flexible aperture value as tackled by test case 2. Here, the greater flexibility and thus expanded mathematical decision space facilitates more suitable DFN variants as solutions. This is as expected and thus reflects a good performance of the rjMCMC procedure.

## 3.4 Conclusions and outlook

In this study, we applied a Bayesian framework and the rjMCMC sampling strategy to flexibly calibrate the parameters of a 3D DFN to data from hydraulic tomography and to adjust to prior information. This is accomplished by representing and inferring, in particular, the geometrical properties of the DFN explicitly. The main advantage of the stochastic inversion procedure is the generation of a set of possible DFN realizations that are approximately equally likely. This facilitates being able to distinguish between parameters or fractures that are identified with higher or

lower certainty. The inversion results for the synthetic test cases demonstrate the capability of characterizing the main flow path between the source/receiver points, as this has the greatest influence on the outcome of the hydraulic tomography experiment. The properties of the other fractures, whose contribution to the pressure signals is less, are subject to higher uncertainty, that is, the resolution of the inversion result is lower. Despite the higher uncertainty, the existence of such fractures is substantiated and can be further analyzed by introducing additional information, for instance, by complementary field investigation.

In one test case, the estimation of the hydraulic aperture is integrated in the inversion algorithm as part of the parameter update of the DFN. However, future research is required on the evaluation of the results, mostly concerning the correlation of the hydraulic aperture with the position and number of fractures. Also, the overall performance of the rjMCMC algorithm and the possibilities regarding the evaluation of the results could be improved by defining two additional update types, like merging nearby fractures and for the reversibility of the chain splitting fractures. These update types could provide a better estimate of the effect of a single fracture and, therefore, offer additional options for the evaluation.

The same inversion framework and MCMC algorithms can be applied to the characterization of DFNs in combination with different forward solvers to consider either more complex physics like coupled flow and transport processes or different sources of measurement data, for example, data from tracer or stress-based tomography. Further information about the DFN, for example, from geophysical measurements or results from continuous inversion, can also be used in the flexible Bayesian framework as prior distribution to be applied to the inversion of more complicated problems. Mainly, three advantages are possible. First, introducing more constraints should reduce the variance of the results. In addition, more prior knowledge about the properties of the fractures is capable of reducing the computational costs by shortening the burn-in phase due to better initial guesses. Third, inversion problems that include the update of the fracture aperture will benefit from information about the transmissivity because of the direct connection between aperture and transmissivity.

The presented evaluation with the different synthetic test cases helps to learn about the features and difficulties of the inversion algorithms together with the potential integration of additional prior information. Ultimately, the results serve as preparation for DFN inversion with measured field data.

# 4 Characterization of the highly fractured zone at the Grimsel Test Site based on hydraulic tomography

## Abstract

In this study, we infer the structural and hydraulic properties of the highly fractured zone at the Grimsel Test Site in Switzerland using a stochastic inversion method. The fractured rock is modeled directly as a discrete fracture network (DFN) within an impermeable rock matrix. Crosshole transient pressure signals recorded from constant rate injection tests at different intervals provide the basis for the (herein presented) first field application of the inversion. The experimental setup is realized by a multi-packer system. The geological mapping of the structures intercepted by boreholes as well as data from previous studies that were undertaken as part of the In situ Stimulation and Circulation (ISC) experiments facilitate the setup of the site-dependent conceptual and forward model. The inversion results show that two preferential flow paths between the two boreholes can be distinguished: one is dominated by fractures with large hydraulic apertures, whereas the other path consists mainly of fractures with a smaller aperture. The probability of fractures linking both flow paths increases the closer we are at the second injection borehole. These results are in accordance with the findings of other studies conducted at the site during the ISC measurement campaign and add new insights into the highly fractured zone at this prominent study site.

## 4.1 Introduction

Solid rocks, such as in crystalline and bedrock formations, typically have a compact matrix of low permeability. Water pathways are focused on mechanical discontinuities that separate individual rock blocks over multiple scales. Such fractures are commonly described as planar structures and form a network that is hard to resolve at field sites. This is due to the high diversity and complexity of natural fracture networks, the difficulty involved with identifying fracture connectivities, and thus the difficulty involved with interpreting the hydraulic regime of an entire formation based on local fracture detection. Accordingly, fractured-aquifer characterization represents a challenge, with a relatively high cost related to the application of specialized field investigation techniques and to gathering a sufficient data set for reliable hydraulic description.

The general poor understanding of how groundwater flows in fractured field sites is in contrast to the relevance of fractured environments that host elementary fresh-water reservoirs worldwide (Chandra et al., 2019; Spencer et al., 2021; Wilske et al., 2020). Moreover, adequate characterization of the properties of fractured field sites concerns many subsurface engineering applications, such as the planning and operation of enhanced geothermal systems (Kittilä et al., 2020; Vogler et al., 2017), the evaluation of potential sites for a nuclear waste repositories (Follin et al., 2014; Li et al., 2022), or the description of an excavation-induced damaged zone around tunnels and openings (Armand et al., 2014; de La Vaissière et al., 2015).

Depending on the chosen experimental setting and the available data, different interpretations of the hydraulic and structural properties of a fracture network are possible. A fractured site can be inspected locally by borehole data (e.g., core mapping and geophysical image logs such as optical or acoustic televiewer). The depth and orientation of structures intercepted by boreholes characterize fracture intensity and prevalent fracture orientations (Armand et al., 2014; Chandra et al., 2019; Krietsch et al., 2018; Pavičić et al., 2021; Tan et al., 2020; Yin and Chen, 2020); furthermore, by fitting probability distributions to the parameters, a statistical analysis can be conducted (Barthélémy et al., 2009; Massiot et al., 2017). Single-hole and cross-hole flow and tracer tests are employed to infer permeability and connectivity between different borehole intervals (Brixel et al., 2020a,b; de La Bernardie et al., 2018; de La Vaissière et al., 2015; Follin et al., 2014; Jalali et al., 2018; Le Borgne et al., 2006; Li et al., 2022; Tan et al., 2020), the velocity distribution (Kang et al., 2015), or transport properties (Kittilä et al., 2019; Lee et al., 2019).

Detailed insight into the properties of flow paths between adjacent boreholes can be gained by tomographic methods. The principle of all tomographic methods is perturbing the investigated system (e.g., by an injection of fluid, a tracer, a thermal anomaly, or an electric current) and recording the response at nearby receivers. In particular, geophysical tomographic methods are applied for the characterization of the rock properties, the identification of fractured (in particular highly fractured) zones, and the monitoring of flow pathways (Deparis et al., 2008; Doetsch et al., 2020; Dorn et al., 2012; Robinson et al., 2016).

This is frequently done in combination with hydrogeological methods (Chen et al., 2006; Day-Lewis et al., 2003; Dorn et al., 2013; Giertzuch et al., 2021a,b; Voorn et al., 2015). A comprehensive portrayal of geophysical methods for the investigation of fractured field sites and the potential target applications is given in Day-Lewis et al. (2017).

In contrast to geophysical exploration techniques, hydraulic, pneumatic, or tracer tomography is based on a fluid or tracer injection at a source well. The response is recorded at different adjacent boreholes at different depth intervals. In most cases, the pressure signals or tracer arrival curves are evaluated by a continuous hydraulic conductivity distribution based on an equivalent porous media (EPM) concept (Dong et al., 2019; Illman et al., 2008, 2009; Jiang et al., 2022; Kittilä et al., 2020; Liu et al., 2022; Poduri et al., 2021; Sharmeen et al., 2012; Tiedeman and Barrash, 2020; Yeh and Liu, 2000; Zha et al., 2015, 2016; Zhao and Illman, 2017; Zhao et al., 2021).



Thus, detected high conductivity zones correspond to the locations of fractures or faults.

Further insights into the fracture properties and improved results can be gained by particle tracking simulations (Tiedeman and Barrash, 2020), binary priors representing either fracture or matrix (Poduri et al., 2021), or by generating synthetic models with similar features to the field site (Zha et al., 2015). Geostatistical methods apply a stochastic EPM, and different realizations of the subsurface are evaluated (Blessent et al., 2011; Park et al., 2004; Wang et al., 2017). Here, different facies represent different levels of fractured or intact rock, for which hydraulic conductivities are calibrated. In contrast to the EPM approach, the properties of the fracture network are inferred more directly by calibrating a connectivity pattern (Fischer et al., 2018a,c; Klepikova et al., 2020).

Our inversion approach differs from previous studies insofar as the fractured rock is represented explicitly as a discrete fracture network (DFN) and the hydraulic and structural parameters of the fractures are inferred directly. The great number of unknown parameters prevents the minimization of an objective function between simulated and observed data, resulting in a single deterministic DFN. Instead, a stochastic approach is applied to consider the nonuniqueness of the results. This is accomplished by generating several realizations of the fracture network that are equally likely to be evaluated as a fracture probability map. The validity of the approach has been demonstrated for synthetic test cases in two dimensions (2D) (Ringel et al., 2019; Somogyvári et al., 2017) and three dimensions (3D) (Ringel et al., 2021).

In this study, the new inversion method is applied to field data for the first time. We use transient pressure signals from hydraulic tomography experiments conducted as part of the In situ Stimulation and Circulation (ISC) experiments at the Grimsel Test Site (GTS) in Switzerland. Proper evaluation and validation of a new approach requires controlled tests, and the GTS and ISC experiments pose a well-explored site for experimental validation. The objective of this paper is to reveal the feasibility and capability of 3D DFN inversion using a small-scale example. This study provides an elementary link between the theoretical development of a new inversion algorithm based on synthetic test cases and field applications, although the small scale may not be representative of the much larger scale of groundwater reservoirs.

The paper is structured as follows: in the first part (Section 4.2), we describe the site and the hydraulic tomography experiments to be used for the inversion. The implementation of the inversion is elaborated upon in the second part (Section 4.3). We review the forward modeling procedure and the general inversion framework developed in previous works with synthetic test cases. We then explain the site-dependent inversion setting (i.e., the conceptual model and the prior parameter distributions that serve as basis for a stochastic inversion procedure) and discuss and justify the necessary constraints and assumptions. The inversion results are interpreted and compared with findings from related ISC experiments.

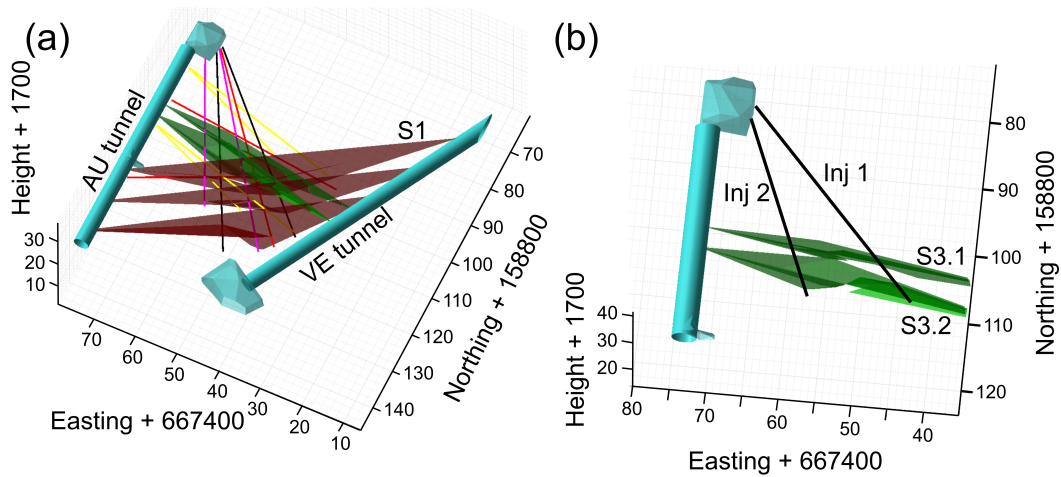


Figure 4.1: (a) General overview of the ISC experimental site showing the AU (Auflockerungszone, i.e., excavation effects) tunnel, the VE (ventilation test) tunnel, all boreholes, and the two types of shear zones (Krietsch et al., 2018). (b) The volume that is investigated in this study, i.e., the zone between the two brittle-ductile (S3) faults.

## 4.2 Experimental setting

### 4.2.1 Test site

The GTS is an underground rock laboratory located in the Aar Massif in the Swiss Alps. The ISC experiments, which serve as the basis for this study, utilized 15 boreholes of 20 m to 50 m depth, including two injection boreholes (Inj1 and Inj2). The other boreholes are used for stress and strain measurement as well as seismic, pressure, and temperature monitoring during the hydraulic stimulation phases (Krietsch et al., 2018). A general overview of the site showing the persistent structures and the boreholes is given in Fig. 4.1a. A summary of the experiments conducted during the ISC measurement campaign and their results are given in Amann et al. (2018) and Doetsch et al. (2018).

The crystalline rock in the southern part of the GTS (ISC experiment volume) has been moderately fractured. Ductile (S1) and brittle-ductile (S3) shear zones can be distinguished from the investigated rock volume (Fig. 4.1a; Krietsch et al. (2018)). The shear zones consist of a fault core, a damage zone, and unperturbed host rock (Wenning et al., 2018). A 4 m to 6 m highly fractured zone with a fracture density (P10) of around  $3 \text{ m}^{-1}$  is present between the fault cores of the two S3 shear zones and is displayed in Fig. 4.1b. The fractures can be distinguished in wall damage zones adjacent to the S3 faults and linking damage zones, i.e., fractures connecting both fault cores (Brixel et al., 2020b). Testing campaigns on the connectivity between

Table 4.1: Parameters of the packer intervals and the hydraulic tomography experiments.

Interval	Interval depth [m]	Injection flow rate [ml min <sup>-1</sup> ]	Injection time [min]
Inj1-Int3	30 – 34	60	60
Inj1-Int4	27 – 29	400	30
Inj2-Int3	25 – 29	60	60
Inj2-Int4	22 – 24	400	12

several intervals of the injection boreholes revealed that the best response occurs between the intervals 3 and 4 of both injection boreholes, which are located in the aforementioned highly fractured zone. Therefore, this is not only a highly fractured zone but also the most permeable region with conductive fractures (Jalali et al., 2018). For this reason, the characterization of the hydraulic and structural properties of this region (Fig. 4.1b) is the target of this study. The geological mapping of the structures intercepted by the boreholes and tunnels provides the basis for the setup of the conceptual model (Krietsch et al., 2018).

#### 4.2.2 Hydraulic tomography data

The hydraulic tomography tests that are applied in this study are part of the characterization phase of the ISC experiment. We utilize transient pressure signals from constant rate injection tests in the intervals 3 and 4 of the injection boreholes Inj1 and Inj2. The different intervals are isolated by a multi-packer system. The properties of the packer intervals and the parameters of the injection are summarized in Table 4.1. Between each injection experiment, pressure recovery was possible. The pressure response of the fluid is measured using piezoresistive pressure transducers. The resolution of the pressure response data is approximately 0.5 kPa. The minimum principal stress is of the order of 8 MPa. As the injected fluid pressure is much below the minimum principal stress, the coupling between hydraulic and mechanical effects can be neglected in the forward modeling of the experiment. The fluid pressure is measured with  $\Delta t = 2$  s. In general, we use similar hydraulic tomography experiments as those applied by Klepikova et al. (2020) except for a shorter injection time (Table 4.1), which was chosen for computational reasons.

The pressure signals are shown in Fig. 4.2 for each injection interval. Due to the stochastic inversion approach, the noisy pressure response data can be directly utilized for the inversion without the necessity to smooth or filter the signals.

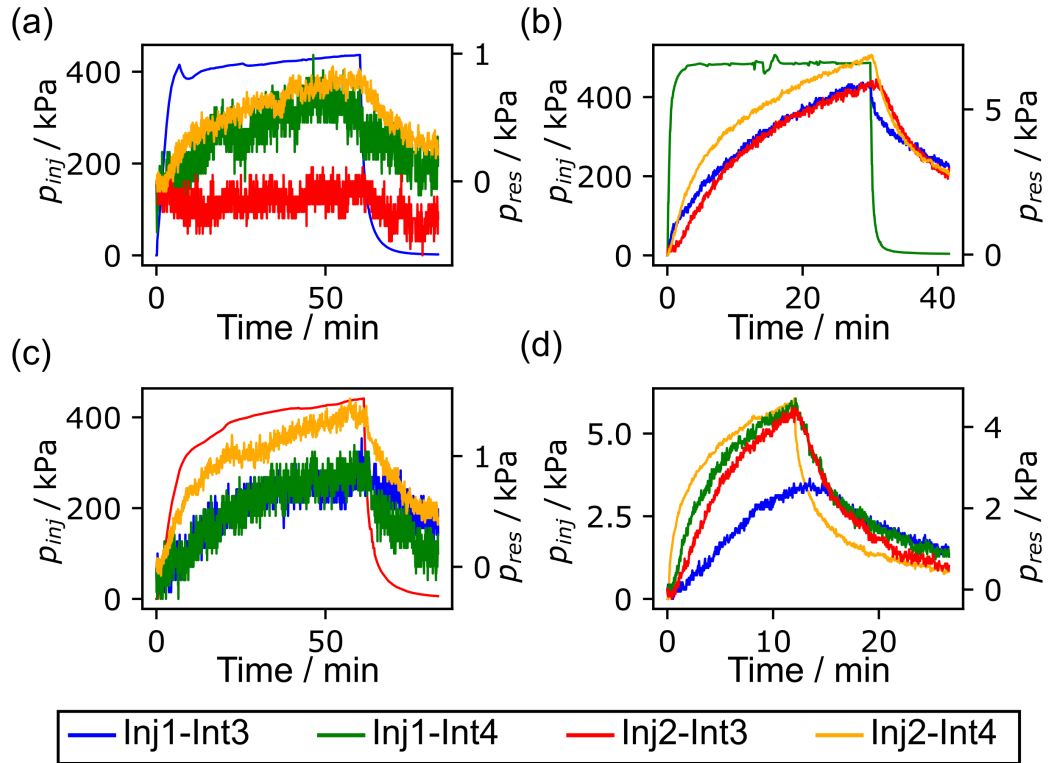


Figure 4.2: Pressure response in the different intervals provoked by a constant rate injection applied sequentially to the intervals Inj1-Int3 (a), Inj1-Int4 (b), Inj2-Int3 (c), and Inj2-Int4 (d), according to Table 4.1. The pressure measured in the respective injection interval belongs to the left vertical axes, and the pressure signals measured in the observation intervals to the right vertical axes.

## 4.3 Implementation of the inversion

### 4.3.1 Forward modeling

Fractures are modeled as 2D objects with constant properties normal to the fracture midplane in a 3D rock matrix that is assumed to be impermeable. The pressure diffusion in a single fracture is described by

$$a\rho S \frac{\partial p}{\partial t} - \nabla_T \cdot \left( a\rho \frac{k_f}{\mu} \nabla_T p \right) = aq, \quad (4.1)$$

where  $a$  [m] is the hydraulic aperture,  $\rho$  [ $\text{kg m}^{-3}$ ] is the density of the fluid,  $S$  [ $\text{Pa}^{-1}$ ] is the specific storage,  $k_f$  [ $\text{m}^2$ ] is the permeability,  $\mu$  [ $\text{Pa s}$ ] is the dynamic viscosity, and  $q$  [ $\text{kg m}^{-3} \text{s}^{-1}$ ] is a source/sink term. The pressure  $p$  [Pa] consists of the static pressure and the piezometric pressure.

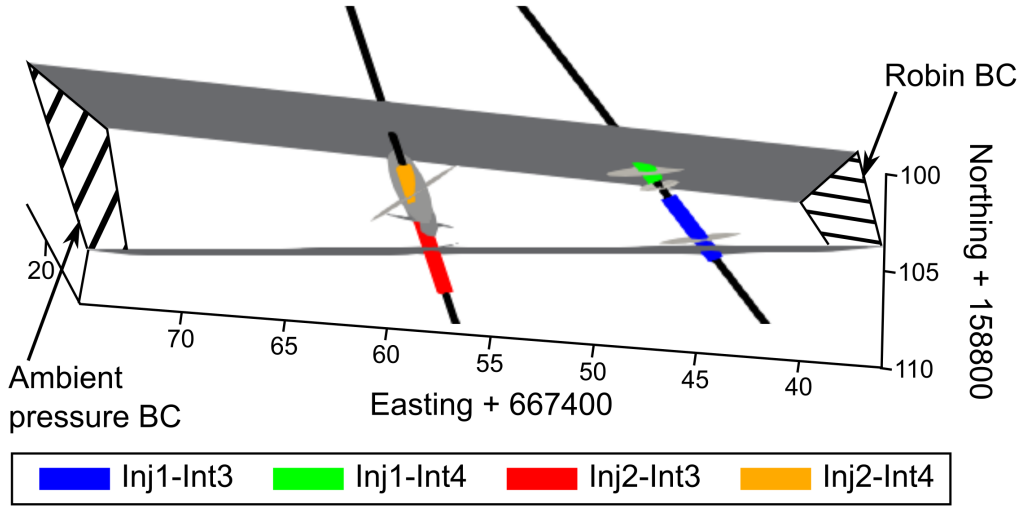


Figure 4.3: Overview of the volume considered in the forward model and the boundary conditions (BCs). The geometry of the S3 faults is simplified to planes, and the fractures intercepted by the injection intervals are illustrated as plane ellipses.

The permeability is related to the aperture by

$$k_f = \frac{a^2}{12}, \quad (4.2)$$

and the subscript T of the gradient ( $\nabla_T$ ) denotes that it is evaluated in the fracture plane (Berre et al., 2019; Zimmerman and Bodvarsson, 1996). In this study, flow in the shear zones is modeled using the same approach as flow in the DFN, i.e., the shear zones are represented as 2D objects whereby the flow parameters are given by hydraulic aperture and specific storage (Eq. 4.1). The equations are solved numerically using the finite element method (FEM) with a conforming discretization at the intersections of different fractures. The generation of the geometry and the meshing of the fractures and shear zones are implemented using the open-source mesh generator *Gmsh* (Geuzaine and Remacle, 2009). The geometry of each structure is created separately by the built-in geometry module of *Gmsh*. The fractures and the shear zones are connected for a conforming discretization at the intersections of different structures by the Boolean operations implemented in *Gmsh*.

The implemented boundary conditions are shown in Fig. 4.3 along with the S3 faults, and the fractures intercepted by the injection boreholes obtained from optical televiewer logs (Krietsch et al., 2018).

The boundary conditions are chosen considering the fact that only a small volume of the ISC experiment is investigated in this study. Therefore, the following boundary conditions are applied:

- The AU tunnel is represented by a pressure boundary condition – in this case, ambient pressure.
- The way to the VE tunnel cannot be modeled explicitly. Thus, we apply a Robin boundary condition as a transfer boundary condition to consider the transition of the flow and the extension of the shear zones towards the VE tunnel (Watanabe et al., 2017).
- A no-flow boundary condition is applied normal to the planes of the fractures and shear zones.

### 4.3.2 Inversion algorithm

The parameters of the DFN  $\theta$  are treated as unknowns characterized by probability density functions. Based on the Bayesian equation, the posterior density function  $p(\theta|\mathbf{d})$  of the parameters given the measured data  $\mathbf{d}$  is proportional to the likelihood function

$$\log L(\mathbf{d}|\theta) \propto - \sum_{i=1}^{N_{\text{data}}} \frac{(d_i - f(\theta)_i)^2}{2\sigma_i^2} \quad (4.3)$$

and the prior distributions  $p(\theta)$  (Gelman et al., 2013). The term  $f(\theta)$  refers to the forward simulation of the hydraulic tomography experiment for the DFN realization defined by the parameters  $\theta$ . The posterior density function is evaluated by sampling from it according to Markov chain Monte Carlo (MCMC) methods. This is an iterative procedure whereby new samples  $\theta'$  are proposed by a proposal function and accepted ( $\theta_i = \theta'$ ) with probability

$$\alpha = \min \left( 1, \frac{p(\theta'|\mathbf{d})q(\theta_{i-1}|\theta')}{p(\theta_{i-1}|\mathbf{d})q(\theta'|\theta_{i-1})|J|} \right) \quad (4.4)$$

or rejected ( $\theta_i = \theta_{i-1}$ ) (Brooks et al., 2011). The so-called reversible jump MCMC algorithm allows one to change the number of parameters (Green, 1995). In this study, the number of parameters is adjusted by deleting or inserting a fracture within the prior bounds. The determinant of the Jacobian matrix  $|J|$  has to be considered for transdimensional updates. It equals 1 for parameters sampled from the prior without linking its value to preexisting parameters (Sambridge et al., 2006). The parameters of the inversion problem are adjusted by proposing a new value from a normal distribution whereby the mean of the normal distribution is given by the current value.

The variance  $\sigma^2$  in the likelihood function (Eq. 4.3) accounts for different sources of uncertainties, such as measurement errors, modeling errors, and errors of the conceptual model. Therefore, the value of the variance is estimated separately for

each pressure signal. This is implemented as part of the inversion algorithm after the update of the parameters of the DFN. The measured data are assumed to consist of a mean and a normally distributed error  $\mathbf{d} = \bar{\mathbf{d}} + \mathcal{N}(0, \sigma^2)$ . With this assumption, the variance can be estimated by sampling from an inverse gamma distribution

$$\sigma^2 | \mathbf{d}, \theta \sim \mathcal{IG} \left( \frac{N_{\text{data}}}{2}, \frac{\sum_{i=1}^{N_{\text{data}}} (d_i - f(\theta)_i)^2}{2} \right) \quad (4.5)$$

as introduced by Gelman (2006) and implemented by authors including Haario et al. (2006) and Ringel et al. (2019). For this reason, the noisy measured data can be directly utilized for the inversion without filtering or smoothing the signals.

In practice, one iteration of the inversion algorithm operates as follows: assuming that the insertion of a fracture is chosen in the MCMC algorithm, the parameters (position; length; fracture set, i.e., orientation; and hydraulic aperture) of the fracture are generated from the prior functions. The chosen parameters are evaluated by simulating the hydraulic tomography experiment with the proposed parameter set  $\theta$  (i.e., including the new fracture). The outcome of the simulation is compared to the measured pressure signals. If the error is smaller (the likelihood, Eq. 4.3, is higher) or similar to the previous step (without the fracture), the acceptance probability (Eq. 4.4) is high (Ringel et al., 2021). After accepting or rejecting the proposed parameters, the variance is updated according to Eq. 4.5.

### 4.3.3 Inversion constraints

The overall inversion procedure relies on several simplifications concerning parameters with less importance for our research target. For instance, the parameters specifying the properties of the shear zones have to be fixed. In general, our aim is an optimal balance between the accuracy of the generated results and the computational cost of the inversion procedure.

The underlying conceptual model comprises simplifications of the properties of single fractures that serve as inversion constraints. We assume plane ellipses as the fracture shape, and the length of the minor axis equals half of the length of the major axis (i.e., the length ratio is fixed). The assumption of reducing the fracture shape to a 2D plane is a common assumption and is justified by the derivation of the cubic law and the large ratio between the fracture extensions and the fracture aperture (Zimmerman and Bodvarsson, 1996). The assumption of the fracture shape as an ellipse is reasonable because the flow is dominated by the path between the intersections of different fractures; therefore, no sharp edges are considered for the simulation of the flow in the DFN. The hydraulic aperture is assumed to be constant over the fracture plane. Two fracture sets are defined with fixed orientations based on the orientations of the structures intercepted by the two injection boreholes. Thus, the fracture set is chosen by the inversion algorithm for the fractures between the boreholes; however, the orientation assigned to the fracture sets is a default. Figure 4.4 shows the orientation of the structures between the S3 shear

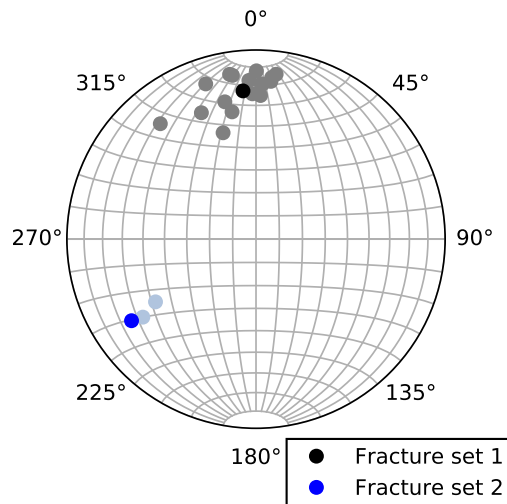


Figure 4.4: Orientations of the structures between the fault cores of the S3 shear zones in the injection boreholes observed from optical televiewer logs (Krietsch et al., 2018), shown in gray and light blue, as well as the calculated orientations for the fracture sets applied for the conceptual model.

zones intercepted by the two injection boreholes and the orientations defined for the two fracture sets. The appearance and distribution of the fractures dominate the flow. Accordingly, the surrounding rock matrix is assumed to be impermeable.

The investigated volume is limited to the volume between the two S3 shear zones (Fig. 4.1). The shear zones consist of a fault core and a damage zone. The permeability increases with distance from the fault core, where the cores are almost impermeable (Wenning et al., 2018). As the properties of the shear zones are not the target of this study, the shape is simplified and the associated hydraulic parameters are fixed. The shape of the shear zones is simplified to a plane rectangle (i.e., a linear interpolation between the shear zones' traces at the injection boreholes). A constant hydraulic aperture of  $a_{SZ} = 1 \cdot 10^{-5}$  m is assigned. This small value is chosen based on preliminary in situ tests and the knowledge that the cores of the shear zones are impermeable at their tunnel intersection. A higher permeability of the shear zone at specific locations can be covered by placing fractures in the respective area that also accounts for the spatial variability in the permeability of the shear zone. Moreover, the specific storage value is fixed at  $S_{SZ} = 1 \cdot 10^{-5}$  Pa<sup>-1</sup>. This high value is prescribed considering the results from cross-borehole tests (Klepikova et al., 2020). Fractures of fracture set 1 are approximately parallel to the S3 faults. Hence, a position close to an S3 fault also accounts for spatial changes in the permeability and specific storage of the S3 faults.

Overall, the application of constraints and assumptions about the fracture shape limit an exact reproduction of the structural properties of the tested rock mass.



Table 4.2: Uniform prior distributions defined by a minimum and maximum possible value.

	Minimum	Maximum
$x$ (easting + 667 400) [m]	45	70
$y$ (northing + 158 800) [m]	102	108
$z$ (height + 1 700) [m]	14	19
Fracture length [m]	0.4	7
Hydraulic aperture [m]	$1 \cdot 10^{-5}$	$1 \cdot 10^{-3}$
Specific storage [ $\text{Pa}^{-1}$ ]	$5 \cdot 10^{-10}$	$1 \cdot 10^{-6}$

All spatial values refer to the position of the midpoint of the ellipse.

However, those parameters that have a major influence on the flow in the DFN are adjusted by the inversion algorithm within prescribed bounds. These are, in particular, the position and the hydraulic aperture of fractures. In contrast, parameters with minor effects on the flow behavior are fixed (e.g., the exact fracture orientation or the length ratio).

#### 4.3.4 Prior distributions

The parameters to be inferred are the number of fractures, the position of the fractures, the fracture lengths, the respective hydraulic aperture for each fracture, and the specific storage coefficient that applies to the whole DFN. The specific storage  $S$  (Eq. 4.1) is given by the compressibility of water in theory (Freeze and Cherry, 1979). However, some fractures are only partially open; thus, due to the roughness of the surface, the specific storage can be increased compared with the theoretical value (Jalali et al., 2018). Moreover, the hydraulic aperture is generally smaller than the actual aperture (Berre et al., 2019). The specific storage is assumed to be valid for the whole DFN because two variable hydraulic parameters for each fracture are not feasible for the inversion algorithm. Accordingly, five different update types are implemented to be applied sequentially: the transdimensional update changes the number of parameters by either inserting a new fracture or deleting a fracture; the other update types keep the number of parameters constant but adjust position, length, hydraulic aperture, or the specific storage. For the update of the position, length, and hydraulic aperture, one fracture is chosen randomly, and a new value is proposed by a random perturbation of the current value.

Uniform prior distributions are applied, i.e., a parameter is specified by a constant probability between minimum and maximum possible values that are given in Table 4.2. The spatial priors are derived in general from the position of fractures intersecting the injection boreholes. The maximum value in the  $x$  direction corresponds to the distance to the AU tunnel to apply the boundary condition. The prior for the north direction is given such that the fractures are located between the cores of the S3 shear zones. The elevation of fractures is expected to have a minor influence on the flow between the two boreholes, and a broader pos-

sible range for the elevation would be less resolved. In the following,  $x$  refers to easting + 667 400 m,  $y$  to northing + 158 800 m, and  $z$  to height + 1 700 m (Fig. 4.1). The minimum value for the fracture length is given by the borehole diameter, and the maximum possible value corresponds to the distance between the shear zones. Fractures proposed during iterative inversion which intersect with the fault cores of the shear zones are reduced to the part of the fracture within the investigated volume (Figs. 4.1b, 4.3). The prior range for the aperture is approximated from the results of single- and cross-borehole tests (Brixel et al., 2020a,b; Jalali et al., 2018). The minimum specific storage value is given by the compressibility of water (Freeze and Cherry, 1979), whereas the maximum value is based on cross-borehole injection tests (Klepikova et al., 2020). Both prior distributions for the hydraulic parameters cause the flow preferentially in the DFN rather than in the shear zones, due to a smaller specific storage and a larger hydraulic aperture of the fractures.

## 4.4 Results

### 4.4.1 Processing of the results

Overall, 27,000 DFN realizations are considered to be posterior DFN realizations because they minimize the error and fulfill the prior conditions. DFN realizations from the initial 500 iterations are discarded as so-called “burn-in” iterations due to a higher error. The computation of the inversion was executed by an Intel Core i9 workstation with 10 cores and 128GB RAM and took about one week. The posterior realizations are approximately equally likely. They reflect the uncertainty of the inversion results in contrast to a unique solution that would be obtained by a deterministic approach. To reduce the autocorrelation of the results, we keep every 100th realization for further processing, which is called “thinning” (Brooks et al., 2011). Using the stochastic approach applied here, the fit between the measured and simulated pressure signals of the hydraulic tomography experiment is evaluated by the posterior and prediction uncertainty. The posterior limits are calculated based on the simulated pressure signals of the posterior DFN realizations which correspond to the uncertainty of the inversion method. The uncertainty related to predicting new observations is a measure of the overall error as well as of conceptual simplifications, as it also considers the estimated variance (Eq. 4.5). The DFN realizations are evaluated using a fracture probability map (FPM) over the investigated volume. For this, the inspected rock volume is divided into raster elements. Each element records whether the element is part of a fracture. By taking the element-wise mean over all of the posterior DFN realizations, the probability that each raster element is part of a fracture is derived. The evaluation of the FPM summarizes the estimated position and length of the fractures (i.e., those parameters with major influence on the flow). The hydraulic aperture is evaluated on the same raster elements. If a raster element is part of a DFN realization, the respective aperture is taken from the DFN. Thus, the mean hydraulic aperture can be evaluated for each element.

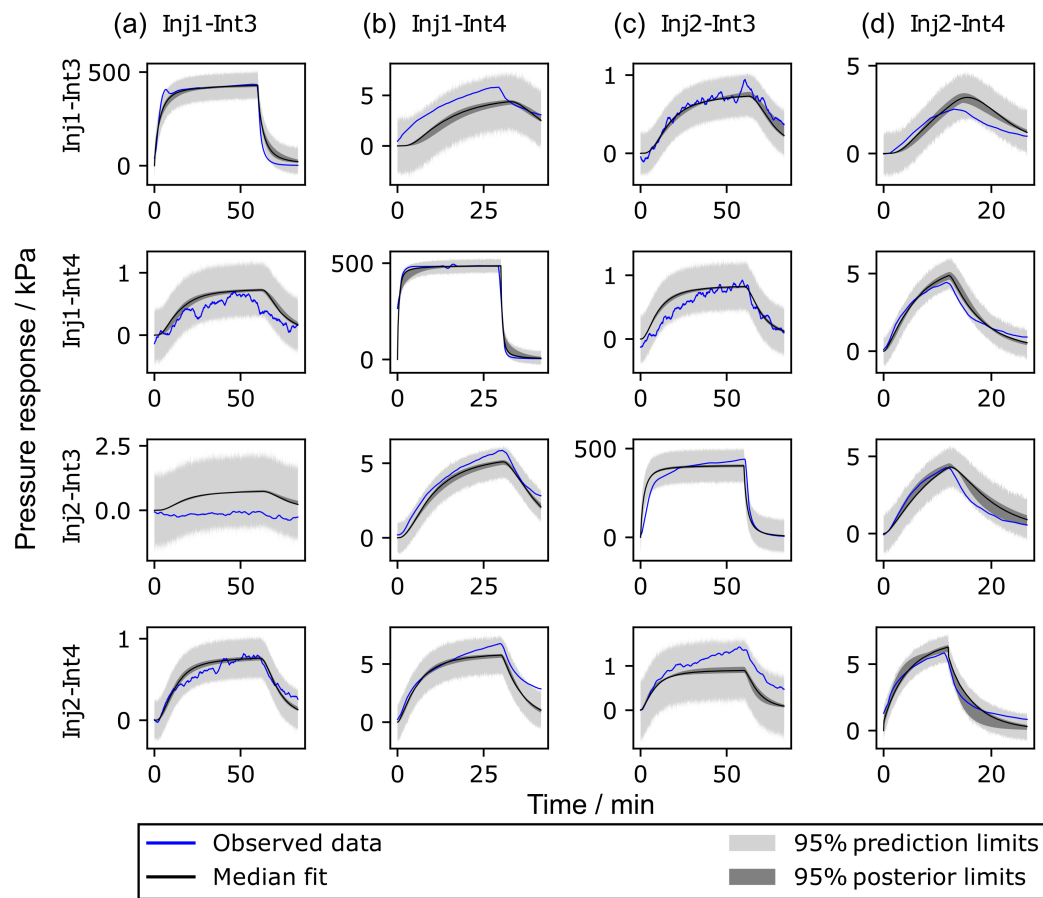


Figure 4.5: Comparison of the observed pressure response with the simulation of the hydraulic tomography experiment for the posterior DFN realizations for injection in the intervals Inj1–Int3 (a), Inj1–Int4 (b), Inj2–Int3 (c), and Inj2–Int4 (d), according to Table 4.1. For visual clarity, the observed pressure signals have been smoothed.

#### 4.4.2 Evaluation of the data

In the first step, the measured and simulated pressure signals are compared to assess the quality of the posterior realizations. Figure 4.5 shows the median fit and the 95% limits of the forward simulation of the posterior DFN realizations and the 95% limits of the prediction uncertainty along with the observed data.

Figure 4.5 demonstrates that the general shape and trend of the measured signals are reproduced by the simulated pressure curves checking the median fit and the 95% posterior limits. This is especially the case for the response in interval 4 of both boreholes. The weaker fit of some signals in interval 3 indicates effects not covered by the inversion approach or forward simulations, such as deviations from the

assumed fracture shape or fracture orientations. For a given DFN realization, the actual measured pressure signals are predicted. Due to measurement noise and simplifications concerning the DFN model, the 95% limits of the prediction uncertainty are wider than for the posterior uncertainty.

#### 4.4.3 Evaluation of the DFN realizations

The FPM and the mean hydraulic aperture are shown for different cross sections ( $z$ ) in Fig. 4.6. The fractures intercepted by the injection intervals and the shear zones are fixed; therefore, they appear with a probability of 100%. Their orientation, as derived from the optical televiewer logs, is assigned to these fractures; thus, the orientation is in the same range as the orientation defined for the fracture set, but the exact values vary.

Overall, two different connections with different levels of permeability are present. A flow path dominated by fractures with a large hydraulic aperture exists between injection interval 4 of both boreholes (Inj1–Int4 and Inj2–Int4). The fractures providing this connection are visible with a high probability in the cross sections  $z = 16$  m and mainly  $z = 17$  m. In general, a good respective permeable connection between two intervals is possible with a large hydraulic aperture of the fractures, with long fractures, with a long intersection length between different fractures, or with a correlation of these factors. In contrast, a connection with fractures with smaller hydraulic apertures appears between injection interval 3 of both boreholes (Inj1–Int3 and Inj2–Int3) and Inj2–Int4. This flow path is present with an average probability of approximately 50% primarily in the cross section  $z = 15$  m. Fractures linking both flow paths appear more likely the closer the location is to injection borehole 2 (i.e., further east). The described behavior is also reflected in the measured data. All responses provoked by the injection in interval 4 of both boreholes are more distinct than for the injection in the intervals 3. Although a maximum hydraulic aperture of  $10^{-3}$  m is enabled by the prior distribution, only a few fractures with a small probability appear with an aperture close to the maximum possible value, as visible in Fig. 4.6, at a depth of  $z = 17$  m. The specific storage coefficient converges to a mean value of  $S = 7.4 \cdot 10^{-7} \text{ Pa}^{-1}$ . Only a few updates were possible that occurred mainly during the burn-in iterations. Therefore, this value is interpreted as the result of an optimization (i.e., as the averaged specific storage to be applied for the whole DFN). The estimated specific storage is greater than the theoretical value that functioned as the minimum value of the prior distribution of the specific storage (Table 4.2). This considers a delay in the response that is not related exclusively to the compressibility of water (Freeze and Cherry, 1979) but also to, for example, the surface roughness or fractures that are only partially open. Multiplied by the maximum possible aperture (Table 4.2), the inferred value is well within the storativity range calculated from cross-borehole injection tests (Klepikova et al., 2020). Several fractures of fracture set 1 appear close to the S3.1 shear zone, indicating either permeable fractures close to the shear zone or a higher permeability of the shear zone in this region than the assigned value. This demonstrates that the prescribed

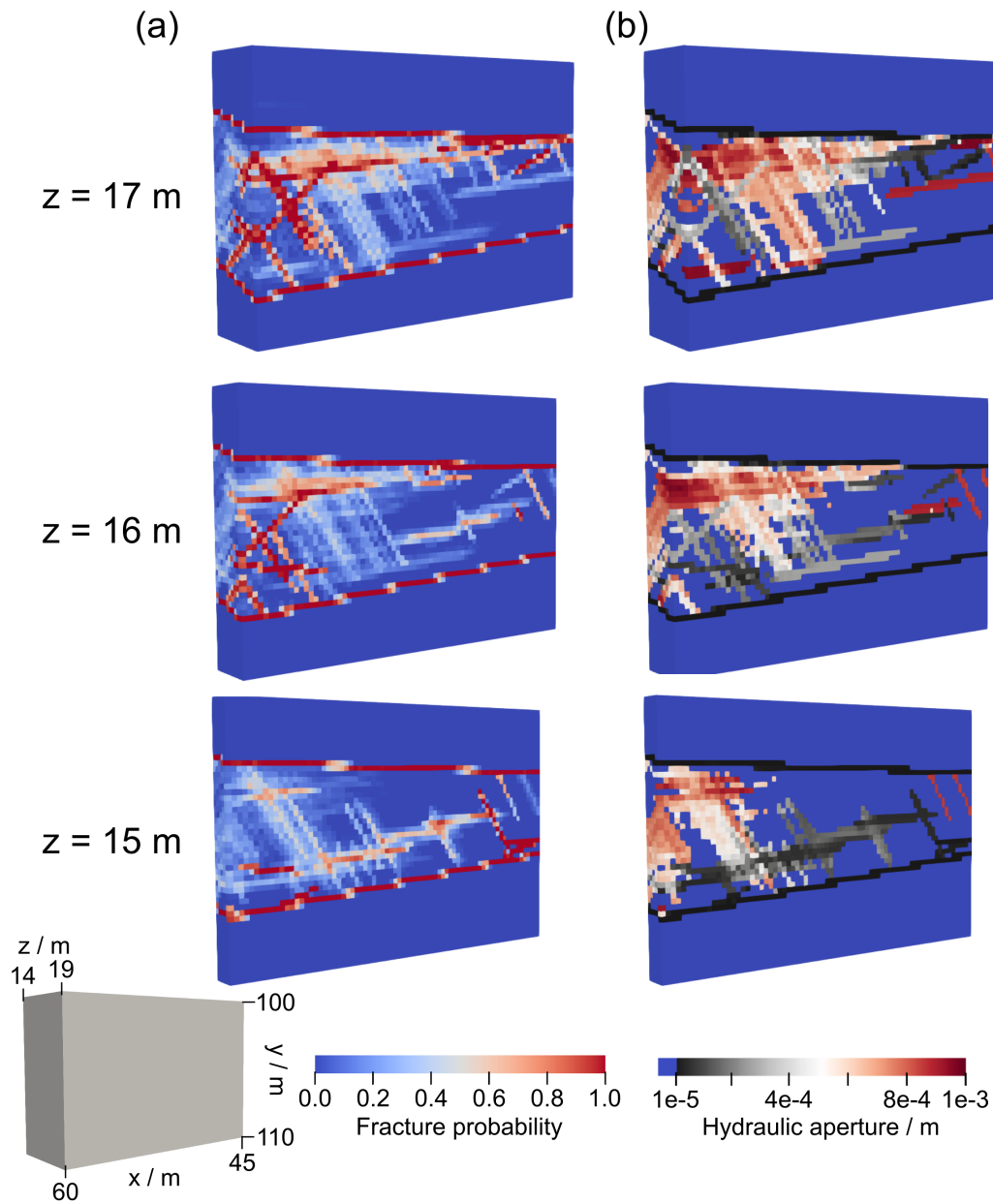


Figure 4.6: Evaluation of the results from the fracture probability map (a) and the mean hydraulic aperture (b) for different cross sections ( $z$ ). The boundaries of the investigated volume are indicated by the cuboid in the lower left.

assumptions with respect to the hydraulic properties of the shear zone do not induce crucial conceptual constraints in the inversion, but a locally high permeability of a shear zone is indicated by a locally high fracture probability.

Although the volume east of injection borehole 2 towards the AU tunnel is part of the inversion (i.e., fractures can be inserted or moved in this volume), the resolution of the results is low because various DFN realizations (i.e., fracture positions) are possible. Only the volume between the two injection boreholes can be evaluated with a sufficient resolution.

### 4.4.4 Comparison with other studies

The inferred flow paths consist of fractures with a high or rather low permeability, which is in accordance with the results of Klepikova et al. (2020). We also compare our results with the structures intersected by other boreholes drilled after conducting the experiments evaluated in this study. While this inversion approach is capable of identifying fractures that are hydraulically relevant, geophysical methods (such as optical televiewer logs) report all structures intercepted by boreholes independent of their permeability. The boreholes PRP1 and FBS1 are partially located within the prior range defined for this study. The 23–25m depth interval for PRP1 has been identified as the interval with the highest transmissivity by Brixel et al. (2020a) and Kittilä et al. (2019). In 95% of the posterior DFN realizations, at least one fracture is present in this interval. Fractures that intersect with the interval between the S3 faults of the FBS1 borehole are present in about 45% of the posterior DFN realizations. This supports the fact that crucial hydraulic features of the DFN can be identified by the presented inversion approach. Still, even if such successful local validation is possible, there are no other independent measurements available to confirm the validity of the inverted complete DFN structure and its probability. Geophysical measurements, such as seismic data (Doetsch et al., 2020) or ground-penetrating radar (Giertzuch et al., 2021b), were able to characterize the ISC volume on a decameter scale and identify the persistent structures and the highly fractured zone; however, they could not delineate or specify the properties of single flow paths.

## 4.5 Conclusions

In this study, we characterized the highly fractured zone at the GTS based on transient pressure signals from hydraulic tomography experiments using a new stochastic inversion method. A stochastic approach was applied to assess the uncertainty of the measured data and the nonuniqueness of the results. The fractured rock is represented directly as a DFN model in the forward simulations. Several posterior DFN realizations that are approximately equally likely are evaluated, and two preferential flow paths dominated by a large or small hydraulic aperture are successfully identified. The presented method relies on some investigations that must be applied prior to the inversion (such as the mapping of structures intercepted by boreholes) and benefits from single- and cross-hole permeability tests for the definition of the hydraulic aperture range. If it is possible to further narrow down the prior range of the hydraulic parameters, the specific storage can be inferred separately for each fracture, instead of computing only a mean value for the whole DFN. In general,

improved results and more insights into the fractured rock can be gained using the same inversion method but with more pressure signals from additional intervals and boreholes.

Future research is necessary on the generally most suitable definition of prior and proposal distributions, which are elementary for robust inversion and for deriving meaningful results. The efficiency of the MCMC sampling can be improved significantly by implementing more elaborate prior or proposal distributions, for example, relying on soft information and site-specific expertise. A further option is utilizing continuous inversion results (such as continuous hydraulic conductivity distributions) or geophysical measurements for highlighting a priori regions with a higher probability of the insertion of fractures or to define zones that are likely connected by fractures to reduce the number of necessary inversion iterations (Dong et al., 2019).

The introduced inversion framework can be applied in a highly flexible way for the characterization of different fractured sites by adapting the site-dependent parameters to meet the conditions of the tomography experiment at each site. Moreover, different types and sources of measured data can be processed for the inversion (such as tracer or in situ stress data), provided that a forward model is available that allows for the flexible update of DFN parameters. The workflow for the setup of the inversion problem is similar. The basis is the properties of the fractures intercepted by the boreholes, i.e., their position and orientation, obtained from optical or acoustic televiewer logs or outcrops. This knowledge is utilized for the prior distributions on the spatial parameters and for the specification of fracture sets. The prior distributions on the hydraulic parameters are based on cross-hole flow tests in this study. This can also be done by the evaluation of the hydraulic tomography experiments as a continuous hydraulic conductivity and specific storage tomogram. As the definition of priors and constraints delineates the range of feasible DFN realizations, this step has to be done carefully. However, the presented Bayesian framework allows the combination of multiple and diverse hard and soft data, which often exist in addition to hydraulic test data that are used to guide the inversion. As demonstrated here, overly tight constraints may be avoided by uniform prior distributions with large value ranges at the expense of a higher computational cost for the inversion. In practice, the amount of information describing the fractured rock is determined mainly by the hydraulic tomography data (i.e., by the number of intervals and boreholes).

The present study paves the way towards the applicability of the discrete inversion approach on a larger scale. The main issue will be to balance the degree of field testing with the desired fracture resolution and the associated computational cost. One possible direction is explicitly implementing only large conductive fractures. The role of smaller fractures with a lower permeability could be represented by calibrating a background permeability within the discrete fracture matrix approach (Berre et al., 2019). Another appealing direction is the representation of scale-dependent fracture sets by their statistical properties following a hierarchical parameterization (Ma et al., 2020).





# 5 Synopsis

## 5.1 Summary and conclusions

Fractured rocks cause a heterogeneous flow field such that the fracture properties cannot be modeled or inferred with a sufficient resolution by a continuous permeability and specific storage distribution. This motivates the application of a discrete representation of the fractures. A novel 3D discrete inversion approach was developed in this study and applied to the reconstruction of a 3D fractured field site for the first time. The chosen discrete approach comprises three elements, which are the explicit representation of fractures as DFN in the forward simulations, the inversion of the structural and hydraulic parameters of the DFN, and the direct evaluation of the DFN parameters. The main hindrance of representing the fractures directly stems from the unknown number of fractures. This was overcome by utilizing the reversible jump MCMC method that also estimates the number of parameters. In this case, the number of fractures was adapted by the inversion algorithm. In addition to the so-called transdimensional update, a parameter update was implemented that adjusts the structural and hydraulic properties of the DFN realizations. This combination is a highly flexible approach for characterizing the parameters of a DFN. Due to the stochastic nature of MCMC methods, uncertainties in the data and the forward modeling are considered.

This thesis demonstrated the field applicability of this new inversion method for a fractured site on a dekameter-scale. The field application of the new inversion approach was prepared by evaluating several synthetic test cases in 2D and 3D. First, the results from hydraulic and tracer tomography applied to a 2D test case were compared. Both approaches were able to identify fractured and non-fractured areas and the main characteristics of the DFN. For this test case, the pressure signals provided a better resolution of the structural properties of the fractures than the tracer breakthrough curves. In addition to the inversion of the DFN structure, the measurement noise and errors in the conceptual model were considered by variance estimation which led to a more realistic setup of the inversion problem for the field application.

In the next step, the inversion method was extended to 3D problems. For that purpose, a fast and robust forward model for the simulation of the transient pressure distribution in a 3D DFN was developed. Inversion results from different 3D synthetic test cases were evaluated to prove the suitability of the method in general. The inverted fracture probability maps accorded well with the setup of the synthetic test cases. The resolution of the fracture probability varied according to the setup of the tomography experiment and the parameter set that is considered

by the inversion algorithm.

Based on the successful work with synthetic test cases, the inversion method was applied to field data, in this case, to the inversion of the structural and hydraulic properties of the highly fractured zone at the Grimsel Test Site (GTS) based on hydraulic tomography. The results revealed two flow paths, whereby one is dominated by fractures with a large hydraulic aperture and the other by fractures with a small hydraulic aperture. The findings coincide with other studies from the In situ Stimulation and Circulation (ISC) experiments and add new information about the highly fractured zone due to the explicit representation of the fractured rock. Overall, a gap was able to be closed by this thesis between continuous state-of-the-art inversion methods and the specific requirements of inferring the properties of fractured rocks.

The first field application of the new inversion method on a dekameter-scale showed promising results and motivates the implementation of the method to the characterization of further fractured sites in rocks with a low-permeability matrix. Thereby, the same inversion concept, i.e., the direct representation of the fractures and the combination of a transdimensional update and a parameter update, can be easily generalized to other sites. The conceptual model, the prior distributions, and the forward model are site-dependent properties, therefore, they have to be customized to match the local conditions. The conceptual model and the prior distributions can be defined based on the known fracture properties. The site-dependent setup of the forward model is essential for a reliable application of the inversion since the pressure signals of the simulated hydraulic tomography experiment are compared with the measured data in the likelihood function of the Bayesian equation. Therefore, the assumptions and simplifications of the forward model have to be rechecked carefully for each site. The location of tunnels or a connection to the surface have to be represented in the boundary conditions as ambient pressure by a Dirichlet boundary condition or inflow/outflow by a Neumann boundary condition. Optional source/sink terms or a Robin boundary condition can simulate the extension of the flow to parts of the rock that are not included in the inversion problem.

Several preliminary studies and a general understanding of the flow characteristics at the site are necessary for a successful implementation of the discrete inversion method. The general properties of the fractures have to be characterized by outcrops or by optical or acoustic televiewer logs for the setup of the conceptual model. The prior distributions of the coordinates of the fractures define the scale of the investigated domain. Therefore, a suitable domain should be specified based on the local geology of the site, such as highly or sparsely fractured regions or shear zones. This information can be obtained, e.g., from seismic data or ground penetrating radar. Single- and cross-hole flow tests provide the prior distribution for the hydraulic parameters. Despite the effort that is necessary for the preparatory work and the required data, the discrete inversion provides useful insights about the properties of the fracture network between boreholes and preferential flow paths, especially in rocks with a low-permeability matrix.

In addition to a more detailed resolution of the fracture properties by the inversion results, another advantage of the explicit representation of the fractured rock

is the further evaluation and processing of the inversion results depending on the planned usage of the investigated site. Several DFN realizations obtained from the inversion algorithm can be utilized for different high-fidelity simulations concerning, e.g., geothermal systems or disposal sites. Simulations of heat extraction or hydrofracturing are a possibility to improve the design and operation of enhanced geothermal systems. Simulations of contaminant transport through a DFN can help to assess the environmental safety of a planned disposal site.

## 5.2 Outlook

Considering the findings from the synthetic test cases and the first field application, various next steps are possible for expanding and transferring the presented discrete inversion method, such as assessing and extending the potential of the approach and reducing the computational costs.

In general, the capabilities, the advantages, and disadvantages of the inversion method have to be examined further which can be achieved by testing the approach over different scales and applications:

- The continuation of the parameter study with synthetic test cases (Ringel et al., 2019, 2021; Somogyvári et al., 2017) allows to investigate the effects of varying DFN parameters, such as the fracture density (Dong et al., 2019), and the influence of deviations from the conceptual fracture model, which are variations of the assumed fracture shape or a variance in the fracture orientations. Their impact can be examined by additional synthetic test cases in 2D and 3D. Quantifying these effects makes the inversion results of field sites more reliable.
- Laboratory experiments with rock blocks or 3D printed fracture networks have the advantage of known fracture locations similar to synthetic tests but also provide more realistic features such as a surface roughness (Brauchler et al., 2013a; Sharmeen et al., 2012; Zhao et al., 2021). Therefore, laboratory experiments bridge the gap between synthetic experiments and field applications.
- On a field scale, the application of the discrete inversion provides more information about the properties of fracture networks compared to continuous inversion approaches. This can be applied to infer and evaluate the features of naturally fractured rocks, the characteristics of an excavation-induced fracture network (Armand et al., 2014; de La Vaissière et al., 2015), and the effects of hydraulic stimulation on fractured rocks (Keilegavlen et al., 2020; Kittilä et al., 2020).
- The inversion results and hydraulic parameters of DFNs over different scales (synthetic, laboratory, and field scale) can be summarized and compared by developing dimensionless numbers, in addition to the Reynolds number.

Specific considerations are necessary for the application of the DFN inversion on a hundred-meter to kilometer scale. The approach has to be implemented carefully to find an optimum between the computational costs of the inversion and the accuracy of the resolution of the fracture properties:

- To reduce the computational costs, the effects of large and small fractures have to be treated differently in the forward simulation. Large fractures with a greater impact on the flow can be implemented directly by their geometric and hydraulic parameters, while smaller fractures are included following their statistical properties which are the fracture density and a fracture length distribution (Ma et al., 2020). The hydraulic effects of the small fractures are considered by assigning a matrix permeability according to the discrete fracture matrix method (Berre et al., 2019).
- The setup of the conceptual model, the simplifications, and assumptions require more consideration concerning their validity over the whole domain. Therefore, more preparatory studies are necessary.
- Precise knowledge is required for the setup of the prior distributions to avoid the computational time for unrealistic DFNs proposed by the inversion algorithm. This is especially the case for the differentiation between large and small fractures which has to be incorporated by the prior distribution of the fracture length.

A major drawback is the computational cost of the method. Due to the stochastic approach, more than 10,000 iterations are required in most cases. This can be improved by reducing either the calculation time of each iteration or the number of necessary iterations:

- The evaluation of the forward model has the main impact on the computation time of each iteration. Therefore, the forward model has to be implemented as a fast and robust simulation code in general. Depending on the application, a multifidelity simulation approach, i.e., the combination of low-fidelity and high-fidelity forward models, can improve the computational efficiency (O'Malley et al., 2018).
- A more specified implementation of prior distributions offers a potential for decreasing the computational efforts by reducing the required number of iterations (Poduri et al., 2021; Zha et al., 2017).
- Hydraulic conductivity tomograms and the variance of the results as obtained from the successive linear estimator approach (Zha et al., 2015; Zhu and Yeh, 2005) can be applied directly as element-wise Gaussian prior distribution in the Bayesian equation and, thereby, in the update probability.
- Results from continuous approaches or geophysical inversion results can be utilized to define regions with a higher or lower probability for inserting a fracture which leads to more efficient proposal functions.

- Geostatistical methods can be applied to facilitate the efficient generation of fracture networks considering realistic geological formations (Blessent et al., 2011; Liu et al., 2009; Park et al., 2004; Shakiba and Doulati Ardejani, 2022; Wang et al., 2017). Thereby, the step of proposing a DFN update can be improved.

So far, the method is limited to data from hydraulic tomography in 3D and rocks with a matrix that can be assumed impermeable:

- Tracer tomography experiments have a few advantages compared to hydraulic tomography since the tracer breakthrough curves can be more easily detected and the noise variance is usually smaller (Ringel et al., 2019; Somogyvári et al., 2017). The inversion problem can be set up in the same way, although the forward simulation is generally more difficult due to possible numerical instabilities because of the convection term in the partial differential equation (Hyman et al., 2015).
- The focus of this study was on fractures within an impermeable rock matrix. Fractured porous media has a non-negligible matrix permeability which has to be estimated by the inversion together with the properties of the fracture network (Berre et al., 2019; Keilegavlen et al., 2020). For that purpose, the most important issues are robust prior distributions for the hydraulic properties of fracture and matrix, such that the correlation between both effects is minimal.
- For the application of heat as tracer, the convective transport of heat in the fractures has to be considered by the forward model. Also, due to the diffusion of heat in the rock matrix, the conduction in the matrix cannot be neglected which makes the inversion problem computationally expensive.

Overall, the discrete inversion method is a valuable tool with various potential applications and different starting points for expanding the approach.



# Appendix

## A.1 Supporting information for Chapter 3

Further inversion results are given as supporting information to Chapter 3. The main characteristics of the discrete fracture network (DFN) can be evaluated in the most flexible way by the reversible jump Markov chain Monte Carlo (rjMCMC) sampling strategy. For comparison, inversion methods that require a fixed number of parameters are also applied here, which may be more suitable when the number of fractures is initially known and thus can be kept constant during the inversion. Moreover, when dealing with a given number of fractures, the effects of each fracture on the flow can be better distinguished and thus the evaluation of the results features additional insights that cannot be revealed easily when applying the rjMCMC. Therefore, they are less likely to be useful in practice and serve mainly as additional information and confirmation of the results presented in the paper.

In this study, the so-called t-walk (traverse or thoughtful walk) MCMC and the delayed rejection adaptive Metropolis algorithm (DRAM) are chosen in addition to the rjMCMC algorithm. The t-walk MCMC (Christen and Fox, 2010) is a black box algorithm that requires almost no tuning. It is designed to be invariant to scale and approximately invariant to affine transformations of the state space, and therefore, it is appropriate to sample from arbitrary continuous distributions. This is achieved by four different randomly chosen proposals. The walk move allows for efficiently mixed samples of distributions with weak correlations, while the traverse move is developed for strong parameter correlations that may change through the state space. The so-called hop and blow moves are necessary to guarantee irreducibility of the chain for arbitrary target distributions, but are chosen with lower probability. The DRAM algorithm (Haario et al., 2006) improves the efficiency of the sampling by combining the delayed rejection Metropolis-Hastings algorithm (Mira, 2001) and the adaption of the proposal covariance matrix based on previous samples (Haario et al., 2001). The delayed rejection algorithm provides samples efficiently to learn the structure of the posterior pdf as the basis for the adaption of the proposal covariance matrix of this structure. Haario et al. (2006) proofed the ergodicity of DRAM and therefore, the proper simulation of the posterior distribution.

Inversion methods for a given number of fractures are applicable, if the number of fractures is known in advance or from the rjMCMC results. In this case, various t-walk chains function as pilot runs to converge to the posterior distribution and to detect local modes in the posterior. Here, again, random starting points are sampled from the prior distribution. This can be used as a starting point for the DRAM algorithm and as a rough estimate of the proposal covariance to be adapted with

the samples. Using the t-walk MCMC to get close to the posterior distribution, is more robust than DRAM, since it requires almost no tuning of the inversion parameters and DRAM is affected more by local minima. MCMC algorithms with a fixed number of fractures provide additional options for the evaluation of the results. Here, the marginal distribution of each parameter can be evaluated by presenting histograms or calculating, for instance, the sample mean and quantiles. The results can be further analyzed by estimating the correlation between parameters, i.e., by 2D scatter plots.

In this base case (Chapter 3), the approximate number of fractures can be evaluated using the FPM as the basis for additionally applying the MCMC inversion algorithms that require the number of parameters to be given. Figure A.1 shows the inversion results by means of calculating the quantiles and checking the range of each fracture parameter. Since the fractures can be distinguished and analyzed individually (Fig. A.1), this provides additional insights about the DFN properties and their correlation. Here, again, it becomes apparent that parameter values of features with a direct influence on the flow path between the injection boreholes are more constrained ( $x$ ,  $z$ , and length of fracture 1 and  $z$  and length of fracture 2 in Fig. A.1a, c, and d). Here, little deviations of the parameters lead to an increased error between the simulated and the observed pressure signals. The quantiles for the evaluation of the  $y$ -coordinate (Fig. A.1b) indicate the difficulty of estimating this parameter as well, due to the lack of information in the direction for this specific test case configuration and, in particular, of the injection points.

Evaluating correlations between parameters provides more insights about the factors with the main influence on the inversion results. The correlation between the length and the  $z$ -coordinate of fracture 4 in Fig. A.2b clarifies that the intersection length with the fracture providing the horizontal connection has the most important effect on the pressure signals. Therefore, moving the position of the center point of the fracture down, requires an increased fracture length for a connection to S/R 2 and the main DFN. This necessitates a correlation between the parameters, which is illustrated in Fig. A.2b. The upper value of the  $z$ -coordinate is limited by injection point 1, since the inversion demonstrated correctly that there is no direct connection between S/R 1 and 2. A similar intersection length can be provided by a few combinations of the fracture parameters  $z_4$  and  $l_4$ . Therefore, more possible combinations of these parameters are accepted as DFN realizations. The significance of the intersection length also explains why so many values are permitted for the  $y$ -coordinate of each fracture.

The outcome and the interpretation regarding the possible properties of each DFN parameter can be accomplished either by inversion approaches with a variable or a fixed number of fractures. The results of both algorithms agree, although, the rjMCMC results are subject to a higher degree of uncertainty, since the setup of the inversion parameters is less constrained. The main advantage of MCMC algorithms with a constant number of parameters are more possibilities for the evaluation of the results, which allows for more insights into the parameters and their correlations.



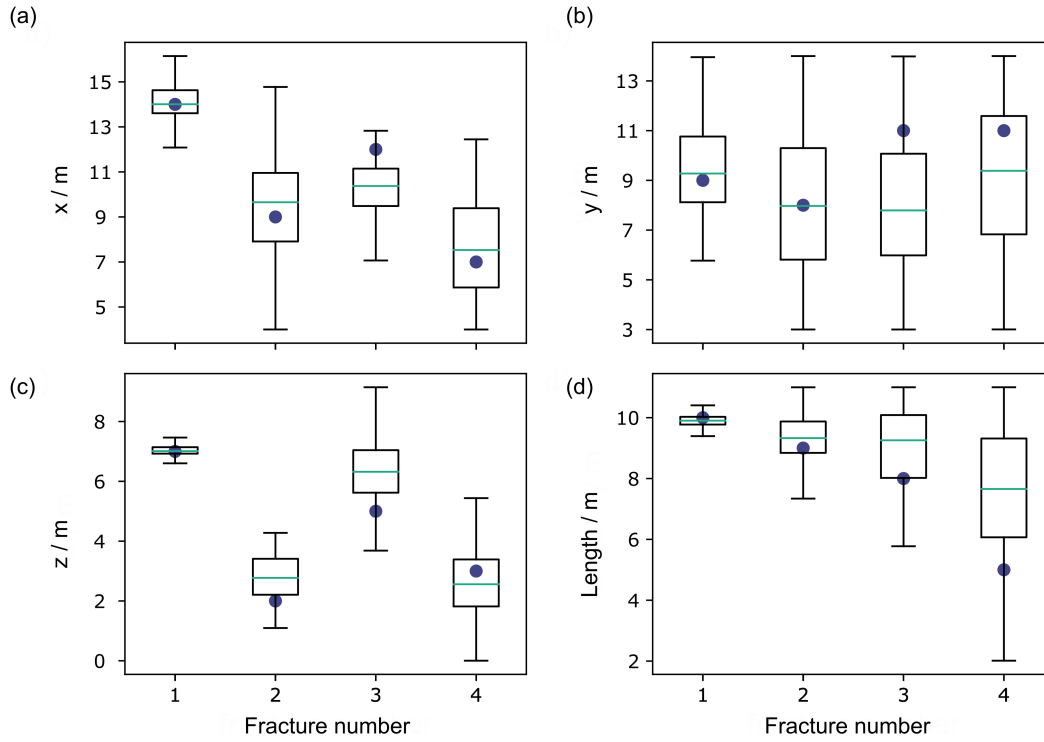


Figure A.1: Range and quantiles of the fracture parameters  $x$  (a),  $y$  (b),  $z$  (c), and fracture length (d) as results from the inversion with a fixed number of fractures for the base test case compared to the value used to set up the test case (blue dot). The fractures denoted as fracture 1 and 2 belong to fracture set 1. Fracture 1 is defined as the fracture with the greater  $z$ -coordinate and fracture 3 is defined as the fracture with the greater  $x$ -coordinate.

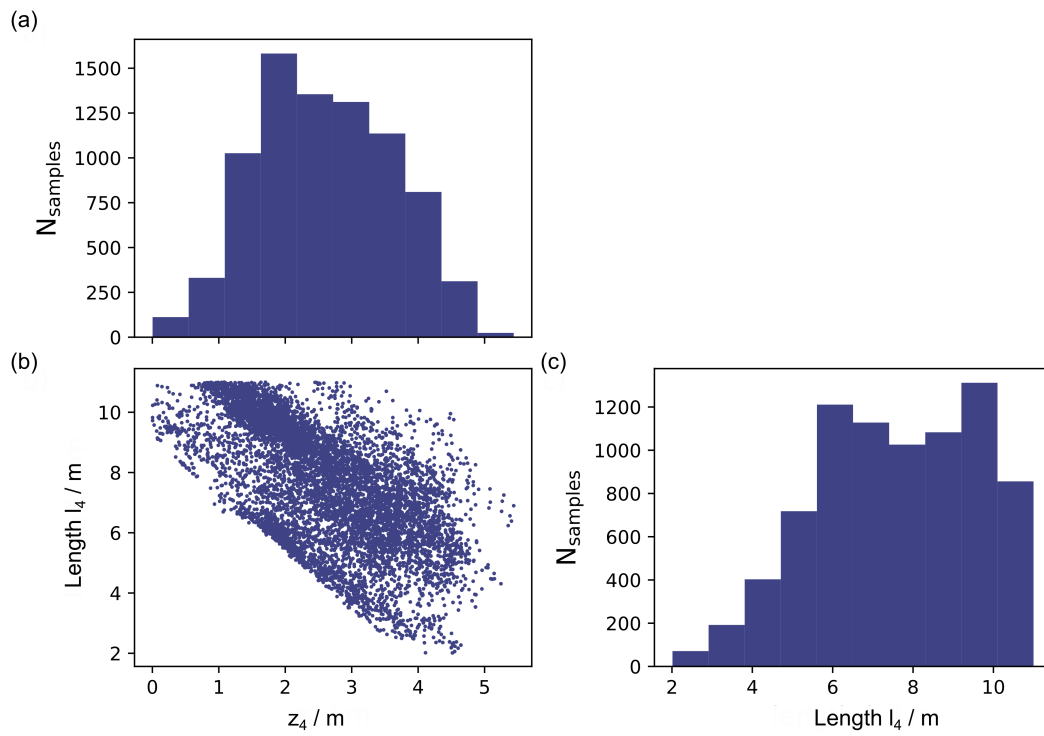


Figure A.2: Histogram of the inversion results of the  $z$ -coordinate (a) and the length (c) of fracture 4 and correlation between both parameters (b).

## References

- Adler, P. M., Thovert, J.-F., and Mourzenko, V. V. (2013). *Fractured porous media*. Oxford Univ. Press, Oxford, <https://doi.org/10.1093/acprof:oso/9780199666515.001.0001>.
- Afshari Moein, M. J., Somogyvári, M., Valley, B., Jalali, M., Loew, S., and Bayer, P. (2018). Fracture network characterization using stress-based tomography. *Journal of Geophysical Research: Solid Earth*, 123(11), 9324–9340. <https://doi.org/10.1029/2018jb016438>.
- Amann, F., Gischig, V., Evans, K., Doetsch, J., Jalali, R., Valley, B., Krietsch, H., Dutler, N., Villiger, L., Brixel, B., Klepikova, M., Kittilä, A., Madonna, C., Wiemer, S., Saar, M. O., Loew, S., Driesner, T., Maurer, H., and Giardini, D. (2018). The seismo-hydromechanical behavior during deep geothermal reservoir stimulations: Open questions tackled in a decameter-scale in situ stimulation experiment. *Solid Earth*, 9(1), 115–137. <https://doi.org/10.5194/se-9-115-2018>.
- Armand, G., Leveau, F., Nussbaum, C., de La Vaissiere, R., Noiret, A., Jaeggi, D., Landrein, P., and Righini, C. (2014). Geometry and properties of the excavation-induced fractures at the Meuse/Haute-Marne URL drifts. *Rock Mechanics and Rock Engineering*, 47(1), 21–41. <https://doi.org/10.1007/s00603-012-0339-6>.
- Aster, R. C., Borchers, B., and Thurber, C. H. (2018). *Parameter estimation and inverse problems*. 3rd edn., Elsevier, Amsterdam and Oxford and Cambridge.
- Barthélémy, J.-F., Guiton, M. L., and Daniel, J.-M. (2009). Estimates of fracture density and uncertainties from well data. *International Journal of Rock Mechanics and Mining Sciences*, 46(3), 590–603. <https://doi.org/10.1016/j.ijrmms.2008.08.003>.
- Berg, S. J. and Illman, W. A. (2011). Three-dimensional transient hydraulic tomography in a highly heterogeneous glaciofluvial aquifer-aquitard system. *Water Resources Research*, 47(10), W10 507. <https://doi.org/10.1029/2011wr010616>.
- Berkowitz, B. (2002). Characterizing flow and transport in fractured geological media: A review. *Advances in Water Resources*, 25(8-12), 861–884. [https://doi.org/10.1016/s0309-1708\(02\)00042-8](https://doi.org/10.1016/s0309-1708(02)00042-8).
- Berre, I., Doster, F., and Keilegavlen, E. (2019). Flow in fractured porous media: A review of conceptual models and discretization approaches. *Transport in Porous Media*, 130(1), 215–236. <https://doi.org/10.1007/s11242-018-1171-6>.

- Blessent, D., Therrien, R., and Lemieux, J.-M. (2011). Inverse modeling of hydraulic tests in fractured crystalline rock based on a transition probability geostatistical approach. *Water Resources Research*, 47(12), W12 530. <https://doi.org/10.1029/2011WR011037>.
- Bodin, T. and Sambridge, M. (2009). Seismic tomography with the reversible jump algorithm. *Geophysical Journal International*, 178(3), 1411–1436. <https://doi.org/10.1111/j.1365-246x.2009.04226.x>.
- Bohling, G. C., Butler, J. J., Zhan, X., and Knoll, M. D. (2007). A field assessment of the value of steady state hydraulic tomography for characterization of aquifer heterogeneities. *Water Resources Research*, 43(5), W05 430. <https://doi.org/10.1029/2006wr004932>.
- Bour, O. and Davy, P. (1997). Connectivity of random fault networks following a power law fault length distribution. *Water Resources Research*, 33(7), 1567–1583. <https://doi.org/10.1029/96WR00433>.
- Brauchler, R., Liedl, R., and Dietrich, P. (2003). A travel time based hydraulic tomographic approach. *Water Resources Research*, 39(12), 1370. <https://doi.org/10.1029/2003wr002262>.
- Brauchler, R., Böhm, G., Leven, C., Dietrich, P., and Sauter, M. (2013a). A laboratory study of tracer tomography. *Hydrogeology Journal*, 21(6), 1265–1274. <https://doi.org/10.1007/s10040-013-1006-z>.
- Brauchler, R., Hu, R., Hu, L., Jiménez, S., Bayer, P., Dietrich, P., and Ptak, T. (2013b). Rapid field application of hydraulic tomography for resolving aquifer heterogeneity in unconsolidated sediments. *Water Resources Research*, 49(4), 2013–2024. <https://doi.org/10.1002/wrcr.20181>.
- Brixel, B., Klepikova, M., Jalali, M., Lei, Q., Roques, C., Kriestch, H., and Loew, S. (2020a). Tracking fluid flow in shallow crustal fault zones: 1. Insights from single-hole permeability estimates. *Journal of Geophysical Research: Solid Earth*, 125(4), e2019JB018 200. <https://doi.org/10.1029/2019JB018200>.
- Brixel, B., Roques, C., Krietsch, H., Klepikova, M., Jalali, M., Lei, Q., and Loew, S. (2020b). Tracking fluid flow in shallow crustal fault zones: 2. Insights from cross-hole forced flow experiments in damage zones. *Journal of Geophysical Research: Solid Earth*, 125(4), e2019JB019 108. <https://doi.org/10.1029/2019JB019108>.
- Brooks, S., Gelman, A., Jones, G., and Meng, X.-L., eds. (2011). *Handbook of Markov Chain Monte Carlo*. Chapman and Hall/CRC, <https://doi.org/10.1201/b10905>.
- Brush, D. J. and Thomson, N. R. (2003). Fluid flow in synthetic rough-walled fractures: Navier-Stokes, Stokes, and local cubic law simulations. *Water Resources Research*, 39(4), 1085. <https://doi.org/10.1029/2002WR001346>.

- Cardiff, M. and Barrash, W. (2011). 3-D transient hydraulic tomography in unconfined aquifers with fast drainage response. *Water Resources Research*, 47(12), W12 518. <https://doi.org/10.1029/2010wr010367>.
- Cardiff, M., Barrash, W., and Kitanidis, P. K. (2012). A field proof-of-concept of aquifer imaging using 3-D transient hydraulic tomography with modular, temporarily-emplaced equipment. *Water Resources Research*, 48(5), W05 531. <https://doi.org/10.1029/2011wr011704>.
- Cardiff, M., Barrash, W., and Kitanidis, P. K. (2013). Hydraulic conductivity imaging from 3-D transient hydraulic tomography at several pumping/observation densities. *Water Resources Research*, 49(11), 7311–7326. <https://doi.org/10.1002/wrcr.20519>.
- Cardiff, M., Zhou, Y., Barrash, W., and Kitanidis, P. K. (2019). Aquifer imaging with oscillatory hydraulic tomography: Application at the field scale. *Groundwater*, 58(5), 710–722. <https://doi.org/10.1111/gwat.12960>.
- Chandra, S., Auken, E., Maurya, P. K., Ahmed, S., and Verma, S. K. (2019). Large scale mapping of fractures and groundwater pathways in crystalline hardrock by AEM. *Scientific Reports*, 9(1), 1–11. <https://doi.org/10.1038/s41598-018-36153-1>.
- Chen, J., Hubbard, S., Peterson, J., Williams, K., Fienen, M., Jardine, P., and Watson, D. (2006). Development of a joint hydrogeophysical inversion approach and application to a contaminated fractured aquifer. *Water Resources Research*, 42(6), W06 425. <https://doi.org/10.1029/2005wr004694>.
- Christen, J. A. and Fox, C. (2010). A general purpose sampling algorithm for continuous distributions (the t-walk). *Bayesian Analysis*, 5(2), 263–281. <https://doi.org/10.1214/10-BA603>.
- Chuang, P.-Y., Chia, Y., Chiu, Y.-C., Teng, M.-H., and Liou, S. Y. H. (2017). Mapping fracture flow paths with a nanoscale zero-valent iron tracer test and a flowmeter test. *Hydrogeology Journal*, 26(1), 321–331. <https://doi.org/10.1007/s10040-017-1651-8>.
- Cliffe, K., Holton, D., Houston, P., Jackson, C. B., Joyce, S., and Milne, A. (2011). Conditioning discrete fracture network models of groundwater flow. *International Journal of Numerical Analysis and Modeling*, 8(4), 543–565.
- Cvetkovic, V. and Cheng, H. (2011). Evaluation of single-well injection-withdrawal tests in Swedish crystalline rock using the Lagrangian travel time approach. *Water Resources Research*, 47(2), W02 527. <https://doi.org/10.1029/2010WR009627>.
- Cvetkovic, V., Cheng, H., Widestrand, H., Byegård, J., Winberg, A., and Andersson, P. (2007). Sorbing tracer experiments in a crystalline rock fracture at Äspö (Swe-

- den): 2. Transport model and effective parameter estimation. *Water Resources Research*, 43(11), W11421. <https://doi.org/10.1029/2006WR005278>.
- Cvetkovic, V., Cheng, H., Byegård, J., Winberg, A., Tullborg, E.-L., and Widestrand, H. (2010). Transport and retention from single to multiple fractures in crystalline rock at Äspö (Sweden): 1. Evaluation of tracer test results and sensitivity analysis. *Water Resources Research*, 46(5), W05505. <https://doi.org/10.1029/2009WR008013>.
- Datta-Gupta, A., Yoon, S., Vasco, D. W., and Pope, G. A. (2002). Inverse modeling of partitioning interwell tracer tests: A streamline approach. *Water Resources Research*, 38(6), 15-1-15-17. <https://doi.org/10.1029/2001wr000597>.
- Day-Lewis, F. D., Lane, J. W., Harris, J. M., and Gorelick, S. M. (2003). Time-lapse imaging of saline-tracer transport in fractured rock using difference-attenuation radar tomography. *Water Resources Research*, 39(10), 1290. <https://doi.org/10.1029/2002wr001722>.
- Day-Lewis, F. D., Slater, L. D., Robinson, J., Johnson, C. D., Terry, N., and Werkema, D. (2017). An overview of geophysical technologies appropriate for characterization and monitoring at fractured-rock sites. *Journal of Environmental Management*, 204, 709-720. <https://doi.org/10.1016/j.jenvman.2017.04.033>.
- de Dreuzy, J.-R., Méheust, Y., and Pichot, G. (2012). Influence of fracture scale heterogeneity on the flow properties of three-dimensional discrete fracture networks (DFN). *Journal of Geophysical Research: Solid Earth*, 117, B11207. <https://doi.org/10.1029/2012JB009461>.
- de La Bernardie, J., Bour, O., Le Borgne, T., Guihéneuf, N., Chatton, E., Labasque, T., Le Lay, H., and Gerard, M.-F. (2018). Thermal attenuation and lag time in fractured rock: Theory and field measurements from joint heat and solute tracer tests. *Water Resources Research*, 54(12), 10,053-10,075. <https://doi.org/10.1029/2018WR023199>.
- de La Vaissière, R., Armand, G., and Talandier, J. (2015). Gas and water flow in an excavation-induced fracture network around an underground drift: A case study for a radioactive waste repository in clay rock. *Journal of Hydrology*, 521, 141-156. <https://doi.org/10.1016/j.jhydrol.2014.11.067>.
- Demirhan, H. and Kalaylioglu, Z. (2015). Joint prior distributions for variance parameters in Bayesian analysis of normal hierarchical models. *Journal of Multivariate Analysis*, 135, 163-174. <https://doi.org/10.1016/j.jmva.2014.12.013>.
- Denison, D. G., Holmes, C. C., Mallick, B. K., and Smith, A. F. (2002). *Bayesian Methods for Nonlinear Classification and Regression*. vol. 386, John Wiley & Sons, Hoboken, NJ, USA.

- Deparis, J., Fricout, B., Jongmans, D., Villemin, T., Effendiantz, L., and Mathy, A. (2008). Combined use of geophysical methods and remote techniques for characterizing the fracture network of a potentially unstable cliff site (the ‘Roche du Midi’, Vercors massif, France). *Journal of Geophysics and Engineering*, 5(2), 147–157. <https://doi.org/10.1088/1742-2132/5/2/002>.
- Doetsch, J., Linde, N., Vogt, T., Binley, A., and Green, A. G. (2012). Imaging and quantifying salt-tracer transport in a riparian groundwater system by means of 3D ERT monitoring. *GEOPHYSICS*, 77(5), B207–B218. <https://doi.org/10.1190/geo2012-0046.1>.
- Doetsch, J., Gischig, V., Krietsch, H., Villiger, L., Amann, F., Dutler, N., Jalali, R., Brixel, B., Klepikova, M., Roques, C., Giertzuch, P.-L., Kittilä, A., and Hochreutener, R. (2018). *Grimsel ISC Experiment Description*. <https://doi.org/10.3929/ETHZ-B-000310581>.
- Doetsch, J., Krietsch, H., Schmelzbach, C., Jalali, M., Gischig, V., Villiger, L., Amann, F., and Maurer, H. (2020). Characterizing a decametre-scale granitic reservoir using ground-penetrating radar and seismic methods. *Solid Earth*, 11(4), 1441–1455. <https://doi.org/10.5194/se-11-1441-2020>.
- Dong, Y., Fu, Y., Yeh, T.-C. J., Wang, Y.-L., Zha, Y., Wang, L., and Hao, Y. (2019). Equivalence of discrete fracture network and porous media models by hydraulic tomography. *Water Resources Research*, 55(4), 3234–3247. <https://doi.org/10.1029/2018wr024290>.
- Dorn, C., Linde, N., Le Borgne, T., Bour, O., and Baron, L. (2011). Single-hole GPR reflection imaging of solute transport in a granitic aquifer. *Geophysical Research Letters*, 38(8), L08401. <https://doi.org/10.1029/2011gl047152>.
- Dorn, C., Linde, N., Doetsch, J., Le Borgne, T., and Bour, O. (2012). Fracture imaging within a granitic rock aquifer using multiple-offset single-hole and cross-hole GPR reflection data. *Journal of Applied Geophysics*, 78, 123–132. <https://doi.org/10.1016/j.jappgeo.2011.01.010>.
- Dorn, C., Linde, N., Le Borgne, T., Bour, O., and de Dreuzy, J.-R. (2013). Conditioning of stochastic 3-D fracture networks to hydrological and geophysical data. *Advances in Water Resources*, 62, 79–89. <https://doi.org/10.1016/j.advwatres.2013.10.005>.
- Fan, Y. and Sisson, S. A. (2011), Reversible jump MCMC, *Handbook of Markov Chain Monte Carlo*, edited by Brooks, S., Gelman, A., Jones, G., and Meng, X.-L., Chapman and Hall/CRC.
- Fang, H. and Zhu, J. (2018). New approach for simulating groundwater flow in discrete fracture network. *Journal of Hydrologic Engineering*, 23(7), 04018025. [https://doi.org/10.1061/\(ASCE\)HE.1943-5584.0001665](https://doi.org/10.1061/(ASCE)HE.1943-5584.0001665).

- Fearnhead, P. (2005). Exact Bayesian curve fitting and signal segmentation. *IEEE Transactions on Signal Processing*, 53(6), 2160–2166. <https://doi.org/10.1109/tsp.2005.847844>.
- Fischer, P., Jardani, A., and Lecoq, N. (2017a). A cellular automata-based deterministic inversion algorithm for the characterization of linear structural heterogeneities. *Water Resources Research*, 53(3), 2016–2034. <https://doi.org/10.1002/2016WR019572>.
- Fischer, P., Jardani, A., Wang, X., Jourde, H., and Lecoq, N. (2017b). Identifying flow networks in a karstified aquifer by application of the cellular automata-based deterministic inversion method (Lez aquifer, France). *Water Resources Research*, 53(12), 10 508–10 522. <https://doi.org/10.1002/2017wr020921>.
- Fischer, P., Jardani, A., Cardiff, M., Lecoq, N., and Jourde, H. (2018a). Hydraulic analysis of harmonic pumping tests in frequency and time domains for identifying the conduits networks in a karstic aquifer. *Journal of Hydrology*, 559, 1039–1053. <https://doi.org/10.1016/j.jhydrol.2018.03.010>.
- Fischer, P., Jardani, A., Jourde, H., Cardiff, M., Wang, X., Chedeville, S., and Lecoq, N. (2018b). Harmonic pumping tomography applied to image the hydraulic properties and interpret the connectivity of a karstic and fractured aquifer (Lez aquifer, France). *Advances in Water Resources*, 119, 227–244. <https://doi.org/10.1016/j.advwatres.2018.07.002>.
- Fischer, P., Jardani, A., and Lecoq, N. (2018c). Hydraulic tomography of discrete networks of conduits and fractures in a karstic aquifer by using a deterministic inversion algorithm. *Advances in Water Resources*, 112, 83–94. <https://doi.org/10.1016/j.advwatres.2017.11.029>.
- Fischer, P., Jardani, A., and Jourde, H. (2020). Hydraulic tomography in coupled discrete-continuum concept to image hydraulic properties of a fractured and karstified aquifer (Lez aquifer, France). *Advances in Water Resources*, 137, 103 523. <https://doi.org/10.1016/j.advwatres.2020.103523>.
- Follin, S., Hartley, L., Rhén, I., Jackson, P., Joyce, S., Roberts, D., and Swift, B. (2014). A methodology to constrain the parameters of a hydrogeological discrete fracture network model for sparsely fractured crystalline rock, exemplified by data from the proposed high-level nuclear waste repository site at Forsmark, Sweden. *Hydrogeology Journal*, 22(2), 313–331. <https://doi.org/10.1007/s10040-013-1080-2>.
- Frampton, A. and Cvetkovic, V. (2010). Inference of field-scale fracture transmissivities in crystalline rock using flow log measurements. *Water Resources Research*, 46(11), W11 502. <https://doi.org/10.1029/2009WR008367>.
- Freeze, R. A. and Cherry, J. A. (1979). *Groundwater*. Prentice Hall, Englewood Cliffs, NJ.



- Gallagher, K., Bodin, T., Sambridge, M., Weiss, D., Kylander, M., and Large, D. (2011). Inference of abrupt changes in noisy geochemical records using transdimensional changepoint models. *Earth and Planetary Science Letters*, 311(1-2), 182–194. <https://doi.org/10.1016/j.epsl.2011.09.015>.
- Gelman, A. (2006). Prior distributions for variance parameters in hierarchical models. *Bayesian Analysis*, 1(3), 515–534. <https://doi.org/10.1214/06-BA117A>.
- Gelman, A., Carlin, J. B., Stern, H. S., Dunson, D. B., Vehtari, A., and Rubin, D. B. (2013). *Bayesian Data Analysis*. Texts in Statistical Science Series, 3rd edn., CRC Press, Boca Raton.
- Geuzaine, C. and Remacle, J.-F. (2009). Gmsh: A 3-D finite element mesh generator with built-in pre- and post-processing facilities. *International Journal for Numerical Methods in Engineering*, 79(11), 1309–1331. <https://doi.org/10.1002/nme.2579>.
- Giertzuch, P.-L., Doetsch, J., Shakas, A., Jalali, M., Brixel, B., and Maurer, H. (2021a). Four-dimensional tracer flow reconstruction in fractured rock through borehole ground-penetrating radar (GPR) monitoring. *Solid Earth*, 12(7), 1497–1513. <https://doi.org/10.5194/se-12-1497-2021>.
- Giertzuch, P.-L., Shakas, A., Doetsch, J., Brixel, B., Jalali, M., and Maurer, H. (2021b). Computing localized breakthrough curves and velocities of saline tracer from ground penetrating radar monitoring experiments in fractured rock. *Energies*, 14(10), 2949. <https://doi.org/10.3390/en14102949>.
- Green, P. J. (1995). Reversible jump Markov chain Monte Carlo computation and Bayesian model determination. *Biometrika*, 82(4), 711–732. <https://doi.org/10.1093/biomet/82.4.711>.
- Haario, H., Saksman, E., and Tamminen, J. (2001). An adaptive Metropolis algorithm. *Bernoulli*, 7(2), 223. <https://doi.org/10.2307/3318737>.
- Haario, H., Laine, M., Mira, A., and Saksman, E. (2006). DRAM: Efficient adaptive MCMC. *Statistics and Computing*, 16(4), 339–354. <https://doi.org/10.1007/s11222-006-9438-0>.
- Hadgu, T., Karra, S., Kalinina, E., Makedonska, N., Hyman, J. D., Klise, K., Viswanathan, H. S., and Wang, Y. (2017). A comparative study of discrete fracture network and equivalent continuum models for simulating flow and transport in the far field of a hypothetical nuclear waste repository in crystalline host rock. *Journal of Hydrology*, 553, 59–70. <https://doi.org/10.1016/j.jhydrol.2017.07.046>.
- Hao, Y., Yeh, T.-C. J., Xiang, J., Illman, W. A., Ando, K., Hsu, K.-C., and Lee, C.-H. (2008). Hydraulic tomography for detecting fracture zone connectivity. *Ground Water*, 46(2), 183–192. <https://doi.org/10.1111/j.1745-6584.2007.00388.x>.

- Hastie, D. I. and Green, P. J. (2012). Model choice using reversible jump Markov chain Monte Carlo. *Statistica Neerlandica*, 66(3), 309–338. <https://doi.org/10.1111/j.1467-9574.2012.00516.x>.
- Hermans, T., Wildemeersch, S., Jamin, P., Orban, P., Brouyère, S., Dassargues, A., and Nguyen, F. (2015). Quantitative temperature monitoring of a heat tracing experiment using cross-borehole ERT. *Geothermics*, 53, 14–26. <https://doi.org/10.1016/j.geothermics.2014.03.013>.
- Hu, L., Bayer, P., Alt-Epping, P., Tatomir, A., Sauter, M., and Brauchler, R. (2015). Time-lapse pressure tomography for characterizing CO<sub>2</sub> plume evolution in a deep saline aquifer. *International Journal of Greenhouse Gas Control*, 39, 91–106. <https://doi.org/10.1016/j.ijggc.2015.04.013>.
- Hu, L., Bayer, P., and Brauchler, R. (2016). Detection of carbon dioxide leakage during injection in deep saline formations by pressure tomography. *Water Resources Research*, 52(7), 5676–5686. <https://doi.org/10.1002/2015wr018420>.
- Hu, R., Brauchler, R., Herold, M., and Bayer, P. (2011). Hydraulic tomography analog outcrop study: Combining travel time and steady shape inversion. *Journal of Hydrology*, 409(1-2), 350–362. <https://doi.org/10.1016/j.jhydrol.2011.08.031>.
- Hyman, J. D., Karra, S., Makedonska, N., Gable, C. W., Painter, S. L., and Viswanathan, H. S. (2015). dfnWorks: A discrete fracture network framework for modeling subsurface flow and transport. *Computers & Geosciences*, 84, 10–19. <https://doi.org/10.1016/j.cageo.2015.08.001>.
- Hyman, J. D., Dentz, M., Hagberg, A., and Kang, P. K. (2019). Linking structural and transport properties in three-dimensional fracture networks. *Journal of Geophysical Research: Solid Earth*, 124(2), 1185–1204. <https://doi.org/10.1029/2018jb016553>.
- Illman, W. A. (2013). Hydraulic tomography offers improved imaging of heterogeneity in fractured rocks. *Groundwater*, 52(5), 659–684. <https://doi.org/10.1111/gwat.12119>.
- Illman, W. A. (2015). Lessons learned from hydraulic and pneumatic tomography in fractured rocks. *Procedia Environmental Sciences*, 25, 127–134. <https://doi.org/10.1016/j.proenv.2015.04.018>.
- Illman, W. A., Craig, A. J., and Liu, X. (2008). Practical issues in imaging hydraulic conductivity through hydraulic tomography. *Groundwater*, 46(1), 120–132. <https://doi.org/10.1111/j.1745-6584.2007.00374.x>.
- Illman, W. A., Liu, X., Takeuchi, S., Jim Yeh, T.-C., Ando, K., and Saegusa, H. (2009). Hydraulic tomography in fractured granite: Mizunami Underground Research site, Japan. *Water Resources Research*, 45(1), W01406. <https://doi.org/10.1029/2007WR006715>.

- Ishibashi, M., Yoshida, H., Sasao, E., and Yuguchi, T. (2016). Long term behavior of hydrogeological structures associated with faulting: An example from the deep crystalline rock in the Mizunami URL, Central Japan. *Engineering Geology*, 208, 114–127. <https://doi.org/10.1016/j.enggeo.2016.04.026>.
- Jalali, M. (2013). Thermo-hydro-mechanical behavior of conductive fractures using a hybrid finite difference—displacement discontinuity method, Ph.D. thesis, University of Waterloo, Waterloo, ON, Canada.
- Jalali, M., Klepikova, M., Doetsch, J., Krietsch, H., Brixel, B., Dutler, N., Gischig, V., and Amann, F. (2018). A multi-scale approach to identify and characterize preferential flow paths in a fractured crystalline rock. *Proceedings of the 52nd U.S. Rock Mechanics/Geomechanics Symposium*, pp. ARMA 18–0496, American Rock Mechanics Association, Alexandria, VA, USA.
- Jardani, A., Revil, A., and Dupont, J. P. (2013). Stochastic joint inversion of hydrogeophysical data for salt tracer test monitoring and hydraulic conductivity imaging. *Advances in Water Resources*, 52, 62–77. <https://doi.org/10.1016/j.advwatres.2012.08.005>.
- Jiang, L., Sun, R., Xiao, W., Liang, X., and Jim Yeh, T.-C. (2022). Spatial correlation analysis between hydraulic conductivity and specific storage in a heterogeneous sandbox by hydraulic tomography. *Journal of Hydrology*, p. 127921. <https://doi.org/10.1016/j.jhydrol.2022.127921>.
- Jiménez, S., Brauchler, R., and Bayer, P. (2013). A new sequential procedure for hydraulic tomographic inversion. *Advances in Water Resources*, 62, 59–70. <https://doi.org/10.1016/j.advwatres.2013.10.002>.
- Jiménez, S., Mariethoz, G., Brauchler, R., and Bayer, P. (2016). Smart pilot points using reversible-jump Markov-chain Monte Carlo. *Water Resources Research*, 52(5), 3966–3983. <https://doi.org/10.1002/2015wr017922>.
- Jougnot, D., Jiménez-Martínez, J., Legendre, R., Le Borgne, T., Méheust, Y., and Linde, N. (2018). Impact of small-scale saline tracer heterogeneity on electrical resistivity monitoring in fully and partially saturated porous media: Insights from geoelectrical milli-fluidic experiments. *Advances in Water Resources*, 113, 295–309. <https://doi.org/10.1016/j.advwatres.2018.01.014>.
- Kang, P. K., Le Borgne, T., Dentz, M., Bour, O., and Juanes, R. (2015). Impact of velocity correlation and distribution on transport in fractured media: Field evidence and theoretical model. *Water Resources Research*, 51(2), 940–959. <https://doi.org/10.1002/2014WR015799>.
- Keilegavlen, E., Berge, R., Fumagalli, A., Staronni, M., Stefansson, I., Varela, J., and Berre, I. (2020). PorePy: An open-source software for simulation of multi-physics processes in fractured porous media. *Computational Geosciences*, 25(1), 243–265. <https://doi.org/10.1007/s10596-020-10002-5>.

- Kittilä, A., Jalali, M., Evans, K. F., Willmann, M., Saar, M. O., and Kong, X.-Z. (2019). Field comparison of DNA-labeled nanoparticle and solute tracer transport in a fractured crystalline rock. *Water Resources Research*, 55(8), 6577–6595. <https://doi.org/10.1029/2019WR025021>.
- Kittilä, A., Jalali, M. R., Somogyvári, M., Evans, K. F., Saar, M. O., and Kong, X.-Z. (2020). Characterization of the effects of hydraulic stimulation with tracer-based temporal moment analysis and tomographic inversion. *Geothermics*, 86, 101–120. <https://doi.org/10.1016/j.geothermics.2020.101820>.
- Klepikova, M., Brixel, B., and Jalali, M. (2020). Transient hydraulic tomography approach to characterize main flowpaths and their connectivity in fractured media. *Advances in Water Resources*, 136, 103–150. <https://doi.org/10.1016/j.advwatres.2019.103500>.
- Klepikova, M. V., Le Borgne, T., Bour, O., Gallagher, K., Hochreutener, R., and Lavenant, N. (2014). Passive temperature tomography experiments to characterize transmissivity and connectivity of preferential flow paths in fractured media. *Journal of Hydrology*, 512, 549–562. <https://doi.org/10.1016/j.jhydrol.2014.03.018>.
- Krietsch, H., Doetsch, J., Dutler, N., Jalali, M., Gischig, V., Loew, S., and Amann, F. (2018). Comprehensive geological dataset describing a crystalline rock mass for hydraulic stimulation experiments. *Scientific Data*, 5(1), 180–269. <https://doi.org/10.1038/sdata.2018.269>.
- Laloy, E., Héroult, R., Jacques, D., and Linde, N. (2018). Training–image based geostatistical inversion using a spatial generative adversarial neural network. *Water Resources Research*, 54(1), 381–406. <https://doi.org/10.1002/2017wr022148>.
- Langtangen, H. P. and Mardal, K.-A. (2019). *Variational Methods for Linear Systems*. Texts in computational science and engineering, Springer International Publishing, [https://doi.org/10.1007/978-3-030-23788-2\\_10](https://doi.org/10.1007/978-3-030-23788-2_10).
- Le Borgne, T., Paillet, F., Bour, O., and Caudal, J.-P. (2006). Cross-borehole flowmeter tests for transient heads in heterogeneous aquifers. *Groundwater*, 44(3), 444–452. <https://doi.org/10.1111/j.1745-6584.2005.00150.x>.
- Le Goc, R., de Dreuzy, J.-R., and Davy, P. (2010). An inverse problem methodology to identify flow channels in fractured media using synthetic steady-state head and geometrical data. *Advances in Water Resources*, 33(7), 782–800. <https://doi.org/10.1016/j.advwatres.2010.04.011>.
- Lee, I.-H., Ni, C.-F., Lin, F.-P., Lin, C.-P., and Ke, C.-C. (2019). Stochastic modeling of flow and conservative transport in three-dimensional discrete fracture networks. *Hydrology and Earth System Sciences*, 23(1), 19–34. <https://doi.org/10.5194/hess-23-19-2019>.

- Li, L., Zhang, Q., Zhou, Z., Cui, Y., Shao, J., and Zhao, Y. (2022). Groundwater circulation patterns in bedrock aquifers from a pre-selected area of high-level radioactive waste repository based on two-dimensional numerical simulation. *Journal of Hydrology*, *610*, 127–149. <https://doi.org/10.1016/j.jhydrol.2022.127849>.
- Liu, Q., Hu, R., Hu, L., Xing, Y., Qiu, P., Yang, H., Fischer, S., and Ptak, T. (2022). Investigation of hydraulic properties in fractured aquifers using cross-well travel-time based thermal tracer tomography: Numerical and field experiments. *Journal of Hydrology*, *609*, 127–151. <https://doi.org/10.1016/j.jhydrol.2022.127751>.
- Liu, X., Zhang, C., Liu, Q., and Birkholzer, J. (2009). Multiple-point statistical prediction on fracture networks at Yucca Mountain. *Environmental Geology*, *57*(6), 1361–1370. <https://doi.org/10.1007/s00254-008-1623-3>.
- Ma, R., Zheng, C., Zachara, J. M., and Tonkin, M. (2012). Utility of bromide and heat tracers for aquifer characterization affected by highly transient flow conditions. *Water Resources Research*, *48*(8), W08523. <https://doi.org/10.1029/2011wr011281>.
- Ma, X., Zhang, K., Yao, C., Zhang, L., Wang, J., Yang, Y., and Yao, J. (2020). Multiscale-network structure inversion of fractured media based on a hierarchical-parameterization and data-driven evolutionary-optimization method. *SPE Journal*, *25*(05), 2729–2748. <https://doi.org/10.2118/201237-pa>.
- Ma, X., Hertrich, M., Amann, F., Bröker, K., Gholizadeh Doonechaly, N., Gischig, V., Hochreutener, R., Kästli, P., Krietsch, H., Marti, M., Nägeli, B., Nejati, M., Obermann, A., Plenkers, K., Rinaldi, A. P., Shakas, A., Villiger, L., Wenning, Q., Zappone, A., Bethmann, F., Castilla, R., Seberio, F., Meier, P., Driesner, T., Loew, S., Maurer, H., Saar, M. O., Wiemer, S., and Giardini, D. (2022). Multi-disciplinary characterizations of the BedrettoLab – a new underground geoscience research facility. *Solid Earth*, *13*(2), 301–322. <https://doi.org/10.5194/se-13-301-2022>.
- Mardia, K. V., Nyirongo, V. B., Walder, A. N., Xu, C., Dowd, P. A., Fowell, R. J., and Kent, J. T. (2007). Markov chain Monte Carlo implementation of rock fracture modelling. *Mathematical Geology*, *39*(4), 355–381. <https://doi.org/10.1007/s11004-007-9099-3>.
- Massiot, C., Townend, J., Nicol, A., and McNamara, D. D. (2017). Statistical methods of fracture characterization using acoustic borehole televiewer log interpretation. *Journal of Geophysical Research: Solid Earth*, *122*(8), 6836–6852. <https://doi.org/10.1002/2017JB014115>.
- Metropolis, N., Rosenbluth, A. W., Rosenbluth, M. N., Teller, A. H., and Teller, E. (1953). Equation of state calculations by fast computing machines. *The Journal of Chemical Physics*, *21*(6), 1087–1092. <https://doi.org/10.1063/1.1699114>.

- Mira, A. (2001). On Metropolis–Hastings algorithms with delayed rejection. *Metron – International Journal of Statistics*, 3, 231.
- Neuman, S. P. (2005). Trends, prospects and challenges in quantifying flow and transport through fractured rocks. *Hydrogeology Journal*, 13(1), 124–147. <https://doi.org/10.1007/s10040-004-0397-2>.
- Ni, C.-F. and Yeh, T.-C. J. (2008). Stochastic inversion of pneumatic cross-hole tests and barometric pressure fluctuations in heterogeneous unsaturated formations. *Advances in Water Resources*, 31(12), 1708–1718. <https://doi.org/10.1016/j.advwatres.2008.08.007>.
- O'Malley, D., Karra, S., Hyman, J. D., Viswanathan, H. S., and Srinivasan, G. (2018). Efficient Monte Carlo with graph-based subsurface flow and transport models. *Water Resources Research*, 54(5), 3758–3766. <https://doi.org/10.1029/2017wr022073>.
- Oron, A. P. and Berkowitz, B. (1998). Flow in rock fractures: The local cubic law assumption reexamined. *Water Resources Research*, 34(11), 2811–2825. <https://doi.org/10.1029/98WR02285>.
- Paradis, D., Gloaguen, E., Lefebvre, R., and Giroux, B. (2016). A field proof-of-concept of tomographic slug tests in an anisotropic littoral aquifer. *Journal of Hydrology*, 536, 61–73. <https://doi.org/10.1016/j.jhydrol.2016.02.041>.
- Park, Y.-J., Sudicky, E. A., McLaren, R. G., and Sykes, J. F. (2004). Analysis of hydraulic and tracer response tests within moderately fractured rock based on a transition probability geostatistical approach. *Water Resources Research*, 40(12), W12404. <https://doi.org/10.1029/2004WR003188>.
- Pavičić, I., Galić, I., Kucelj, M., and Dragičević, I. (2021). Fracture system and rock-mass characterization by borehole camera surveying: Application in dimension stone investigations in geologically complex structures. *Applied Sciences*, 11(2), 764. <https://doi.org/10.3390/app11020764>.
- Poduri, S., Kambhammettu, B., and Gorugantula, S. (2021). A new randomized binary prior model for hydraulic tomography in fractured aquifers. *Groundwater*, 59(4), 537–548. <https://doi.org/https://doi.org/10.1111/gwat.13074>.
- Punskaya, E., Andrieu, C., Doucet, A., and Fitzgerald, W. J. (2002). Bayesian curve fitting using MCMC with applications to signal segmentation. *IEEE Transactions on Signal Processing*, 50(3), 747–758. <https://doi.org/10.1109/78.984776>.
- Reddy, J. N. and Gartling, D. K. (2010). *The Finite Element Method in Heat Transfer and Fluid Dynamics*. 3 edn., Taylor & Francis.
- Ren, S., Gragg, S., Zhang, Y., Carr, B. J., and Yao, G. (2018). Borehole characterization of hydraulic properties and groundwater flow in a crystalline fractured

- aquifer of a headwater mountain watershed, Laramie Range, Wyoming. *Journal of Hydrology*, 561, 780–795. <https://doi.org/10.1016/j.jhydrol.2018.04.048>.
- Ren, S., Zhang, Y., Jim Yeh, T.-C., Wang, Y., and Carr, B. J. (2021). Multi-scale hydraulic conductivity characterization in a fractured granitic aquifer: The evaluation of scale effect. *Water Resources Research*, 57(9), e2020WR028482. <https://doi.org/10.1029/2020WR028482>.
- Ringel, L. M., Somogyvári, M., Jalali, M., and Bayer, P. (2019). Comparison of hydraulic and tracer tomography for discrete fracture network inversion. *Geosciences*, 9(6), 274. <https://doi.org/10.3390/geosciences9060274>.
- Ringel, L. M., Jalali, M., and Bayer, P. (2021). Stochastic inversion of three-dimensional discrete fracture network structure with hydraulic tomography. *Water Resources Research*, 57(12), e2021WR030401. <https://doi.org/10.1029/2021WR030401>.
- Ringel, L. M., Jalali, M., and Bayer, P. (2022). Characterization of the highly fractured zone at the Grimsel Test Site based on hydraulic tomography. *Hydrology and Earth System Sciences*, 26(24), 6443–6455. <https://doi.org/10.5194/hess-26-6443-2022>.
- Robinson, J., Slater, L., Johnson, T., Shapiro, A., Tiedeman, C., Ntarlagiannis, D., Johnson, C., Day-Lewis, F., Lacombe, P., Imbrigiotta, T., and Lane, J. (2016). Imaging pathways in fractured rock using three-dimensional electrical resistivity tomography. *Groundwater*, 54(2), 186–201. <https://doi.org/10.1111/gwat.12356>.
- Roubinet, D., de Dreuzy, J.-R., and Davy, P. (2010). Connectivity-consistent mapping method for 2-D discrete fracture networks. *Water Resources Research*, 46(7), W07532. <https://doi.org/10.1029/2009wr008302>.
- Sambridge, M. (2016). Reconstructing time series and their uncertainty from observations with universal noise. *Journal of Geophysical Research: Solid Earth*, 121(7), 4990–5012. <https://doi.org/10.1002/2016jb012901>.
- Sambridge, M., Gallagher, K., Jackson, A., and Rickwood, P. (2006). Trans-dimensional inverse problems, model comparison and the evidence. *Geophysical Journal International*, 167(2), 528–542. <https://doi.org/10.1111/j.1365-246X.2006.03155.x>.
- Sánchez-León, E., Erdal, D., Leven, C., and Cirpka, O. A. (2020a). Comparison of two ensemble Kalman-based methods for estimating aquifer parameters from virtual 2-D hydraulic and tracer tomographic tests. *Geosciences*, 10(7), 276. <https://doi.org/10.3390/geosciences10070276>.
- Sánchez-León, E., Leven, C., Erdal, D., and Cirpka, O. A. (2020b). Comparison of two ensemble-Kalman filter based methods for estimating aquifer parameters

- from real 3-D hydraulic and tracer tomographic tests. *Geosciences*, 10(11), 462. <https://doi.org/10.3390/geosciences10110462>.
- Schwede, R. L., Li, W., Leven, C., and Cirpka, O. A. (2014). Three-dimensional geostatistical inversion of synthetic tomographic pumping and heat-tracer tests in a nested-cell setup. *Advances in Water Resources*, 63, 77–90. <https://doi.org/10.1016/j.advwatres.2013.11.004>.
- Shakiba, S. and Doulati Ardejani, F. (2022). A comparative study of novel object-based geostatistical algorithm and direct sampling method on fracture network modeling. *Stochastic Environmental Research and Risk Assessment*, pp. 1–17. <https://doi.org/10.1007/s00477-022-02320-0>.
- Sharmeen, R., Illman, W. A., Berg, S. J., Yeh, T.-C. J., Park, Y.-J., Sudicky, E. A., and Ando, K. (2012). Transient hydraulic tomography in a fractured dolostone: Laboratory rock block experiments. *Water Resources Research*, 48(10), W10 532. <https://doi.org/10.1029/2012WR012216>.
- Singha, K. and Gorelick, S. M. (2005). Saline tracer visualized with three-dimensional electrical resistivity tomography: Field-scale spatial moment analysis. *Water Resources Research*, 41(5), W05 023. <https://doi.org/10.1029/2004wr003460>.
- Somogyvári, M. and Bayer, P. (2017). Field validation of thermal tracer tomography for reconstruction of aquifer heterogeneity. *Water Resources Research*, 53(6), 5070–5084. <https://doi.org/10.1002/2017wr020543>.
- Somogyvári, M., Bayer, P., and Brauchler, R. (2016). Travel-time-based thermal tracer tomography. *Hydrology and Earth System Sciences*, 20(5), 1885–1901. <https://doi.org/10.5194/hess-20-1885-2016>.
- Somogyvári, M., Jalali, M., Parras, S. J., and Bayer, P. (2017). Synthetic fracture network characterization with transdimensional inversion. *Water Resources Research*, 53(6), 5104–5123. <https://doi.org/10.1002/2016WR020293>.
- Somogyvári, M., Kühn, M., and Reich, S. (2019). Reservoir-scale transdimensional fracture network inversion. *Advances in Geosciences*, 49, 207–214. <https://doi.org/10.5194/adgeo-49-207-2019>.
- Spencer, S. A., Anderson, A. E., Silins, U., and Collins, A. L. (2021). Hillslope and groundwater contributions to streamflow in a Rocky Mountain watershed underlain by glacial till and fractured sedimentary bedrock. *Hydrology and Earth System Sciences*, 25(1), 237–255. <https://doi.org/10.5194/hess-25-237-2021>.
- Tan, L., Xiang, W., Luo, J., Liu, Q., and Zuo, X. (2020). Investigation of the models of flow through fractured rock masses based on borehole data. *Advances in Civil Engineering*, 2020, 4219 847. <https://doi.org/10.1155/2020/4219847>.



- Tiedeman, C. R. and Barrash, W. (2020). Hydraulic tomography: 3D hydraulic conductivity, fracture network, and connectivity in mudstone. *Groundwater*, 58(2), 238–257. <https://doi.org/10.1111/gwat.12915>.
- Tiedeman, C. R., Lacombe, P. J., and Goode, D. J. (2010). Multiple well-shutdown tests and site-scale flow simulation in fractured rocks. *Groundwater*, 48(3), 401–415. <https://doi.org/10.1111/j.1745-6584.2009.00651.x>.
- Tran, N. H. and Tran, K. (2007). Combination of fuzzy ranking and simulated annealing to improve discrete fracture inversion. *Mathematical and Computer Modelling*, 45(7-8), 1010–1020. <https://doi.org/10.1016/j.mcm.2006.08.013>.
- Tso, C.-H. M., Zha, Y., Yeh, T.-C. J., and Wen, J.-C. (2016). The relative importance of head, flux, and prior information in hydraulic tomography analysis. *Water Resources Research*, 52(1), 3–20. <https://doi.org/10.1002/2015wr017191>.
- Vasco, D. W. and Datta-Gupta, A. (1999). Asymptotic solutions for solute transport: A formalism for tracer tomography. *Water Resources Research*, 35(1), 1–16. <https://doi.org/10.1029/98WR02742>.
- Vesselinov, V. V., Neuman, S. P., and Illman, W. A. (2001). Three-dimensional numerical inversion of pneumatic cross-hole tests in unsaturated fractured tuff: 1. Methodology and borehole effects. *Water Resources Research*, 37(12), 3001–3017. <https://doi.org/10.1029/2000wr000133>.
- Vogler, D., Walsh, S. D. C., Bayer, P., and Amann, F. (2017). Comparison of surface properties in natural and artificially generated fractures in a crystalline rock. *Rock Mechanics and Rock Engineering*, 50(11), 2891–2909. <https://doi.org/10.1007/s00603-017-1281-4>.
- Voorn, M., Exner, U., Barnhoorn, A., Baud, P., and Reuschlé, T. (2015). Porosity, permeability and 3D fracture network characterisation of dolomite reservoir rock samples. *Journal of Petroleum Science and Engineering*, 127, 270–285. <https://doi.org/10.1016/j.petrol.2014.12.019>.
- Vu, M. T. and Jardani, A. (2022). Mapping discrete fracture networks using inversion of hydraulic tomography data with convolutional neural network: SegNet-fracture. *Journal of Hydrology*, 609, 127752. <https://doi.org/10.1016/j.jhydrol.2022.127752>.
- Wang, X., Jardani, A., Jourde, H., Lonergan, L., Cosgrove, J., Gosselin, O., and Massonnat, G. (2016). Characterisation of the transmissivity field of a fractured and karstic aquifer, Southern France. *Advances in Water Resources*, 87, 106–121. <https://doi.org/10.1016/j.advwatres.2015.10.014>.
- Wang, X., Jardani, A., and Jourde, H. (2017). A hybrid inverse method for hydraulic tomography in fractured and karstic media. *Journal of Hydrology*, 551, 29–46. <https://doi.org/10.1016/j.jhydrol.2017.05.051>.

- Watanabe, N., Blöcher, G., Cacace, M., Held, S., and Kohl, T. (2017). *Geoenergy Modeling III: Enhanced Geothermal Systems*. SpringerBriefs in Energy, Springer, Cham, <https://doi.org/10.1007/978-3-319-46581-4>.
- Wen, J.-C., Chen, J.-L., Yeh, T.-C. J., Wang, Y.-L., Huang, S.-Y., Tian, Z., and Yu, C.-Y. (2019). Redundant and nonredundant information for model calibration or hydraulic tomography. *Groundwater*, *58*(1), 79–92. <https://doi.org/10.1111/gwat.12879>.
- Wenning, Q. C., Madonna, C., de Haller, A., and Burg, J.-P. (2018). Permeability and seismic velocity anisotropy across a ductile–brittle fault zone in crystalline rock. *Solid Earth*, *9*(3), 683–698. <https://doi.org/10.5194/se-9-683-2018>.
- Wilske, C., Suckow, A., Mallast, U., Meier, C., Merchel, S., Merkel, B., Pavetich, S., Rödiger, T., Rugel, G., Sachse, A., Weise, S. M., and Siebert, C. (2020). A multi-environmental tracer study to determine groundwater residence times and recharge in a structurally complex multi-aquifer system. *Hydrology and Earth System Sciences*, *24*(1), 249–267. <https://doi.org/10.5194/hess-24-249-2020>.
- Wu, H., Fu, P., Zhang, J., and Morris, J. P. (2020). Interpretation of tracer data using a Markov chain Monte Carlo approach for the characterization of the EGS Collab testbed. *Proceedings of the 54th U.S. Rock Mechanics/Geomechanics Symposium*, pp. ARMA 20–1705, American Rock Mechanics Association.
- Wu, H., Zhang, J., Fu, P., and Morris, J. P. (2021). Inferring fracture aperture distribution at the EGS Collab Experiment 1 testbed through a deep learning accelerated Bayesian approach. *Proceedings of the 46th Workshop on Geothermal Reservoir Engineering*.
- Yang, H., Hu, R., Qiu, P., Liu, Q., Xing, Y., Tao, R., and Ptak, T. (2020). Application of wavelet de-noising for travel-time based hydraulic tomography. *Water*, *12*(6), 1533. <https://doi.org/10.3390/w12061533>.
- Yeh, T.-C. J. and Liu, S. (2000). Hydraulic tomography: Development of a new aquifer test method. *Water Resources Research*, *36*(8), 2095–2105. <https://doi.org/10.1029/2000wr900114>.
- Yin, T. and Chen, Q. (2020). Simulation-based investigation on the accuracy of discrete fracture network (DFN) representation. *Computers and Geotechnics*, *121*, 103487. <https://doi.org/10.1016/j.compgeo.2020.103487>.
- Zha, Y., Yeh, T.-C. J., Illman, W. A., Tanaka, T., Bruines, P., Onoe, H., and Saegusa, H. (2015). What does hydraulic tomography tell us about fractured geological media? A field study and synthetic experiments. *Journal of Hydrology*, *531*, 17–30. <https://doi.org/10.1016/j.jhydrol.2015.06.013>.

- Zha, Y., Yeh, T.-C. J., Illman, W. A., Tanaka, T., Bruines, P., Onoe, H., Saegusa, H., Mao, D., Takeuchi, S., and Wen, J.-C. (2016). An application of hydraulic tomography to a large-scale fractured granite site, Mizunami, Japan. *Ground Water*, 54(6), 793–804. <https://doi.org/10.1111/gwat.12421>.
- Zha, Y., Yeh, T.-C. J., Illman, W. A., Onoe, H., Mok, C. M. W., Wen, J.-C., Huang, S.-Y., and Wang, W. (2017). Incorporating geologic information into hydraulic tomography: A general framework based on geostatistical approach. *Water Resources Research*, 53(4), 2850–2876. <https://doi.org/10.1002/2016WR019185>.
- Zha, Y., Yeh, T.-C. J., Illman, W. A., Zeng, W., Zhang, Y., Sun, F., and Shi, L. (2018). A reduced-order successive linear estimator for geostatistical inversion and its application in hydraulic tomography. *Water Resources Research*, 54(3), 1616–1632. <https://doi.org/10.1002/2017wr021884>.
- Zhao, H., Luo, N., and Illman, W. A. (2021). The importance of fracture geometry and matrix data on transient hydraulic tomography in fractured rocks: Analyses of synthetic and laboratory rock block experiments. *Journal of Hydrology*, 601, 126700. <https://doi.org/10.1016/j.jhydrol.2021.126700>.
- Zhao, Z. and Illman, W. A. (2017). On the importance of geological data for three-dimensional steady-state hydraulic tomography analysis at a highly heterogeneous aquifer-aquitard system. *Journal of Hydrology*, 544, 640–657. <https://doi.org/10.1016/j.jhydrol.2016.12.004>.
- Zhao, Z., Illman, W. A., Yeh, T.-C. J., Berg, S. J., and Mao, D. (2015). Validation of hydraulic tomography in an unconfined aquifer: A controlled sand-box study. *Water Resources Research*, 51(6), 4137–4155. <https://doi.org/10.1002/2015wr016910>.
- Zhao, Z., Illman, W. A., Zha, Y., Yeh, T.-C. J., Mok, C. M. B., Berg, S. J., and Han, D. (2019). Transient hydraulic tomography analysis of fourteen pumping tests at a highly heterogeneous multiple aquifer-aquitard system. *Water*, 11(9), 1864. <https://doi.org/10.3390/w11091864>.
- Zhu, J. and Yeh, T.-C. J. (2005). Characterization of aquifer heterogeneity using transient hydraulic tomography. *Water Resources Research*, 41(7), W07028. <https://doi.org/10.1029/2004WR003790>.
- Ziegler, M., Loew, S., and Moore, J. R. (2013). Distribution and inferred age of exfoliation joints in the Aar Granite of the central Swiss Alps and relationship to Quaternary landscape evolution. *Geomorphology*, 201, 344–362. <https://doi.org/10.1016/j.geomorph.2013.07.010>.
- Zienkiewicz, O. C., Nithiarasu, P., and Taylor, R. L. (2014). *The finite element method for fluid dynamics*. 7th edn., Butterworth-Heinemann, Oxford.

## References

---

Zimmerman, R. W. and Bodvarsson, G. S. (1996). Hydraulic conductivity of rock fractures. *Transport in Porous Media*, 23(1), 1–30. <https://doi.org/10.1007/BF00145263>.

# Curriculum vitae

## Personal information

- Name: Lisa Maria Ringel
- Date of birth: 10 April, 1995
- Place of birth: Ingolstadt

## Professional experience

- 11/2019 – Current: **Research assistant**, Applied Geology, Institute of Geosciences and Geography, MLU Halle-Wittenberg, Halle (Saale), Germany
- 10/2018 – 10/2019: **Research assistant**, Institute of new Energy System, University of Applied Sciences Ingolstadt, Ingolstadt, Germany

## Education

- 11/2019 – Current: **PhD student**, Applied Geology, Institute of Geosciences and Geography, MLU Halle-Wittenberg, Halle (Saale), Germany  
Title: Stochastic characterization of discrete fractures in rocks by hydraulic tomography
- 03/2018 – 10/2018: **Master's thesis**, Institute of Aeroelasticity, German Aerospace Center, Göttingen, Germany  
Title: Preliminary design of a wind tunnel experiment for transient shock boundary layer interaction
- 03/2017 – 10/2018: **M.Eng. Technical Development in Mechanical Engineering**, University of Applied Sciences Ingolstadt, Ingolstadt, Germany
- 10/2013 – 03/2017: **B.Eng. Renewable Energy Technologies**, University of Applied Sciences Ingolstadt, Ingolstadt, Germany

## List of publications

### Peer-reviewed publications

**Ringel, L. M.**, Jalali, M., & Bayer, P. (2022). Characterization of the highly fractured zone at the Grimsel Test Site based on hydraulic tomography. *Hydrology and Earth System Sciences*. 26(24), 6443–6455. <https://doi.org/10.5194/hess-26-6443-2022>

**Ringel, L. M.**, Jalali, M., & Bayer, P. (2021). Stochastic Inversion of Three-Dimensional Discrete Fracture Network Structure With Hydraulic Tomography. *Water Resources Research*. 57(12), e2021WR030401. <https://doi.org/10.1029/2021WR030401>.

**Ringel, L. M.**, Somogyvári, M., Jalali, M., & Bayer, P. (2019). Comparison of Hydraulic and Tracer Tomography for Discrete Fracture Network Inversion. *Geosciences*, 9(6), 274. <https://doi.org/10.3390/geosciences9060274>.

### Conference contributions

**Ringel, L. M.**, Jalali M., & Bayer, P. (2022). Estimation of hydraulic and geometrical characteristics of fractured geothermal reservoirs using in-situ tomographic methods, *European Geothermal Congress 2022*, Berlin, Germany, 17–21 October 2022.

**Ringel, L. M.**, Jalali, M., & Bayer, P. (2022). Inversion of Hydraulic Tomography Data from the Grimsel Test Site with a Discrete Fracture Network Model, *EGU General Assembly 2022*, Vienna, Austria, 23–27 May 2022.

**Ringel, L. M.**, Somogyvari, M., Jalali, M. & Bayer, P.(2020). Characterization of discrete fracture networks by invasive tomographic methods, *Computational Methods in Water Resources*, virtual, 14–17 December 2020.

**Ringel, L. M.**, Jalali, M. & Bayer, P. (2020). Inversion of three-dimensional discrete fracture networks using hydraulic tomography, *AGU Fall Meeting 2020*, virtual, 1–17 December 2020.

Nitzsche, J., **Ringel, L. M.**, Kaiser, C., Hennings, H. (2019). Fluid-mode flutter in plane transonic flows, *International Forum on Aeroleasticity and Structural Dynamics*, Savannah, USA, 10–13 June, 2019.

**Ringel, L. M.**, Somogyvári, M., Jalali, M., & Bayer, P. (2019). Inversion of discrete fracture networks by hydraulic and tracer tomography, *EGU General Assembly 2019*, Vienna, Austria, 7–12 April 2019.

# Declaration

Ich erkläre an Eides statt, dass ich die Arbeit selbstständig und ohne fremde Hilfe verfasst, keine anderen als die von mir angegebenen Quellen und Hilfsmittel benutzt und die den benutzten Werken wörtlich oder inhaltlich entnommenen Stellen als solche kenntlich gemacht habe.

I declare under penalty of perjury that this thesis is my own work entirely and has been written without any help from other people. I used only the sources mentioned and included all the citations correctly both in word and content.

---

(Datum, Date)

---

(Unterschrift, Signature)